UC San Diego

UC San Diego Electronic Theses and Dissertations

Title

A study on enhanced electrochemical stability in water electrolysis components, via stoichiometry tuned atomic layer deposited films

Permalink

https://escholarship.org/uc/item/77j28187

ISBN

9798293833634

Author

Wang, Kesong

Publication Date

2025-09-13

Peer reviewed|Thesis/dissertation

eScholarship.org Powered by the California Digital Library
University of California

UNIVERSITY OF CALIFORNIA SAN DIEGO

A study on enhanced electrochemical stability in water electrolysis components, via stoichiometry tuned atomic layer deposited films

A Dissertation submitted in partial satisfaction of the requirements
for the degree Doctor of Philosophy

in

Engineering Sciences (Mechanical Engineering)

by

Kesong Wang

Committee in charge:

Professor Prabhakar R. Bandaru, Chair
Professor Andrew C. Kummel, Co-Chair
Professor Yu Qiao
Professor David Saintillan

2025

Copyright

Kesong Wang, 2025

All rights reserved.

The Dissertation of Kesong Wang is approved, and it is acceptable in quality and form for publication on microfilm and electronically.

University of California San Diego

2025

DEDICATION

To my family, whose unwavering support, love, and encouragement have guided me through every stage of life and made this journey possible.

To my friends and collaborators, whose companionship and support helped me navigate the challenges along the way.

To my academic advisors, Prof. Prabhakar R. Bandaru and Prof. Andrew C. Kummel, for their invaluable guidance, mentorship, and support throughout my Ph.D. research and beyond.

TABLE OF CONTENTS

DISSERTATION APPROVAL PAGE iii

DEDICATION iv

TABLE OF CONTENTS v

LIST OF FIGURES viii

LIST OF TABLES xi

ACKNOWLEDGEMENTS xii

VITA xv

ABSTRACT OF THE DISSERTATION xvi

Chapter 1 Introduction 1

1.1 Hydrogen Energy and the Role of Water Electrolyzers 1

1.2 Challenges in PEM Water Electrolyzer Materials 2

1.3 Atomic Layer Deposition (ALD) for Corrosion Protection 3

1.4 Electrochemical Characterization: Potentiostatic and Potentiodynamic Techniques 4

1.5 Inductive Coupled Plasma Mass Spectrometry (ICP-MS) 6

1.6 Electrochemical Impedance Spectroscopy (EIS) 7

1.7 Reference 8

Chapter 2 Enhanced corrosion resistance in aluminum-based electrolyzer components via stoichiometry tuned atomic layer deposited TiO_x film 12

2.1 Abstract 12

2.2 Introduction 12

2.3 Experimental section 16

2.4 Structural and elemental analysis through transmission electron microscopy (TEM) 20

2.5 Determining TiO_x stoichiometry by correlating energy dispersive spectroscopy (EDS) and Auger electron spectroscopy (AES) 21

2.6 Atomic force microscopy (AFM) study of the film topography 23

2.7 SEM/TEM and ICP-MS based analysis of the extent of corrosion of Al substrates.....25

2.8 Electrochemical analysis of the ALD TiO_x coating on Al substrates 30

2.9 Conclusions 33

2.10 Supporting Information 34

2.11 Acknowledgements.....43

2.12 References.....44

Chapter 3 TiO_x/Al_2O_3 laminate atomic layer deposited (ALD) films to enable corrosion prot4ection of aluminum screens and porous components in water electrolyzers.....49

3.1 Abstract.....49

3.2 Introduction 49

3.3 Experimental section 52

3.4 Surface treatment optimization.....57

3.5 Protection layer optimization 59

3.6 Electrochemical study for uncoated and optimal recipe coated Al screens 62

3.7 ALD penetration ability and distribution uniformity study.....67

3.8 Conclusion.....69

3.9 Supporting information 70

3.10 Acknowledgement 78

3.11 Reference 79

Chapter 4 Improved corrosion resistance and electrical characteristics of titanium, with atomic layer deposited (ALD) TiO_x coating.....85

4.1 Abstract.....85

4.2 Introduction 85

4.3 Experimental Section.....88

4.4 Oxide Formation as a Function of pH and Temperature.....91

4.5 Comparative ICP-MS analysis 95

4.6 Electrochemical analysis of ALD TiO_x coated *vs.* uncoated Ti substrates 96
4.7 Electrochemical impedance spectroscopy (EIS) analysis 99
4.8 Electrical conductivity variation of the uncoated and ALD coated Ti samples 102
4.9 Conclusion 103
4.10 Supporting Information 105
4.11 Acknowledgements 111
4.12 Reference 112

LIST OF FIGURES

Figure 1.1 Schematics of green hydrogen energy and water electrolyzers 1

Figure 1.2 A schematic model of general ALD binary reaction sequence 3

Figure 2.1 Schematic outline of the corrosion protection of Al substrate achieved by optimized ALD TiOx protection layers 16

Figure 2.2 TEM Imaging of 60 nm ALD TiO_x film on EP Al(1100) substrate after O_2 plasma clean 21

Figure 2.3 Auger Electron Spectroscopy (AES) and SEM Energy dispersive X-ray Spectroscopy (EDS) characterization on three representative recipes of ALD TiO_x 23

Figure 2.4 Atomic force microscopy (AFM) characterization of the as-deposited ALD TiO_x layers 25

Figure 2.5 SEM images related to the corrosion testing of Al with and without ALD TiO_x 26

Figure 2.6 The results from ICP-MS (inductively coupled plasma - mass spectroscopy) of the corrosion related elemental loss of Al (as Al^{3+}) and Ti (as Ti^{4+}) from three representative ALD recipes (R1, R2, and R3) for 60 nm TiO_x coating layers on EP Al 1100 28

Figure 2.7 TEM images of pinholes on ALD TiO_x and corroded Al after potentiostatic test 30

Figure 2.8 Electrical current variation observed in corrosion testing 31

Figure 3.1 Schematic representation 51

Figure 3.2 Schematic of fabrication processes related to corrosion protection layers 56

Figure 3.3 Characterization of surface treatment on corrosion resistance of Aluminum screens *prior* to ALD adhesion and protection layers 58

Figure 3.4 Characterization of the influence of adhesion and protection layers on corrosion resistance of Aluminum screens 60

Figure 3.5 Electrochemical characterization contrasting the behavior of uncoated and optimally coated Al screens 63

Figure 3.6 Evidence of ALD permeation and uniformity of stoichiometry through successive layers, in the flow field 68

Figure 4.1 Proposed Mechanism for Corrosion Protection by ALD TiOx 87

Figure 4.2 TEM characterization of anodic oxide on GR2 Ti after potentiostatic (PS) test in H_2SO_4 at 2.4 V (vs. RHE) 93

Figure 4.3 ICP-MS determination of the Ti (as Ti^{4+}), comparing uncoated Ti *with* ALD TiO_x coated Ti 95

Figure 4.4 Comparison of the electrical polarization characteristics of uncoated *vs.* ALD TiO_x coated GR2 Ti samples 97

Figure 4.5 EIS measurements and modeling of the uncoated and ALD TiO_x coated Ti samples 100

Figure 4.6 Current-voltage (J-V) characteristics before and after the PS testing 102

Supplemental Figure 2.1 SEM Images of ALD TiO_x deposited at different temperatures 37

Supplemental Figure 2.2 AES and EDS characterization on different ALD TiO_x 37

Supplemental Figure 2.3 Images of tested sample for corrosion test (potentiostatic test) 38

Supplemental Figure 2.4 ICP-MS calibration curve for Al and Ti ions 38

Supplemental Figure 2.5 ICP-MS characterization for ALD TiO_x temperature optimization 39

Supplemental Figure 2.6 ICP-MS characterization for ALD TiO_x purge time optimization 39

Supplemental Figure 2.7 Potentiostatic test of uncoated and ALD TiO_x coated Al substrate..... 40

Supplemental Figure 2.8 Polarization curves of uncoated and ALD TiO_x coated Al substrate ... 41

Supplemental Figure 2.9 Polarization curves of GR2 Ti 42

Supplemental Figure 2.10 Optical constant vs. nm of (a) Si and (b) TiO_x 43

Supplemental Figure 3.1 70

Supplemental Figure 3.2 Surface area estimation for Al screen sample 70

Supplemental Figure 3.3 Cross section transmission electron microscopy (TEM) characterization of the influence of surface treatment and ALD layers on Al screens 71

Supplemental Figure 3.4 Cross section transmission electron microscopy (TEM) of Al substrates, with the optimized surface treatment and subsequent coating..... 72

Supplemental Figure 3.5 TEM characterization of corrosion in Al screen due to pinholes in the ALD protection layer 73

Supplemental Figure 3.6 TEM and EDS characterization of oxide formed after oxygen plasma exposure of the substrate..... 73

Supplemental Figure 3.7 Determination of the Al^{3+} and Ti^{4+} concentration through ICP-MS analysis for ALD TiO_x coated Al screen subject to oxygen plasma treatment on one/single side and double/both sides after PS testing 74

Supplemental Figure 3.8 Schematic of processes related to the long purge (2s) and short purge (1s) ALD TiO_x 75

Supplemental Figure 3.9 Determination of the (a) Al^{3+} and (b) Ti^{4+} concentration through ICP-MS analysis of 50 nm TiO_x synthesized by long purge (2 s) ALD and short purge (1 s) ALD TiO_x coated on flat Al (MP Al 1100) and Al screens, after the PS testing..... 76

Supplemental Figure 3.10 EIS Nyquist plot for the high frequency (1250 Hz - 1MHz) region of uncoated and optimal recipe coated Al screens. 78

Supplemental Figure 4.1 Optical constant vs. wavelength (nm) 105

Supplemental Figure 4.2 Experimental setup for electrochemical testing 106

Supplemental Figure 4.3 Ellipsometry and TEM characterization of anodic film on GR2 Ti after potentiostatic (PS) test in H_2SO_4 at 2.4 V vs. RHE 107

Supplemental Figure 4.4 Thickness measured through ellipsometry, for ALD TiO_x coated Ti before and after the PS test 108

Supplemental Figure 4.5 ICP-MS results related to the elemental loss of Ti (as Ti^{4+}) as a function of time 108

Supplemental Figure 4.6 The current density as a function of time during the potentiostatic (PS) testing 109

Supplemental Figure 4.7 The current density (J) – voltage characteristics of ALD TiO_x-coated Ti, where the native oxide was wet etched by HF prior to ALD deposition 110

Supplemental Figure 4.8 Current density (*J*) - voltage characteristics for uncoated and ALD TiO_x coated Ti samples before and after the PS testing 111

LIST OF TABLES

Table 2.1 A comparison of the Tafel fit parameters of bare EP Al and ALD TiO_x coated EP Al substrates (using recipe R2) 32

Table 3.1 Tafel fitting parameters for the uncoated and optimally coated Al screens 64

Table 3.2 The obtained fits of the electrolyte resistance (R_s), porosity related resistance (R_{pore}), and the constant phase element (CPE) related to the film (Q_f) and double-layer characteristics (Q_{dl}) and associated exponents (α_f and α_{dl}) 66

Table 4.1 Comparison of the Tafel fit parameters of uncoated and ALD TiO_x coated GR2 Ti ... 97

Table 4.2 Fit parameters from modeling of the EIS spectra for GR2 Ti without *and* with 30 nm of ALD TiO_x coating at pH 3 and 80°C 100

Supplemental Table 2.1 Detailed information of different Al substrates 34

Supplemental Table 2.2 ICP-MS results of 50 nm R2 (150 ms $TiCl_4$ + 2 s purge + 50 ms H_2O + 2 s purge) ALD TiO_x coated on different Al substrate after potentiostatic test in 1 mM H_2SO_4 at 2.4 V vs. NHE 35

Supplemental Table 2.3 Reported test metal concentration in the 67-70% trace metal grade nitric acid 35

Supplemental Table 2.4 Tafel fit parameters of uncoated and ALD TiO_x coated EP Al 1100 36

Supplemental Table 2.5 ICP-MS results of repeat test for 50 nm ALD TiO_x coated with different recipe on EP Al substrate after potentiostatic test in 1 mM H_2SO_4 at 2.4 V vs. NHE 36

Supplemental Table 3.1 Benefits of each optimized process 77

ACKNOWLEDGEMENTS

First and foremost, I would like to express my sincere gratitude to Professor Prabhakar R. Bandaru and Professor Andrew C. Kummel for their unwavering support and guidance throughout my Ph.D. journey. As my academic advisors and the chair and co-chair of my committee, their mentorship has been instrumental in shaping both my research and professional development. Their insightful feedback, generous time, and innovative research ideas were invaluable during the many drafts and long nights of this work. I am especially thankful for their encouragement and advice, which enabled me to grow as a researcher and explore new career opportunities beyond academia. I also deeply appreciate their guidance in improving my communication and presentation skills, which has had a lasting impact on my academic and professional confidence. I consider myself truly fortunate to have had the opportunity to work under their mentorship. Their patience, expertise, and dedication have made a profound difference in my academic journey, and I am deeply honored to be their student.

Secondly, I would like to express my sincere appreciation to the members of my dissertation committee, Professor David Saintillan and Professor Yu Qiao. Their valuable insights, thoughtful suggestions, and constructive feedback provided crucial direction and clarity to my research. Their guidance played an important role in shaping the scope and depth of this thesis, and I am grateful for their time and expertise.

Next, I would like to extend my sincere gratitude to Dr. Adam Paxon, Dr. Thomas I. Valdez, Dr. Ahmet Gün Erlat, and Yaneth Hernandez for their collaboration in developing corrosion-resistant solutions for PEMWEs. I greatly appreciate the valuable discussions and collective efforts in overcoming the many challenges we faced. I would also like to thank Dr. Neal Arakawa for his generous support and guidance with ICP-MS analysis. His expertise in both the

operation of the instrument and the interpretation of data was instrumental to the completion of this work. Additionally, I am grateful to Patrick Driscoll, Dr. Xuekun Lu, and the rest of the Nano3 cleanroom staff for their consistent support, training, and dedication to maintaining an excellent research environment.

I would also like to thank all my group members and collaborators for their generous support and contributions throughout my research. I am especially grateful to Ping-Che Lee for assistance with TEM characterization and to Dr. Seonguk Yun for his help with AES analysis. I sincerely thank Dr. Zichen Zhang for his patience and guidance with ALD, PECVD, PVD, and semiconductor fabrication processes. I also extend my appreciation to Dr. Yongliang Dong, Dr. Yun Zhou, Dr. Li Cheng, Dr. Alex Lee, Dr. Dohyun Go, Dr. Dipayan Pal, Dr. Hidenori Yamada, Shreyam Natani, Kassra Eshraghi, Pranjali Khajanji, Ramteja Kondakindi, Hyochul Ahn, Seong Yang, Seyeon Park, and Anirudh Ramanathan for their invaluable support, collaboration, and encouragement throughout this journey.

Finally, I would like to express my deepest gratitude to my family and friends for their unwavering support throughout my life. Your understanding, encouragement, and belief in me have been the foundation of my personal and academic journey. I would not be who I am today without your constant presence and support.

Chapter 2, in full, is a reprint of the material as it appears in "Enhanced Corrosion Resistance in Aluminum-Based Electrolyzer Components via Stoichiometry Tuned Atomic Layer-Deposited TiO_x Films." *ACS Applied Materials & Interfaces* 16, no. 27 (2024): 35043-35052 by Kesong Wang, Adam Paxson, Thomas I. Valdez, Ahmet Erlat, Ping-Che Lee, Seonguk Yun, Pranjali Khajanji, Zichen Zhang, Andrew C. Kummel, and Prabhakar Bandaru. The dissertation author was the primary investigator and author of this paper.

Chapter 3, in full, is a reprint with permission from Kesong Wang, "TiO_x/Al_2O_3 laminate atomic layer deposited (ALD) films to enable corrosion protection of aluminum screens and porous components in water electrolyzers", manuscript submitted to *ACS Applied Materials & Interfaces*, by Kesong Wang, Adam Paxson, Thomas I. Valdez, Ahmet Gün Erlat, Ping-Che Lee, Andrew C. Kummel, Prabhakar R. Bandaru. The dissertation author was the primary researcher and author of this paper.

Chapter 4, in full, is a reprint of the material as it appears in "Improved corrosion resistance and electrical characteristics of titanium, with atomic layer deposited (ALD) TiO_x coating." *Applied Surface Science* 692 (2025): 162719 by Kesong Wang, Adam Paxson, Thomas I. Valdez, Ahmet G. Erlat, Ping-Che Lee, Seonguk Yun, Andrew C. Kummel, and Prabhakar R. Bandaru. The dissertation author was the primary researcher and author of this material.

VITA

2017 Bachelor of Science in Theoretical and Applied Mechanics, Lanzhou University

2018 Master of Science in Mechanical Engineering, Wahington University in St. Louis

2025 Doctor of Philosophy in Engineering Sciences (Mechanical Engineering), University of California San Diego

ABSTRACT OF THE DISSERTATION

A study on enhanced electrochemical stability in water electrolysis components, via stoichiometry tuned atomic layer deposited films

by

Kesong Wang

Doctor of Philosophy in Engineering Sciences (Mechanical Engineering)

University of California San Diego, 2025

Professor Prabhakar R. Bandaru, Chair
Professor Andrew C. Kummel, Co-Chair

This dissertation explores advanced surface engineering strategies to enhance the corrosion resistance of metallic components in proton exchange membrane (PEM) water electrolyzers, with a focus on replacing costly titanium (Ti) with more abundant and thermally conductive aluminum (Al). Through the application of atomic layer deposition (ALD) techniques, conformal and robust titanium oxide (TiO_x) coatings were developed and optimized to provide long-term protection under industrially relevant electrochemical conditions, low pH, high voltage (>2.4 V), and elevated temperature (up to 80°C).

The chapter two demonstrates that pinhole-free, oxygen-vacancy-rich TiO_x coatings significantly improve the corrosion resistance of Al substrates, achieving dissolution rates as low as ~6 nm per year and enabling projected lifetimes of up to 60,000 hours for PEM anode current collectors. The chapter three extends this approach to complex geometries, applying a multi-step surface treatment including electropolishing, O_2 treatment, and a multi-layer ALD structure on Al gas diffusion layer components, reducing corrosion rates by four orders of magnitude. The chapter four focuses on Ti itself, showing that thin ALD TiO_x coatings drastically reduce corrosion and current degradation, achieving a five orders of magnitude improvement in current stability compared to uncoated Ti.

Collectively, these studies offer a scalable and cost-effective pathway to substitute Ti with Al in critical electrolyzer components, while extending device longevity through nanoscale engineering of corrosion-resistant coatings. This work advances the deployment of affordable hydrogen production technologies by addressing material limitations in PEM electrolyzer systems.

Chapter 1 Introduction

1.1 Hydrogen Energy and the Role of Water Electrolyzers

The transition to a sustainable energy future necessitates the development of clean, scalable, and dispatchable energy carriers. Hydrogen (H_2) has emerged as a critical vector in this context due to its high energy density[1], versatility[2], and carbon-free combustion[3]. When generated from renewable sources, hydrogen offers a pathway to decarbonize hard-to-abate sectors such as steel production[4], ammonia synthesis[5], heavy transportation[4,5], and long-duration energy storage[6] as shown in **Fig. 1.1a**.

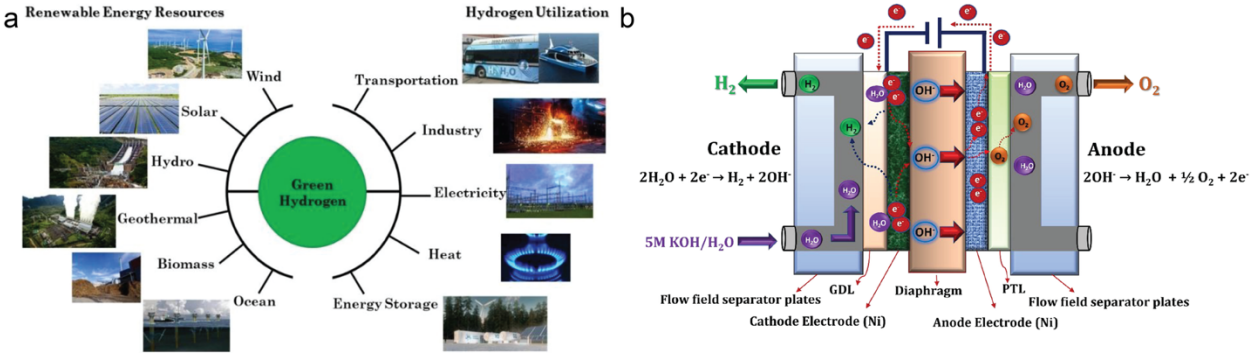


Figure 1.1 Schematics of green hydrogen energy and water electrolyzers, **(a)** renewable energy source for green hydrogen energy production and its applications[7], **(b)** Schematic of proton exchange membrane (PEM) water electrolyzers[8]

Among the various methods of hydrogen production, water electrolysis, the splitting of water (H_2O) into hydrogen and oxygen (O_2) using electricity (**Fig. 1.1b)**, is particularly promising. When powered by renewable energy sources shown in **Fig. 1.1a** such as wind or solar, water electrolysis enables the production of green hydrogen, yielding zero direct emissions and establishing a direct link between variable renewable electricity and storable chemical energy[7].

Several electrolyzer technologies exist, including alkaline electrolysis, solid oxide electrolysis, and proton exchange membrane (PEM) electrolysis[9]. Among these, PEM water

electrolyzers are gaining increased attention due to their compact design, rapid response to power fluctuations, high current densities, and suitability for integration with intermittent renewable energy sources[10].

1.2 Challenges in PEM Water Electrolyzer Materials

Despite their advantages, PEM electrolyzers face significant challenges related to materials durability and cost. Operating conditions in PEM systems are highly aggressive, characterized by low pH (acidic environment), high anodic potentials (>2.0 V vs. RHE), and elevated temperatures (typically 60–80°C)[11]. Under such conditions, conventional materials are prone to corrosion and performance degradation.

Titanium (Ti) has been widely adopted for key components such as bipolar plates, anode flow fields, and gas diffusion layers due to its strong corrosion resistance[11,12]. However, Ti's high material cost and machining complexity pose barriers to large-scale deployment of PEM technology. Substituting Ti with more abundant and cost-effective materials like aluminum (Al) could significantly lower system costs, but Al suffers from rapid corrosion in acidic, oxidizing conditions.

To address these issues, research has increasingly focused on developing protective coatings and surface treatments that enable the use of alternative metals in electrolyzer environments without compromising durability or performance[12,13]. In particular, atomic layer deposition (ALD) has emerged as a promising technique to fabricate ultrathin, conformal, and corrosion-resistant coatings tailored for harsh electrochemical environments[14–16].

1.3 Atomic Layer Deposition (ALD) for Corrosion Protection

Atomic Layer Deposition (ALD) is a thin-film deposition technique distinguished by its ability to produce highly conformal, pinhole-free, and atomically controlled coatings, even on substrates with complex geometries or high aspect ratios[17–19]. It is particularly well-suited for applications that demand precise control over film thickness, stoichiometry, and uniformity—traits that are critically important for protective coatings in harsh environments such as proton exchange membrane (PEM) electrolyzers.

ALD is based on a sequential, self-limiting surface reaction process in which precursor gases are pulsed alternately into a reaction chamber[20]. Each precursor pulse reacts with the surface in a self-limiting manner, allowing for monolayer-by-monolayer film growth as shown in **Fig. 1.2**[21]. This atomic-level control enables the formation of ultrathin and dense oxide films, such as titanium oxide (TiOx) and aluminum oxide (Al_2O_3), with exceptional precision and repeatability[22].

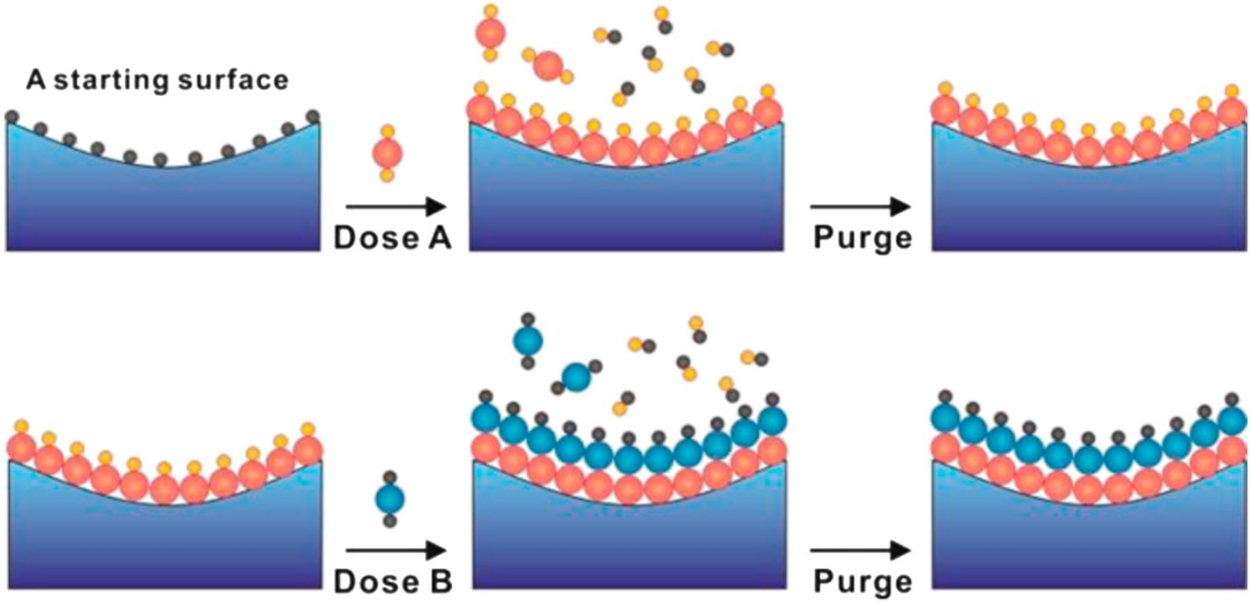


Figure 1.2 A schematic model of general ALD binary reaction sequence[21]. Precursor A and B are sequentially introduced to a substrate surface with inert gas purging in between.

In the context of corrosion protection, ALD films serve as diffusion barriers that limit the transport of corrosive species, such as H^+, O_2, and H_2O molecules, to the underlying metal substrate[15,23,24]. By tailoring the composition, crystalline phase, and oxygen vacancy concentration of the coating, it is possible to engineer films with high electrochemical stability, minimal dissolution rates, and excellent adhesion[25].

Moreover, ALD is compatible with both planar and textured surfaces[21], making it ideal for electrolyzer components such as gas diffusion layers (GDLs), flow fields, and current collectors that often exhibit intricate surface morphology. When applied to metals like aluminum or titanium, ALD coatings can dramatically extend component lifetime under acidic and oxidizing conditions typical of PEM electrolyzers, while enabling the use of lower-cost base materials.

Recent advancements in ALD process development, including multilayer and doped coatings, have further expanded its utility in energy conversion and storage systems[16,26]. The ability to precisely tune film characteristics at the nanoscale makes ALD a powerful tool in designing corrosion-resistant materials tailored to the specific demands of high-performance electrochemical devices.

1.4 Electrochemical Characterization: Potentiostatic and Potentiodynamic Techniques

Understanding and quantifying the corrosion resistance of materials in aggressive electrochemical environments, such as those present in proton exchange membrane (PEM) water electrolyzers, requires precise and reliable testing methodologies. Among the most widely employed techniques for evaluating corrosion behavior are potentiostatic and potentiodynamic electrochemical tests. These methods provide essential insights into the stability, durability, and

electrochemical degradation mechanisms of coated and uncoated materials under relevant operating conditions[27,28].

Potentiostatic testing involves maintaining a constant electrode potential relative to a reference electrode while measuring the resulting current over time. This technique is particularly useful for simulating long-term exposure to specific anodic potentials, such as those encountered at the anode side of PEM electrolyzers. The current-time behavior during potentiostatic holds reveals important information about the passivation quality, electrochemical stability, and the potential breakdown or degradation of protective coatings[29]. A low, stable current typically indicates strong resistance to corrosion and minimal charge transfer at the interface.

In contrast, potentiodynamic polarization involves sweeping the electrode potential at a fixed rate and recording the current response to generate a polarization curve. This curve reveals key electrochemical characteristics including the corrosion potential (E_corr), corrosion current density (i_corr), and regions of passivation and transpassive behavior[30]. These metrics are critical for assessing both the thermodynamic propensity and kinetic rate of corrosion processes. The shape and features of the polarization curve allow identification of protective behavior and the onset of localized or uniform corrosion[30].

These electrochemical methods are typically conducted under conditions that mimic the operating environment of PEM electrolyzers—such as low pH electrolytes (e.g., < pH5 H_2SO_4), elevated temperatures, and high anodic potentials (up to 2.4 V vs. reference electrodes)[11]. Such rigorous testing protocols help screen materials and coatings for durability in real-world scenarios.

In this dissertation, potentiostatic and potentiodynamic techniques are employed systematically to evaluate the performance of atomic layer deposited (ALD) coatings on aluminum and titanium substrates. These methods enable the quantification of corrosion resistance and offer

insight into the protective mechanisms of engineered thin films, supporting the development of cost-effective and durable components for water electrolysis applications.

1.5 Inductive Coupled Plasma Mass Spectrometry (ICP-MS)

Inductively Coupled Plasma Mass Spectrometry (ICP-MS) is a highly sensitive analytical technique used for the detection and quantification of trace elements in liquid samples[31]. It is particularly valuable in materials science and electrochemistry for measuring metal dissolution rates, enabling precise evaluation of corrosion resistance in coated and uncoated materials under aggressive electrochemical conditions.

The ICP-MS technique operates by nebulizing a liquid sample into a fine aerosol, which is then introduced into a high-temperature argon plasma (~6000–10000 K)[32]. Within the plasma, the sample is atomized and ionized, producing positively charged ions that are extracted into a mass spectrometer. These ions are then separated based on their mass-to-charge (m/z) ratios, allowing for highly accurate and selective detection of elements at part-per-billion (ppb) to part-per-trillion (ppt) levels[33].

In the context of this dissertation, ICP-MS serves as a complementary tool to electrochemical techniques, providing quantitative data on the dissolution of key metals such as aluminum (Al) and titanium (Ti) from substrate or coating materials. This allows for direct measurement of material loss during potentiostatic corrosion tests and enables estimation of coating durability and lifetime under PEM water electrolyzer-relevant conditions.

ICP-MS is especially advantageous for evaluating low corrosion rates, where traditional weight loss or visual inspection methods lack the necessary sensitivity. By quantifying the exact amount of dissolved metal ions in the electrolyte after electrochemical exposure, ICP-MS offers

critical validation of protective coating performance and facilitates the optimization of coating compositions and deposition parameters.

In this research, ICP-MS is employed to assess the dissolution behavior of ALD-deposited TiOx coatings on aluminum and titanium substrates, thereby supporting the development of corrosion-resistant, cost-effective alternatives to conventional titanium components in PEM electrolyzers.

1.6 Electrochemical Impedance Spectroscopy (EIS)

Electrochemical Impedance Spectroscopy (EIS) is a powerful, non-destructive analytical technique used to investigate the electrochemical behavior and interfacial properties of materials in electrolyte environments[34,35]. It plays a crucial role in the characterization of corrosion resistance, coating performance, and electrode kinetics—making it particularly valuable in the development of materials for proton exchange membrane (PEM) water electrolyzers.

EIS measures the impedance response of an electrochemical system over a range of frequencies, typically from millihertz to hundreds of kilohertz, by applying a small sinusoidal voltage perturbation and measuring the resulting current[36]. The impedance data are commonly presented in Nyquist or Bode plots and can be interpreted through equivalent circuit models that describe charge transfer resistance, double-layer capacitance, diffusion processes, and coating properties[37,38].

In the context of corrosion studies, EIS enables the distinction between resistive and capacitive behavior at the metal-electrolyte interface, providing insight into the integrity and protective quality of surface coatings[39]. For instance, a high charge transfer resistance and a

capacitive response typically indicate effective corrosion protection and minimal electrochemical activity at the surface.

This technique is particularly suited for evaluating thin conformal coatings such as those produced by Atomic Layer Deposition (ALD), where conventional testing may fail to resolve subtle interfacial changes. EIS can detect early degradation phenomena and provide quantitative parameters such as coating resistance, pore resistance, and capacitance, which are essential for predicting long-term durability under electrolysis-relevant conditions (e.g., low pH, high voltage, elevated temperatures).

In this dissertation, EIS is utilized to complement potentiostatic and potentiodynamic corrosion testing by providing a frequency-resolved understanding of the electrochemical performance of TiOx-coated aluminum and titanium substrates. The insights gained through EIS help validate the effectiveness of ALD coatings in mitigating corrosion and support the design of robust, cost-effective materials for PEM electrolyzer applications.

1.7 Reference

(1) Yue, M.; Lambert, H.; Pahon, E.; Roche, R.; Jemei, S.; Hissel, D. Hydrogen Energy Systems: A Critical Review of Technologies, Applications, Trends and Challenges. *Renewable and Sustainable Energy Reviews* **2021**, *146*, 111180. https://doi.org/10.1016/j.rser.2021.111180.

(2) Amez Arenillas, I.; Ortega, M. F.; García Torrent, J.; Llamas Moya, B. Hydrogen as an Energy Vector: Present and Future. In *Sustaining Tomorrow via Innovative Engineering*; WORLD SCIENTIFIC, 2021; pp 83–129. https://doi.org/10.1142/9789811228032_0003.

(3) Pitsch, H. The Transition to Sustainable Combustion: Hydrogen- and Carbon-Based Future Fuels and Methods for Dealing with Their Challenges. *Proceedings of the Combustion Institute* **2024**, *40* (1–4), 105638. https://doi.org/10.1016/j.proci.2024.105638.

(4) Franco, A.; Giovannini, C. Routes for Hydrogen Introduction in the Industrial Hard-to-Abate Sectors for Promoting Energy Transition. *Energies (Basel)* **2023**, *16* (16), 6098. https://doi.org/10.3390/en16166098.

(5) Jayachandran, M.; Gatla, R. K.; Flah, A.; Milyani, A. H.; Milyani, H. M.; Blazek, V.; Prokop, L.; Kraiem, H. Challenges and Opportunities in Green Hydrogen Adoption for Decarbonizing Hard-to-Abate Industries: A Comprehensive Review. *IEEE Access* **2024**, *12*, 23363–23388. https://doi.org/10.1109/ACCESS.2024.3363869.

(6) Cheekatamarla, P. Hydrogen and the Global Energy Transition—Path to Sustainability and Adoption across All Economic Sectors. *Energies (Basel)* **2024**, *17* (4), 807. https://doi.org/10.3390/en17040807.

(7) Agaton, C. B.; Batac, K. I. T.; Reyes Jr., E. M. Prospects and Challenges for Green Hydrogen Production and Utilization in the Philippines. *Int J Hydrogen Energy* **2022**, *47* (41), 17859–17870. https://doi.org/10.1016/j.ijhydene.2022.04.101.

(8) Shiva Kumar, S.; Lim, H. An Overview of Water Electrolysis Technologies for Green Hydrogen Production. *Energy Reports* **2022**, *8*, 13793–13813. https://doi.org/10.1016/j.egyr.2022.10.127.

(9) Sebbahi, S.; Nabil, N.; Alaoui-Belghiti, A.; Laasri, S.; Rachidi, S.; Hajjaji, A. Assessment of the Three Most Developed Water Electrolysis Technologies: Alkaline Water Electrolysis, Proton Exchange Membrane and Solid-Oxide Electrolysis. *Mater Today Proc* **2022**, *66*, 140–145. https://doi.org/10.1016/j.matpr.2022.04.264.

(10) Salehmin, M. N. I.; Husaini, T.; Goh, J.; Sulong, A. B. High-Pressure PEM Water Electrolyser: A Review on Challenges and Mitigation Strategies towards Green and Low-Cost Hydrogen Production. *Energy Convers Manag* **2022**, *268*, 115985. https://doi.org/10.1016/j.enconman.2022.115985.

(11) Ahmed, K. W.; Jang, M. J.; Park, M. G.; Chen, Z.; Fowler, M. Effect of Components and Operating Conditions on the Performance of PEM Electrolyzers: A Review. *Electrochem* **2022**, *3* (4), 581–612. https://doi.org/10.3390/electrochem3040040.

(12) Liu, T.; Tao, Y.; Wang, Y.; Hu, M.; Zhang, Z.; Shao, J. Towards Cost-Effective and Durable Bipolar Plates for Proton Exchange Membrane Electrolyzers: A Review. *Fuel* **2024**, *368*, 131610. https://doi.org/10.1016/j.fuel.2024.131610.

(13) Liu, T.; Tao, Y.; Wang, Y.; Wu, M.; Zhang, J.; Yu, Y.; Wang, X.; Shao, J. Thermal Sprayed Protective Coatings for Bipolar Plates of Hydrogen Fuel Cells and Water Electrolysis Cells. *Coatings* **2024**, *14* (3), 307. https://doi.org/10.3390/coatings14030307.

(14) Liu, X.; Su, Y.; Chen, R. Atomic-Scale Engineering of Advanced Catalytic and Energy Materials via Atomic Layer Deposition for Eco-Friendly Vehicles. *International Journal of Extreme Manufacturing* **2023**, *5* (2), 022005. https://doi.org/10.1088/2631-7990/acc6a7.

(15) Singh, A. K.; Adstedt, K.; Brown, B.; Singh, P. M.; Graham, S. Development of ALD Coatings for Harsh Environment Applications. *ACS Appl Mater Interfaces* **2019**, *11* (7), 7498–7509. https://doi.org/10.1021/acsami.8b11557.

(16) Gupta, B.; Hossain, Md. A.; Riaz, A.; Sharma, A.; Zhang, D.; Tan, H. H.; Jagadish, C.; Catchpole, K.; Hoex, B.; Karuturi, S. Recent Advances in Materials Design Using Atomic Layer Deposition for Energy Applications. *Adv Funct Mater* **2022**, *32* (3). https://doi.org/10.1002/adfm.202109105.

(17) Pakkala, A.; Putkonen, M. Atomic Layer Deposition. In *Handbook of Deposition Technologies for Films and Coatings*; Elsevier, 2010; pp 364–391. https://doi.org/10.1016/B978-0-8155-2031-3.00008-9.

(18) Cremers, V.; Puurunen, R. L.; Dendooven, J. Conformality in Atomic Layer Deposition: Current Status Overview of Analysis and Modelling. *Appl Phys Rev* **2019**, *6* (2). https://doi.org/10.1063/1.5060967.

(19) Zhang, Z.; Passlack, M.; Pitner, G.; Kuo, C.-H.; Ueda, S. T.; Huang, J.; Kashyap, H.; Wang, V.; Spiegelman, J.; Lam, K.-T.; Liang, Y.-C.; Liew, S. L.; Hsu, C.-F.; Kummel, A. C.; Bandaru, P. Sub-Nanometer Interfacial Oxides on Highly Oriented Pyrolytic Graphite and Carbon Nanotubes Enabled by Lateral Oxide Growth. *ACS Appl Mater Interfaces* **2022**, *14* (9), 11873–11882. https://doi.org/10.1021/acsami.1c21743.

(20) Lu, J.; Elam, J. W.; Stair, P. C. Atomic Layer Deposition—Sequential Self-Limiting Surface Reactions for Advanced Catalyst "Bottom-up" Synthesis. *Surf Sci Rep* **2016**, *71* (2), 410–472. https://doi.org/10.1016/j.surfrep.2016.03.003.

(21) Lu, J.; Elam, J. W.; Stair, P. C. Synthesis and Stabilization of Supported Metal Catalysts by Atomic Layer Deposition. *Acc Chem Res* **2013**, *46* (8), 1806–1815. https://doi.org/10.1021/ar300229c.

(22) Cao, L.; Lu, J. Atomic-Scale Engineering of Metal–Oxide Interfaces for Advanced Catalysis Using Atomic Layer Deposition. *Catal Sci Technol* **2020**, *10* (9), 2695–2710. https://doi.org/10.1039/D0CY00304B.

(23) Scheuermann, A. G.; McIntyre, P. C. Atomic Layer Deposited Corrosion Protection: A Path to Stable and Efficient Photoelectrochemical Cells. *J Phys Chem Lett* **2016**, *7* (14), 2867–2878. https://doi.org/10.1021/acs.jpclett.6b00631.

(24) Abdulagatov, A. I.; Yan, Y.; Cooper, J. R.; Zhang, Y.; Gibbs, Z. M.; Cavanagh, A. S.; Yang, R. G.; Lee, Y. C.; George, S. M. Al_2O_3 and TiO_2 Atomic Layer Deposition on Copper for Water Corrosion Resistance. *ACS Appl Mater Interfaces* **2011**, *3* (12), 4593–4601. https://doi.org/10.1021/am2009579.

(25) Wang, Q.; Cheng, Y.; Tao, H. B.; Liu, Y.; Ma, X.; Li, D.; Yang, H. Bin; Liu, B. Long-Term Stability Challenges and Opportunities in Acidic Oxygen Evolution Electrocatalysis. *Angewandte Chemie* **2023**, *135* (11). https://doi.org/10.1002/ange.202216645.

(26) Zhao, Y.; Zhang, L.; Liu, J.; Adair, K.; Zhao, F.; Sun, Y.; Wu, T.; Bi, X.; Amine, K.; Lu, J.; Sun, X. Atomic/Molecular Layer Deposition for Energy Storage and Conversion. *Chem Soc Rev* **2021**, *50* (6), 3889–3956. https://doi.org/10.1039/D0CS00156B.

(27) Saji, V. S. Corrosion and Materials Degradation in Electrochemical Energy Storage and Conversion Devices. *ChemElectroChem* **2023**. https://doi.org/10.1002/celc.202300136.

(28) Moradi, M.; Vasseghian, Y.; Khataee, A.; Kobya, M.; Arabzade, H.; Dragoi, E.-N. Service Life and Stability of Electrodes Applied in Electrochemical Advanced Oxidation Processes: A Comprehensive Review. *Journal of Industrial and Engineering Chemistry* **2020**, *87*, 18–39. https://doi.org/10.1016/j.jiec.2020.03.038.

(29) Tomashov, N. D. *Passivity and Protection of Metals against Corrosion*; Springer Science & Business Media, 2012.

(30) Dhawan, S. K.; Bhandari, H.; Ruhi, G.; Bisht, B. M. S.; Sambyal, P. *Corrosion Preventive Materials and Corrosion Testing*; CRC Press, 2020. https://doi.org/10.1201/9781315101217.

(31) Ammann, A. A. Inductively Coupled Plasma Mass Spectrometry (ICP MS): A Versatile Tool. *Journal of Mass Spectrometry* **2007**, *42* (4), 419–427. https://doi.org/10.1002/jms.1206.

(32) Thompson, M. *Handbook of Inductively Coupled Plasma Spectrometry*; Springer Science & Business Media, 2012.

(33) Medhe, S. Ionization Techniques in Mass Spectrometry: A Review. *Mass Spectrom Purif Tech* **2018**, *04* (01). https://doi.org/10.4172/2469-9861.1000126.

(34) Bandarenka, A. S. Exploring the Interfaces between Metal Electrodes and Aqueous Electrolytes with Electrochemical Impedance Spectroscopy. *Analyst* **2013**, *138* (19), 5540. https://doi.org/10.1039/c3an00791j.

(35) Magar, H. S.; Hassan, R. Y. A.; Mulchandani, A. Electrochemical Impedance Spectroscopy (EIS): Principles, Construction, and Biosensing Applications. *Sensors* **2021**, *21* (19), 6578. https://doi.org/10.3390/s21196578.

(36) Lazanas, A. Ch.; Prodromidis, M. I. Electrochemical Impedance Spectroscopy─A Tutorial. *ACS Measurement Science Au* **2023**, *3* (3), 162–193. https://doi.org/10.1021/acsmeasuresciau.2c00070.

(37) Cesiulis, H.; Tsyntsaru, N.; Ramanavicius, A.; Ragoisha, G. The Study of Thin Films by Electrochemical Impedance Spectroscopy; 2016; pp 3–42. https://doi.org/10.1007/978-3-319-30198-3_1.

(38) Huang, J.; Li, Z.; Liaw, B. Y.; Zhang, J. Graphical Analysis of Electrochemical Impedance Spectroscopy Data in Bode and Nyquist Representations. *J Power Sources* **2016**, *309*, 82–98. https://doi.org/10.1016/j.jpowsour.2016.01.073.

(39) Herrera Hernández, H.; M. Ruiz Reynoso, A.; C. Trinidad González, J.; O. González Morán, C.; G. Miranda Hernández, J.; Mandujano Ruiz, A.; Morales Hernández, J.; Orozco Cruz, R. Electrochemical Impedance Spectroscopy (EIS): A Review Study of Basic Aspects of the Corrosion Mechanism Applied to Steels. In *Electrochemical Impedance Spectroscopy*; IntechOpen, 2020. https://doi.org/10.5772/intechopen.94470.

Chapter 2 Enhanced corrosion resistance in aluminum-based electrolyzer components via stoichiometry tuned atomic layer deposited TiO_x film

2.1 Abstract

Titanium (Ti) is widely used as anode current collectors in proton exchange membrane (PEM) based water electrolyzers due to its self-passivated oxide layer which protects it from corrosion in acidic solutions. However, the cost of material and machining process for Ti is high. A wider utilization of water electrolyzers to produce hydrogen could be favored by the use of less expensive coated aluminum (Al) substrates, which could potentially replace high-cost Ti based components. It is shown here by depositing a pinhole-free oxygen vacancy rich titanium oxide (TiOx) protection layer by atomic layer deposition (ALD), the corrosion resistance of Al substrates in acidic environments at oxygen evolution potentials can be enhanced. The optimization of the oxygen vacancy concentration is accomplished by tuning the ALD parameters to achieve ideal stoichiometry and conformal coating on rough substrates. The robustness of the coatings was evaluated at high potentials (2.4V vs. NHE - normal hydrogen electrode) in low pH conditions. A low TiOx dissolution rate of the order of ~ 6 nm year-1 was observed. By testing under industrially relevant conditions, i.e., high applied voltages (2.4 V) and low pH, an Al loss at around zero-ppb level was achieved using optimized ALD parameters. It is proposed that a 40 nm TiOx coating on Al may be adequate to provide 60,000 hours of durability in a PEM water electrolyzer anode current collector.

2.2 Introduction

The production of green hydrogen[1] using renewable energy sources may be implemented via water electrolysis.[2] Water electrolyzers are typically operated at large overpotentials, *i.e.,* at

greater than 1.23 V (*vs*. NHE) - the minimum potential difference needed for the splitting of water into hydrogen and oxygen, per thermodynamic considerations[3,4], and at low pH conditions[5] for enhanced efficiency[6,7]. Titanium (Ti) has been a favored material for water electrolyzer current collectors and other components[8,9] due to its electrochemical stability under oxygen evolution potentials in acidic media – as may be deduced from the relevant Pourbaix diagram[10] The formation of a surface passivation layer associated with the Ti minimizes loss of material, preventing damage to the proton exchange membrane (PEM)[11,12].

A major issue relevant to use of Ti in electrolyzers is its cost and limited availability[13,14] with the implication the high-volume production of green hydrogen would be less attractive from a supply chain and economic perspective. Aluminum (Al) is an order of magnitude less expensive and more abundant compared to Ti, while possessing attractive attributes compared to Ti such as lower density, higher electrical conductivity, and higher thermal conductivity[15]. Furthermore, the mechanical strength of Al alloys could be comparable to Ti[16], while allowing for easier fabrication and lower component production costs[17]. While the corrosion resistance for Al has been reported to be inferior compared to Ti, especially at low and high pH[18,19], the present study shows that such issues could be remedied by the deposition of carefully optimized conformal thin films of TiO_x (with $x \sim 1.35$, as measured with Auger electron spectroscopy : AES) onto the Al substrate.

TiO_x coated Al potentially combines the well-known robustness to environmental degradation of the titanium oxides with the economic and physical advantages of Al. Previous reports of corrosion protection of metallic substrates have typically utilized line-of-sight based physical (/chemical) vapor deposition (P-/C-VD) methods[20–22], for the related coatings. Further, studies of corrosion resistant coatings for harsh environment applications deposited through atomic layer deposition (ALD)[23–28] are limited. ALD films have been shown to possess higher resistance

to ambient chemical degradation due to (a) conformality - diminishing the role of intrinsic substrate roughness through the possibility of coating porous structure[29], and (b) ability for tuning the film crystallinity and stoichiometry[25]. A related significant advantage of ALD, compared to PVD or CVD coating-based corrosion protection, is an ability to reduce the influence of pinhole type defects[30,31].

It was previously reported that ultrathin (5-60 nm) ALD TiO_x could serve as an effective moisture permeation barrier[32] and was corrosion resistant to 0.1 M NaCl (pH = 7) solutions[33]. It was indicated that the nominal oxide on titanium is intrinsically constituted of two layers, with the inner layer being one of a lower oxidation state with a smaller rate of dissolution in diluted sulfuric acidic[34]. However, there does not seem to be adequate insights into the durability of ALD coatings under harsh electrophysical conditions, *i.e.,* at extremes of pH, applied voltages, *etc.* as relevant to electrolyzers such as pH of 3 and applied voltages of 2.4V (*vs.* NHE). Furthermore, the significance of the oxygen content of the ALD titanium oxide, has not been actively investigated. For instance, it is well known that TiO_2 (titanium dioxide) with a O : Ti ratio closer to 2 has insulating character while a smaller ratio would imply more semiconducting attributes[35]. A semiconducting TiO_x may be advantageous due to the associated possibility of less reactivity compared to bulk rutile TiO_2[36].

In the present study, the stoichiometry and consequent Ti oxidation state of the TiO_x were tuned by adjusting the $TiCl_4$ and H_2O precursor pulse lengths. The present study shows optimized oxygen vacancy rich TiO_x coating (on Al substrates) was robust over days of testing in 1 mM H_2SO_4 at 2.4 V (*vs*. NHE), and the corrosion resistance of Al was improved by orders of magnitude. An optimized TiO_x coating has a rate of dissolution at the level of ~ 6 nm $year^{-1}$. The characteristics of such coatings were thoroughly investigated by imaging including scanning and

transmission electron microscopy and atomic force microscopy, as well as by analytical methods including Auger electron spectroscopy and electrochemistry measurements. The use of oxygen vacancy rich ALD TiO_x coatings opens new avenues in their utilization for economically fabricated electrolyzer components. It was shown that a thin film coating of thickness ~ 40 nm on Al could last the lifetime (~ 60,000 hours) of a typical electrolyzer stack[37] if it is assumed that the corrosion current has reached a steady state value after ~ 50 hours of testing.

Atomic layer deposition (ALD) of titanium oxide on Al substrates (see Table **S2.1** of the *Supporting Information*) , as schematically indicated in **Fig. 2.1 (a),** was performed using variable ALD pulsing schemes (as indicated in detail in *Section 2.2 – Experimental Section*). The sequence of steps related to the conformal ALD of the TiO_x is indicated in **Fig. 2.1 (b)**. The coated substrates were subjected to electrochemical testing, under controlled and standard conditions, for determining the robustness of the coatings at low pH (~ 3) at large applied voltages (2.4 V *vs*. NHE): **Fig. 2.1(c).** Corrosion pits were observed on the uncoated substrate due to the interaction of the substrate with the 1 mM H_2SO_4 solution, while the ALD TiO_x protected substrate indicated the absence of such pits.

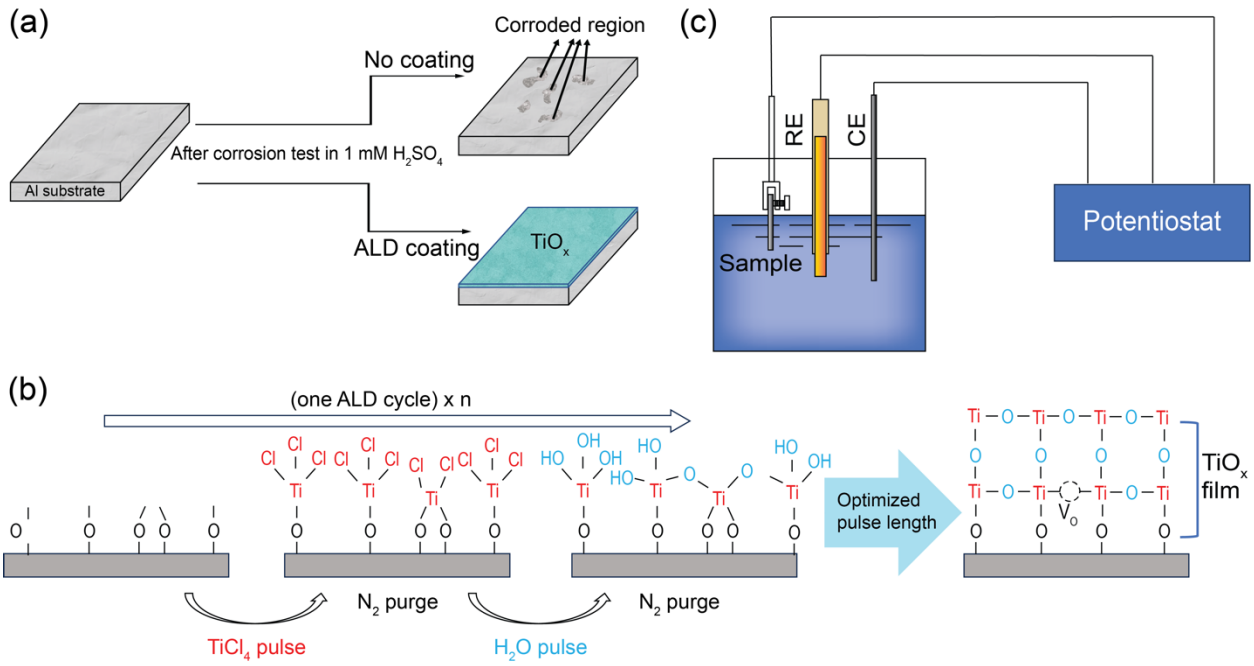


Figure 2.1 Schematic outline of the corrosion protection of Al substrate achieved by optimized ALD TiOx protection layers. (a) The substrates not coated (/coated) with the TiOx layers were found to be substantially affected (/not affected) on exposure to 1 mM sulfuric acid (pH ~ 3), (b) A single ALD cycle, coating a thickness of ~ 0.04 nm of TiOx, involves four successive steps (from left to right), i.e., (i) a TiCl4 pulse, (ii) a N2 gas purge, (iii) a H2O pulse, and (iv) a N2 gas purge. Varying pulse durations for the TiCl4 and the H2O yield a tunable x for the TiOx, while the purge time was used to minimize the pinholes in the ALD coating on the substrate. (c) The ALD coated samples, as the working electrode, were tested in standard electrochemical apparatus, with a Pt counter electrode (CE) and a Hg/HgSO4 reference electrode (RE), for quantitatively assessing potentiostatic corrosion over multiple days.

2.3 Experimental section

Aluminum sample preparation

Polished aluminum (Al) alloys, *e.g.,* Al 1100 (McMaster, Inc.) (99.0-99.95% Al, 0.05-0.20% Cu, 0.95% max Fe, 0.05% max Mg, 0.95% max Si, 0.1% max Zn, and residuals) were cut into 1 cm × 1 cm × 0.05 cm, samples. The alloy was specifically chosen for its excellent mechanical formability and superior corrosion resistance as shown by the comparison of Al-based materials in **Tables S2.1** and **S2.2** of the *Supporting Information*. The Al samples were polished by either

(i) mechanical polishing (MP), or (ii) electropolishing (EP). During the MP (Struers), the Al samples were first rough polished on Tech-Cloth (Allied High-Tech Products. Inc.) using a diamond suspension solution (DiaDuo-2 1 μm) with compression force of 25 N, with sample and stage rotation speeds of 200 rpm and 150 rpm, respectively. The samples were further polished on Final-P (Allied High-Tech Products. Inc.) using a silica suspension solution (OP-S 0.25 μm) with compression force of 10 N, and sample and stage rotation speeds of 150 rpm. The MP achieved a *rms* roughness of the order of 2 nm. Alternately, the EP was performed by immersing the Al samples into a 4:1 (phosphoric acid: sulfuric acid) mixture with applied voltage of 5 V, at 80 ^{o}C, and stirred (with a magnetic stirrer) at 200 rpm. After EP, the samples were removed from the mixture and cleaned in 28-30% ammonium hydroxide (NH_4OH) at room temperature for 30 sec. In this paper, EP Al samples were used as representative of a surface with controlled roughness. The samples were further ultrasonically cleaned, successively, in (i) acetone, (ii) isopropanol (IPA), and (iii) deionized (DI) water, for 5 min each with a nitrogen blow dry between each step. The Al substrates were treated with oxygen plasma (OP – Oxford Plasma lab 80 Plus RIE) to remove carbonaceous residues on the surface, which are known to hinder conformal ALD.

Atomic layer deposition (ALD) of TiO_x coating on Al alloys

The TiO_x films were deposited by ALD (Beneq TFS 200), using $TiCl_4$ and H_2O precursors. A typical ALD cycle consisted of the following four successive steps, *i.e.,* (i) a $TiCl_4$ pulse, (ii) a N_2 gas purge, (iii) a H_2O pulse, and (iv) a N_2 gas purge – as indicated in **Fig. 2.1(b)**. Typical pulse durations for the $TiCl_4$ and the H_2O were in the range of 100 ms – 150 ms and 25 ms – 50 ms, respectively. A higher (/lower) $TiCl_4$: H_2O pulse ratio would be expected to yield a smaller (/larger) value of the x in TiO_x. The purge times were varied in the range of 1 – 4 seconds, for tuning the extent of precursor reaction in the gas phase for ALD. The $TiCl_4$: H_2O pulse ratios were

then varied, with an aim of synthesizing films with the largest corrosion resistance. In this paper, the structural morphology, physical characteristics, and electrochemical attributes, obtained from three representative ALD recipes, *i.e.,* **R1** (100 ms $TiCl_4$ + 2 s purge + 50 ms H_2O + 2 s purge), **R2** (150 ms $TiCl_4$ + 2 s purge + 50 ms H_2O + 2s purge), and **R3** (150ms $TiCl_4$ + 2s purge + 25 ms H_2O + 2s purge) are reported. The ALD TiO_x deposition temperature was chosen to be 120 ^oC, as it was previously noted that ALD temperatures in excess of 150 ^oC induced crystallization of the TiO_x films, with enhanced possibility of corrosion in acidic conditions[38,39], as was also confirmed by preliminary experiments – see **Section Fig. S2.1** of the *Supporting Information*. A TiO_x deposition rate of ~ 0.02 nm – 0.04 nm $cycle^{-1}$ was recorded by ellipsometry (J.A. Woollam M-20000D) measurements using the spectral variation of the relevant optical constants, see Fig. **S2.10** of the *Supporting Information.*

Surface Characterization

The surface film morphology and elemental composition, *e.g.,* the Al content, the TiO_x stoichiometry, were characterized by scanning electron microscopy (SEM: FEI Apreo) imaging coupled with EDS (energy dispersive X-ray spectroscopy), with an electron beam energy of 10 keV. Further confirmation of the Ti : O ratios were obtained by Auger electron spectroscopy (AES: microCMA), with an electron beam energy of 3 keV. Tapping mode atomic force microscopy (AFM: Park NX20) with the AFM tip NSC15/Al BS (Park system, < 8nm) was used to determine the roughness of the samples, over several 10 μm × 10 μm regions before and after ALD. Assuming the conformality of the ALD, the R_z (the measure of the difference between the highest peak and the lowest valley in a thin film) may be taken as related to the presence of a pinhole in the film. The reported R_z was obtained through extensive averaging over several line scans over the sample area.

Corrosion testing

The ALD film coated samples were tested for corrosion resistance in sulfuric acid solutions, typically with a molarity of 1 mM (with a pH of 3) under a constant voltage of 2.4 V (*vs*. NHE) – corresponding to typical test conditions employed for commercial water electrolyzers[4-6]. The schematic of the relevant experimental apparatus was shown in **Fig. 2.1(c),** with the test sample as the working electrode (WE). The mercury sulfate electrode (MSE) was used as the reference electrode (RE) while a Pt wire served as the counter electrode (CE). The potential difference, corresponding to the testing voltage was applied between the test sample and the RE. In the related potentiostatic (PS) testing, ALD coated samples were taped, with the edges protected, and with a sampling area of 0.785 cm^2 (shown in **Fig. S2.3** of the *Supporting Information*) were kept in solution for up to 50 hours. The samples were immersed in the solution for 5 min prior to the commencement of the testing to determine the open circuit potential. The monitoring of the current density, relevant to the sample, during the potentiostatic testing was performed (Gamry 1010B). The Tafel tests were done both before and after the potentiostatic testing with voltage scans from -1.8 V to 1.8 V (-1.166 V to 2.434 V) *vs.* MSE (NHE) in 1 mM H_2SO_4).

Inductively coupled plasma mass spectrometry (ICP-MS)

The loss of Ti (in the form of Ti^{4+} ions) from the coating as well as Al (in the form of Al^{3+} ions) from the substrate was monitored at the 0.1 ppb and 0.01 ppb (parts per billion) level by ICP-MS (iCAP RQ) with a detection limit of 0.3 ng L^{-1} for Al and 0.8 ng L^{-1} for Ti^{40}. Typically, ~ 2 ml samples of the acid solutions were removed and tested, occasionally during the potentiostatic testing. The Al^{3+} and Ti^{4+} concentrations were carefully calibrated over a range of 0.01 ppb to 1000 ppb in 1% trace metal nitric acid (*blank*), for ensuring the fidelity of the test results. The

blank (1% trace metal nitric acid) was forced to zero for reference. And all values equal or smaller than zero were treated as zero loss in this study.

2.4 Structural and elemental analysis through transmission electron microscopy (TEM)

To improve the corrosion resistance of Al substrates, three different TiO_x thin films were deposited by thermal ALD with different ALD recipes (**R1**: 100 ms $TiCl_4$ + 2 s purge + 50 ms H_2O + 2 s purge, **R2**: 150 ms $TiCl_4$ + 2 s purge + 50 ms H_2O + 2 s purge, and **R3**: 150 ms $TiCl_4$ + 2 s purge + 25 ms H_2O + 2 s purge) – also see *Section 4.2*) . The morphologies of the ALD layers on the O_2 plasma cleaned Al substrates was examined by transmission electron microscopy (TEM) and is shown in **Fig. 2.2**. The ALD TiO_x showed an expected film thickness (from a deposition rate of ~ 0.02 – 0.04 nm cycle^{-1}) of ~ 60 (± 2) nm for all three ALD recipes. The TEM of the TiO_x layers is consistent with an amorphous structure while EDS maps indicate a uniform composition of the TiO_x films. **Fig. 2.2 (d)** shows the scanning TEM energy dispersive spectroscopy (STEM-EDS) scans of the **R2** ALD TiO_x. It was noted that a 5 nm Al_xO_y film was formed due to oxygen plasma (OP) treatment of the substrate and is visible in both the TEM images and the EDS maps. Such a layer suggests a methodology for substrate cleaning, aimed at improving corrosion resistance. While the elemental distribution observed in EDS suggests uniform elemental distribution of the Ti and O in the ALD TiO_x layer, further analysis would be needed to determine the specific stoichiometry.

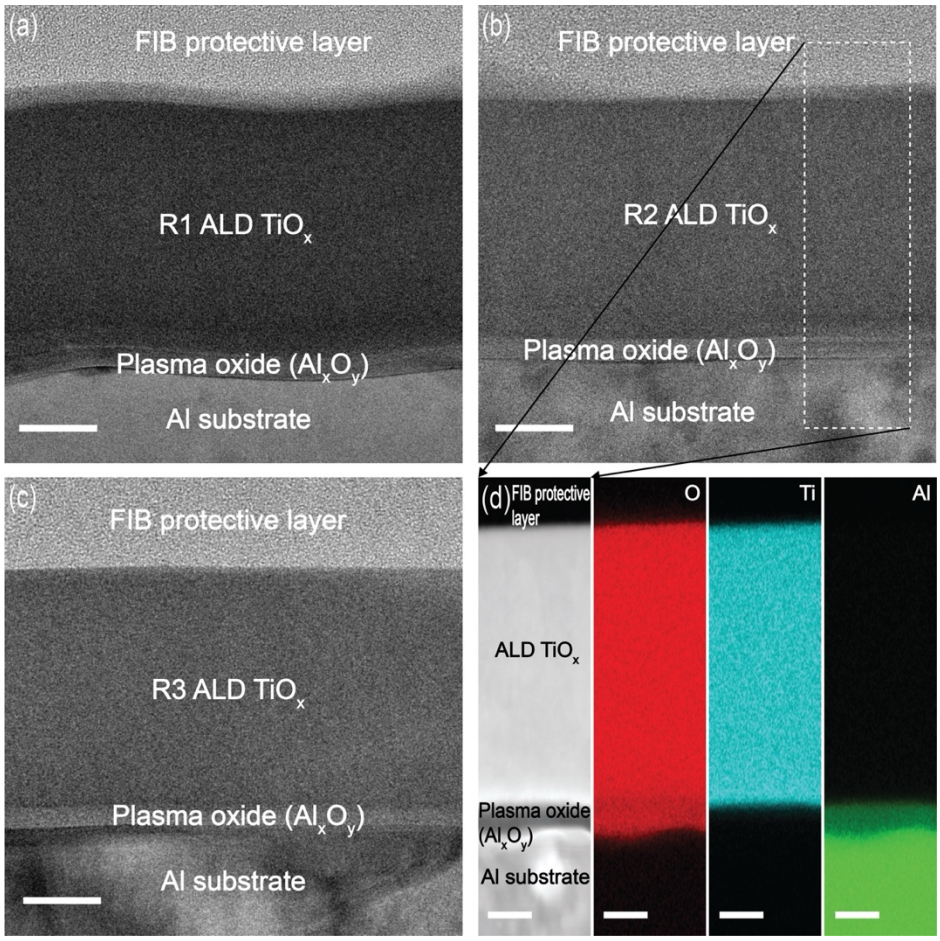


Figure 2.2 TEM Imaging of 60 nm ALD TiO_x film on EP Al(1100) substrate after O_2 plasma clean. TEM image of **(a) R1** ALD TiO_x coating, **(b) R2** ALD TiO_x coating, and **(c) R3** ALD TiO_x coating on the Al substrate (the scale bar is 20 nm). An interfacial aluminum oxide, arising from an oxygen plasma clean, was observed at the substrate – coating interface. **(d)** STEM EDS mapping of **R2** ALD TiO_x coating on the Al substrate (the scale bar is 10 nm).

2.5 Determining TiO_x stoichiometry by correlating energy dispersive spectroscopy (EDS) and Auger electron spectroscopy (AES)

The ALD precursor pulse length was optimized to deposit a non-stoichiometric titanium oxide with an O : Ti ratio deviating from the 2:1 ratio in TiO_2 because non-stoichiometric films were reported to have superior corrosion resistance[35]. The O : Ti ratios for the three representative ALD recipes: **R1** (100 ms $TiCl_4$ + 2 s purge + 50 ms H_2O + 2 s purge)**, R2** (150 ms $TiCl_4$ + 2 s

purge + 50 ms H_2O + 2 s purge), and **R3** (150 ms $TiCl_4$ + 2 s purge + 25 ms H_2O + 2 s purge)**,** were characterized through both EDS (/SEM) as well as AES: **Fig. 2.3,** also see **Fig. S2.2** of the *Supporting Information*.

The quantitative determination of the elemental concentration, *i.e.,* Ti, Al, and O, in AES[41,42] was done by comparing the relative peak-to-peak intensities of the respective differentiated Auger peaks, taking into account the element-specific sensitivity factors[41]. In EDS, the ratio of the respective elemental weight concentrations (*c*), *e.g.,* C_{Ti}/C_O, is proportional to the peak intensities (*I*) of the identified[43] elements, through

$$\frac{C_{Ti}}{C_O} = k_{Ti-O}\frac{I_{Ti}}{I_O} \qquad (2.1)$$

where k_{Ti-O} is a factor determined by comparison with a reference/standard (*std*) sample:

$$k_{Ti-O} = \frac{C_{Ti}^{std}}{C_O^{std}}\frac{I_O^{std}}{I_{Ti}^{std}})^{44} \qquad (2.2)$$

Subsequently, the weight concentration was converted to atomic concentration. The characteristic energy peak of each element was indicated in the AES and EDS spectrum. Three measurements were taken at distinct sample locations at the center and edge areas, for reporting a mean value as well as related random and systematic errors. Both the AES and EDS indicated that the O : Ti ratio was successfully tuned via adjusting the precursor pulse length from recipe **R1** to **R2** to **R3**. It was noted that there was a significant difference in the measured Ti : O ratios between the EDS and AES measurements, *e.g.,* in the case **R2,** the ratio was ~ 2.9 from EDS, and ~ 1.35 from AES. The difference in the measured stoichiometry in these two cases is due to the different interaction volume of the two different characterization methods. While the sampling area related to AES [45] has been indicated to be a few square microns with a probe depth ~ 2-3 nm, the corresponding value for EDS [43] is much larger at ~ hundreds of square microns with a signal from up to ~1 μm of depth into the sample and may also include contributions from Al substrate oxidation.

Consequently, the AES, probing the top few nm (~ 2-3 nm) of the film[46,47], was considered as more representative of the TiO_x film stoichiometry. It was observed that the measured O : Ti ratio was correlated with the dosed H_2O : $TiCl_4$ precursor pulse length ratio, *i.e.,* recipes **1**, **2**, and **3** with H_2O : $TiCl_4$ precursor pulse length ratios of 1:2, 1:3, and 1:6, yielded $TiO_{1.4}$, $TiO_{1.35}$, and $TiO_{1.3}$, respectively as measured through AES.

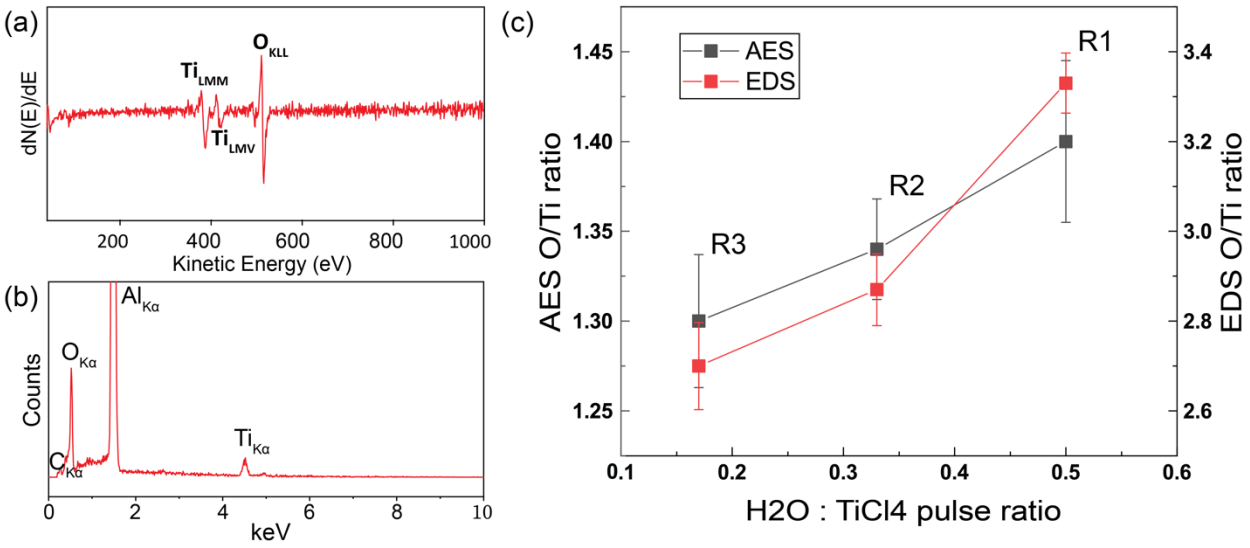


Figure 2.3 Auger Electron Spectroscopy (AES) and SEM Energy dispersive X-ray Spectroscopy (EDS) characterization on three representative recipes of ALD TiO_x. The observed **(a)** AES, and **(b)** EDS spectra, for TiOx synthesized through ALD recipe **R2** (150 ms $TiCl_4$ + 2 s purge + 50 ms H_2O + 2 s purge). **(c)** The O : Ti ratio for the three recipes, **R1** (100 ms $TiCl_4$ + 2 s purge + 50 ms H_2O + 2 s purge), **R2** (150 ms $TiCl_4$ + 2 s purge + 50 ms H_2O + 2 s purge), and **R3** (150 ms $TiCl_4$ + 2 s purge + 25 ms H_2O + 2 s purge) with different $TiCl_4$: H_2O precursor pulse length, as measured by AES (*left*) and EDS (*right*) with error determined by measurement at three different locations on sample.

2.6 Atomic force microscopy (AFM) study of the film topography

The surface roughness and associated features were characterized to determine quantitatively the role of the ALD in depositing conformal coatings - also see *Section 2.3*. The characteristic surface topography resulting from ALD TiO_x films corresponding to recipes **R1**, **R2**, and **R3** on electropolished Al substrates (of root mean square height, S_q ~ 7.0 ± 0.5 nm) is shown

in **Fig. 2.4**. For better understanding of the influence of surface roughness and comparison, the ALD of the TiO_x was also performed on smooth (S_q ~ 0.30 ± 0.03 nm) silicon (Si) substrates. Each sample was characterized, for consistency of the measured values, at several different locations. It was observed that a significant roughening of the surface morphology was obtained with an increased $TiCl_4$: H_2O precursor pulse length ratio.

With recipe **R1** (100 ms $TiCl_4$ and 50ms H_2O), an *Sq* of ~ 7.1 ± 0.5 nm (/0.33 ± 0.04 nm) was measured on EP Al 1100 (/Si): **Fig. 2.4 (a)** and **2.4 (d)**, similar to what was previously reported[48,49]. With a higher $TiCl_4$ precursor pulse time (150 ms $TiCl_4$), *e.g.,* as in the recipe **R2**, an *Sq* ~ 7.7 ± 0.6 nm (/0.40 ± 0.03 nm) was noted on the EP Al 1100 (/Si): **Fig. 2.4 (b)** and **2.4 (e)**. Alternately, a further decreased H_2O pulse length (~ 25 ms), as in recipe **R3** contributed to a substantial increase in the S_q to ~ 12.1 ± 1.0 nm (/0.56 ± 0.06 nm) on the EP Al 1100 (/Si): **Fig. 2.4 (c)** and **2.4 (f)**. The line trace measurements were applied on random positions and avoided the pitting hole defects (black features in **Fig. 2.4 (a)**, **2.4 (b)**, and **2.4 (c)**) caused by electropolishing to study the ALD TiO_x topography on EP Al 1100. A higher mean roughness depth *(R_z)* (30 nm on EP Al 1100 and 3.0 nm on Si) was also observed in the latter case as shown in the line trace in **Fig. 2.4 (c) and (f)**, implying that small water pulse lengths may result in unsaturated precursor coverage leads to oxide thickness heterogeneity with a greater possibility of pinhole formation.

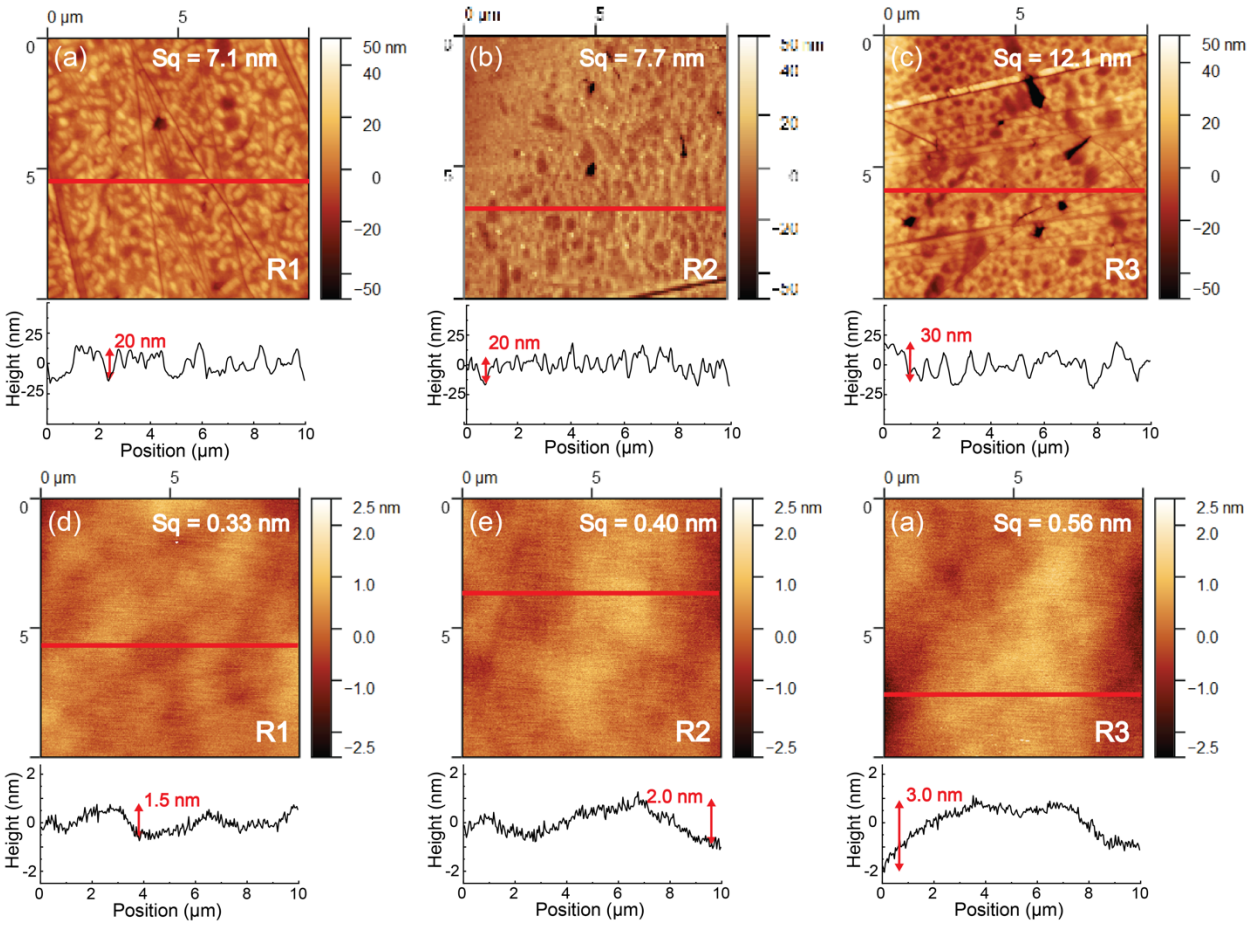


Figure 2.4 Atomic force microscopy (AFM) characterization of the as-deposited ALD TiO_x layers (a) R1 (100 ms $TiCl_4$ + 2 s purge + 50 ms H_2O + 2 s purge), (b) R2 (150 ms $TiCl_4$ + 2 s purge + 50 ms H_2O + 2 s purge), (c) R3 (150 ms $TiCl_4$ + 2 s purge + 25 ms H_2O + 2 s purge) on electropolished (EP) Al 1100, **(d) R1**, **(e) R2 (f) R3** on Si(001). The root mean surface roughness (S_q) is indicated on the images. The topography measured from the scans (*red lines*) is shown beneath the images with the mean roughness depth (indicated in *red*). The layer roughness also reflects the intrinsic roughness, *i.e.,* the bare EP Al (/Si) had a root mean surface roughness (S_q) ~ 7 ± 0.5 nm (/0.3 ± 0.03 nm).

2.7 SEM/TEM and ICP-MS based analysis of the extent of corrosion of Al substrates

The corrosion resistance of the ALD TiO_x coating layers, with respect to the representative recipes **R1**, **R2**, **R3** - considering both the extent of protection of the underlying substrate as well as the layer durability, were investigated – see *Section 2.3*. The TiO_x/Al samples were immersed in 1 mM H_2SO_4 with a constant applied voltage of 2.4 V (*vs.* NHE) to mimic the working condition

of electrolyzers, over various time scales. This was done by three electrode experiments, as discussed in *Section 2.3* and as represented in **Fig. 2.1(c),** also see **Fig. S2.3** of the *Supporting Information* for details on the sample testing configuration.

The corrosion resistance of the surfaces was first examined by SEM imaging as shown for the tested samples before and after the potentiostatic test: **Fig 2.5**. It was apparent from the comparison of the SEM images with and without the ALD TiO_x coating in **Fig. 2.5 (b)** and **(c),** respectively, that the coating was successful in substantially preventing corrosion. Significant pitting was observed on the Al substrate in the absence of the coating, while the coated surface was relatively unchanged.

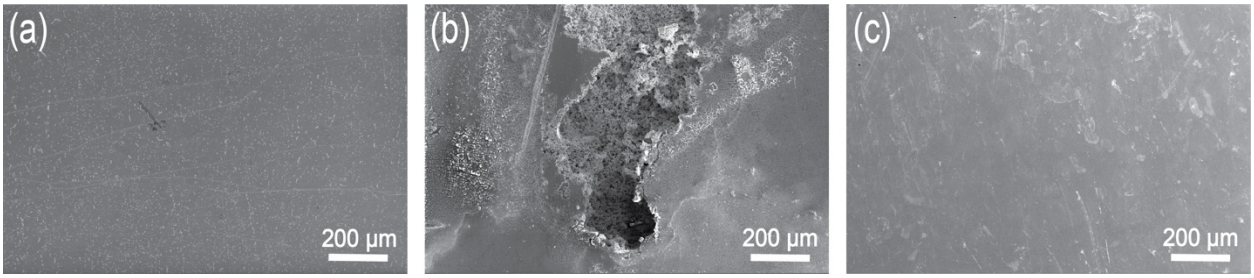


Figure 2.5 SEM images related to the corrosion testing of Al with and without ALD TiO_x. **(a)** Uncoated electropolished (EP) Al substrate prior to corrosion testing. After immersion in 1 mM Sulfuric acid with 2.4 V (*vs.* NHE) of applied voltage at room temperature, the **(b)** surface of the EP Al without TiO_x coating is significantly worse compared to **(c)** EP Al with 60 nm of TiO_x deposited by recipe **R2.**

While the beneficial results of the TiO_x coating in **Fig. 2.5(c)** are demonstrated above for recipe **R2,** similar improvements in corrosion resistance were obtained for the other recipes, **R1** and **R3.** Consequently, there is a necessity for more quantitative determination of the corrosion protection due to the coating layers. For analyzing the extent of corrosion of the Al substrate due to the TiO_x coating (using recipes **R1**, **R2**, and **R3**), the Al^{3+} and Ti^{4+} concentrations in the acid electrolyte were measured by ICP-MS (with a resolution of parts per billion: ppb, typical to the

detection limits of the technique[40]) over a duration of 50 hr – see *Section 2.3* for related experimental details. The ion concentrations were monitored at regular intervals during testing. The results shown in **Fig. 2.6 (a)** indicate that while a large amount of Al^{3+} (~8000 ppb) was detected in the absence of the ALD TiO_x layer, that there was a drastic decrease to < 0.1 ppb level through the use of the ALD coating, specifically through the use of recipe **R2: Fig. 2.6 (a)**. It was observed that recipe **R2** also yielded the lowest Ti^{4+}, *i.e.,* at ~ 0.14 ppb: **Fig. 2.6 (b)**. In comparison, recipes **R1** and **R3** yielded relatively less protection of the Al substrate by an order of magnitude, while the coatings themselves were all durable with respect to the loss of the Ti, at the level of 0.2 ppb $\pm$0.1 ppb. The details related to the ICP-MS calibration are illustrated in **Table S2.3** as well as additional details in **Figs. S2.4 – S2.6** of the *Supporting Information*.

Through a study of the concentration variation with time, it was seen that the loss of the Ti was fairly consistent and linear with time, with a relative saturation observed only for recipe **R2.** A measure of the corrosion rate (*CR*) of the Al substrate and the TiO_x coating may be obtained through the relation:

$$CR = \frac{[C_x]V_{sol} \cdot 24\ h \cdot 365\ d}{\rho_x} \qquad (2.3)$$

Here, $[C_x]$is the concentration of the species, *i.e.,* Al^{3+}/Ti^{4+} ions detected through the ICP-MS, V_{sol} is the sampling volume, and ρ_x is the density of the Al/TiO_x. It was estimated that the TiO_x synthesized through recipe **R2** had a corrosion rate related to the Ti loss of the order of 6 nm $year^{-1}$.

While there was negligible loss of the Al^{3+} using recipe **R2**, the rate of loss of Al^{3+} was again constant for EP Al coated with recipes **R1** and **R3**. However, the Al^{3+} was detected after 10 hours in the potentiostatic test for the EP Al substrate coated with recipe **R1**, while the Al^{3+} could

be detected at the beginning of the test for EP Al coated with recipe **R3**. This phenomenon indicated that the corrosion of the Al was ascribed to pinholes in the coating. The ALD TiO_x coated with recipe **R1** is more susceptible to corrosion to form pinholes during the potentiostatic test, whereas the ALD TiO_x coated with recipe **R3** forms pinholes at the beginning of the potentiostatic test at the regions with thinner oxide. This result is consistent with the AFM results on both EP Al 1100 and Si indicated previously. It was concluded that the robustness of the coating layer as well as the protection of underlying Al substrate are ensured to the maximum extent possible, within the resolution of measurement, using a specific ALD recipe: **R2**. While inclusions in the Al substrate may induce statistical variations, tests in our study were typically carried out over larger area (~ 1 cm^2) where the related influence of inclusions could be minimized or averaged out. We did confirm, through many tests over the period of several months, that the obtained results were robust and reproducible.

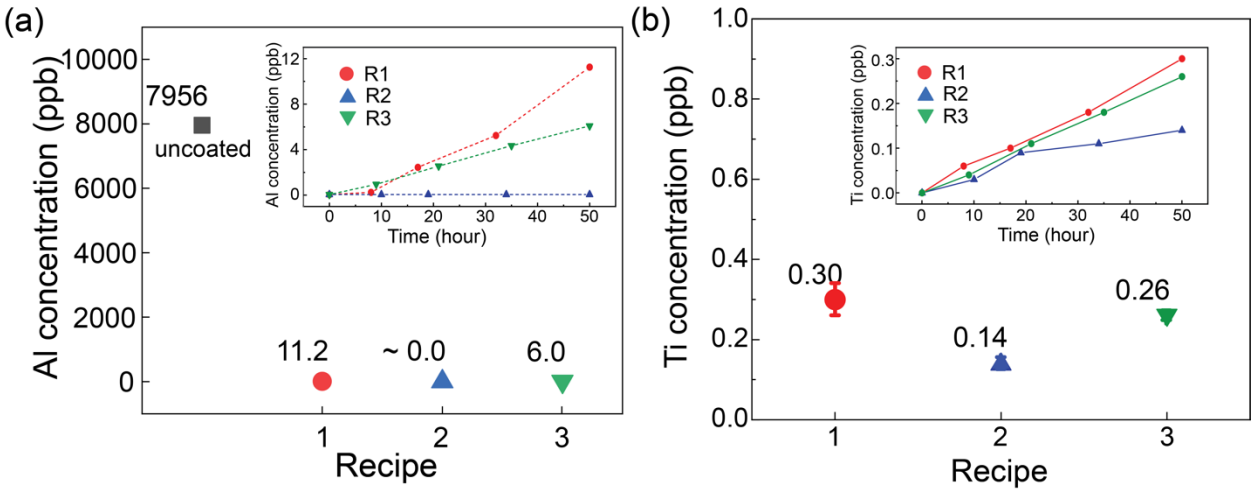


Figure 2.6 The results from ICP-MS (inductively coupled plasma - mass spectroscopy) **of the corrosion related elemental loss of Al (as Al^{3+}) and Ti (as Ti^{4+}) from three representative ALD recipes (R1, R2, and R3) for 60 nm TiO_x coating layers on EP Al 1100.** The samples were immersed in 1 mM H_2SO_4 at 25 °C and held at 2.4V (*vs.* NHE) for 50 hrs. **(a)** The coatings were seen to be effective in preventing Al substrate corrosion by orders of magnitude, **(b)** Recipe **R2** was observed to be the most effective, in terms of reducing the Ti^{4+} concentrations to ~ 0.14 ppb, respectively. The variation of Al^{3+} and Ti^{4+} dissolution with time is shown in the *insets*.

From the ICP-MS results, it was noticed that the corrosion of the Al substrate is higher for the ALD TiO_x layer coated with recipe **R1** and **R3** by orders of magnitude. To better understand the corrosion mechanism of the ALD TiO_x coated EP Al 1100, the pinholes in the ALD TiO_x and corroded Al substrate were investigated through TEM, as in **Fig. 2.7**. A large corrosion pit inside the Al substrate was observed and is consistent with the high Al^{3+} concentration detected in the solution after potentiostatic testing for EP Al 1100 coated with **R1** and **R3** ALD TiO_x. The pinhole location is indicated by the deposition of the FIB protective layer into the corrosion pit beneath the ALD TiO_x layer. The size of the pinhole is tiny in comparison with the corrosion pit, which indicated that the Al substrate is much more susceptible to corrosion than the ALD TiO_x. Enormous corrosion pits will be generated once a small pinhole is formed in the ALD TiO_x. The nucleation of the corrosion could be initiated at inclusions after the dissolution of the ALD TiO_x or at thin oxide sites with pinholes. Therefore, both generating a pinhole free and corrosion resistant ALD TiO_x are important to eliminate the corrosion of the Al substrate. This is demonstrated by the optimized oxygen vacancy rich ALD TiO_x deposited by recipe **R2** that is pinhole free and has low dissolution rate in 1 mM H_2SO_4 at 2.4 V (*vs*. NHE).

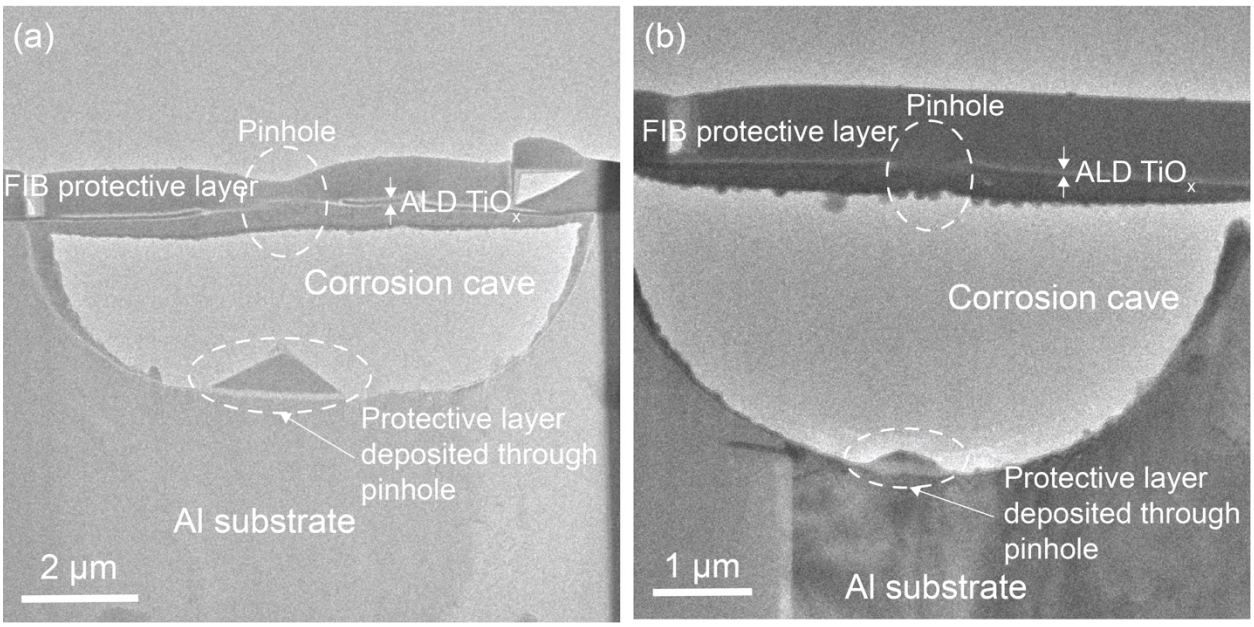


Figure 2.7 TEM images of pinholes on ALD TiO_x and corroded Al after potentiostatic test, Al substrate corroded **(a)** after ALD TiO_x deposited with recipe **R1** dissolved into 1mM H_2SO_4 and formed pinholes or **(b)** through pinholes formed during ALD TiO_x deposited with recipe **R3**.

2.8 Electrochemical analysis of the ALD TiO_x coating on Al substrates

The resistance to corrosion may also be elucidated through electrical voltage – current variations, as obtained through polarization plots[50]. During the potentiostatic tests for ALD TiO_x coated Al: **Fig. 2.8 (a),** it was seen that there was a gradual increase in the measured current through the sample immersed in the test acid solution, implying initial localized corrosion of the ALD TiO_x which serves as pitting initiation sites[51]. However, the rate of increase in the current density diminishes with time, leading to a steady state current density (SSCD). Further details related to the potentiostatic testing, comparing uncoated and ALD coated Al substrates are indicated in **Fig. S2.7** of the *Supporting Information*. Aiming towards an understanding of the electrochemical mechanisms of the corrosion process of the coating and the substrate, a more detailed investigation through the use of polarization curves[52] for the ALD TiO_x coated substrates, with associated definition for the corrosion potential (E_{corr}) and corrosion current density (J_{corr}) is indicated in **Fig.**

2.8 (b). A comparison of the polarization curves for the coated *vs.* uncoated Al substrates is shown in **Fig. 2.8 (c)**.

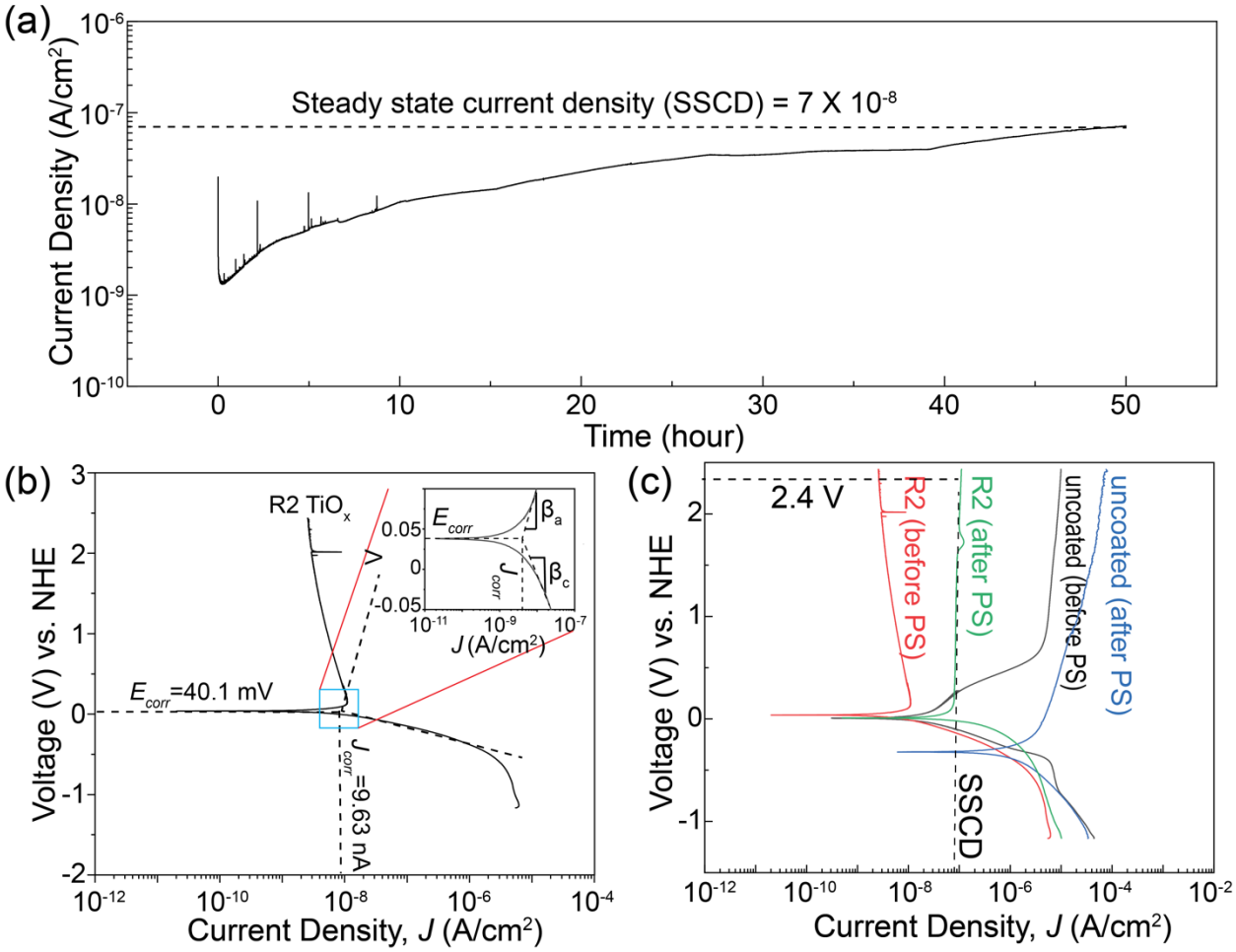


Figure 2.8 Electrical current variation observed in corrosion testing. (a) The susceptibility to corrosion was monitored over time by potentiostatic (PS) tests, where the electrical current through TiO_x coated Al substrates immersed in test acid solutions was monitored at a fixed voltage of 2.4 V (*vs.* NHE). The current was normalized to a constant and fixed area of 0.785 cm^2. **(b)** polarization curves indicate the definition of the corrosion potential (E_{corr}) and the corrosion current density (J_{corr}) for ALD TiO_x coated Al substrates - in 1mM H_2SO_4., using recipe **R2**, **(c)** polarization curves of Al substrate with and without ALD TiO_x tested before and after potentiostatic test indicated the E_{corr} and J_{corr} are substantially increased/reduced due to the ALD coating.

The E_{corr} and J_{corr} was determined by the intersection of the anodic slope (β_a) and the cathodic slope (β_c) of the polarization curves, following standard precepts [10], and as defined in **Fig. 2.7(b).** The resistance to corrosion was indicated by the polarization resistance:

$$R_p = \frac{\beta_a \beta_c}{2.303 \cdot (\beta_a + \beta_c)} \left(\frac{1}{J_{corr}} \right) \qquad (2.4)$$

The associated values are shown in Table 2.1.

Table 2.1 A comparison of the Tafel fit parameters of bare EP Al and ALD TiO_x coated EP Al substrates (using recipe **R2**), obtained from the experimental polarization curves, when the samples were placed in 1 mM H_2SO_4.

Sample	I_{corr} (nA cm^{-2})	E_{corr} (mV)	R_p (Ω cm^2)
Uncoated (before PS)	26.0	10.0	1.51×10^6
Uncoated (after PS)	6254.8	-322.0	6.03×10^4
R2 coated (before PS)	9.6	40.1	6.29×10^6
R2 coated (after PS)	73.2	9.0	1.18×10^6

It was noted, from **Table 2.1** that a higher E_{corr} (~ 40 mV) accompanied by a smaller J_{corr} (~ 9.6 nA cm^{-2}) was observed for the TiO_x coated Al substrate in comparison to when the coating was not used, *i.e.,* with an E_{corr} ~ 10 mV, and J_{corr} ~ 26 nA cm^{-2} from the Tafel test in 1 mM H_2SO_4 before the potentiostatic test was applied to the specimen. An increased robustness in terms of the resistance to corrosion is evident as manifested through a four-fold increased polarization resistance (R_p) for the coated substrate. Subsequently, when the uncoated and coated samples were subject to potentiostatic testing, the magnitude of the increase (/decrease) in the J_{corr} (/E_{corr} and R_p)

in the Tafel analysis was smaller in the TiO_x coated sample. The current density at 2.4 V (*vs.* NHE) in the polarization curves is in accordance with the SSCD at 50 hours, observed in the potentiostatic test. Therefore, lower SSCD can be represented for higher resistance (lower activity) to the corrosion to some extent. The decrease in the E_{corr} for the uncoated samples by ~ 332 mV is an order of magnitude larger than for the coated samples, of ~ 31 mV. The smaller E_{corr} change could be interpreted as an indication of the higher resistance to corrosion due to the TiO_x coating. Furthermore, higher positive E_{corr} results in lower current density at high positive voltage (2.4V *vs*. NHE) also indicated better corrosion resistance at high positive voltage. Further details related to the polarization curves, comparing uncoated and ALD coated Al substrates, as well as a reference Ti electrode are indicated in **Table S2.4** and **Fig. S2.8,** as well as in **Fig. S2.9** of the *Supporting Information*.

2.9 Conclusions

The present study demonstrates that optimized ALD TiO_x coatings obtained by tuning the stoichiometry as well as by the absence of pinholes could be deployed for reducing the corrosion of Al substrates by orders of magnitude. Several variables related to the ALD, *i.e.,* precursor pulse lengths, purge times, deposition temperature, *etc.* were found to be of significance. For corrosion resistant films, both the quantity as well as the ratio of the dosed $TiCl_4$ and the H_2O precursors were seen to be crucial. A correlation was seen between the oxidation level (/oxygen vacancy concentration) of the deposited film with respect to diminished leaching of the Al from the underlying substrate and serves as an indicator for high quality corrosion resistant films.

The ALD coatings were tested on Al samples immersed in conditions relevant to industrial electrolyzer application, *e.g.,* low pH and large overpotentials. Careful monitoring of the resultant

loss of Al^{3+} by ICP-MS yielded a loss of at the 0.1 ppb level[40], within the instrumental resolution, for a specific ALD coating recipe: 150 ms $TiCl_4$ + 2 s purge + 50 ms H_2O + 2 s purge. While TiO_x films with carefully controlled oxygen deficiency could be used for improved corrosion resistance, deviations in x of $\pm$ 0.05 from the optimal composition in ALD TiO_x, as obtained by Auger spectroscopy, were observed to have much increased susceptibility to corrosion. A corrosion rate of the order of 6 nm $year^{-1}$ was estimated for the optimized TiO_x coatings.

2.10 Supporting Information

Supplemental Table 2.1 Detailed information of different Al substrates Al 1100 is the best replacement material for titanium anode pack of electrolyzers and fuel cells due to its low cost, corrosion resistant and easy to form properties.

Material	Al 1100 (McMaster)	Al 99.999% (Goodfellow)	Al 7075 (McMaster)
Al purity	99%	99.999%	87.32% - 90.02%
composition	Al, Cu, Fe, Mg, Si, Zn, etc.	Al, Si, Cu, Fe, Mg	Al, Zn, Mg, Cu, Fe, Si, Mn, Cr, Ti, etc.
Hardness (Brinell)	23	15	150
Pros	Easy to form, corrosion resist, cost efficient	High purity, double side polished	High hardness, corrosion resist, cost efficient
Cons	Surfaces need extra polish process	Expensive, soft for compression	Surface need extra polish process, hard for manufacturing

Supplemental Table 2.2 ICP-MS results of 50 nm R2 (150 ms $TiCl_4$ + 2 s purge + 50 ms H_2O + 2 s purge) ALD TiO_x coated on different Al substrate after potentiostatic test in 1 mM H_2SO_4 at 2.4 V vs. NHE, The optimized oxygen vacancy rich TiO_x deposited with recipe R2 (150 ms $TiCl_4$ + 2 s purge + 50 ms H_2O + 2 s purge) showed the best corrosion resistance on Al 1100 substrate with no Al substrate corroded, compared to other two different Al substrates, *e.g.*, Al 99.999% and Al 7075. The ALD TiO_x on Al 1100 is the most robust film at the mimic condition for electrolyzers manifested the lowest dissolution rate.

Al substrate	27 Al KED (ppb)	48 Ti KED (ppb)	TiO_2 dissolution rate (nm $year^{-1}$)	TiO_2 dissolution rate (ug cm^{-2} $year^{-1}$)
Al 1100	0.0 (50hr)	0.14 (50hr)	5.91	2.50
Al 99.999%	30.0 (50hr)	0.76 (50hr)	32.08	13.57
Al 7075	3.8 (50hr)	0.24 (50hr)	10.13	4.29

Supplemental Table 2.3 Reported test metal concentration in the 67-70% trace metal grade nitric acid[53]. 1% trace metal nitric acid - obtained through dilution from the obtained 67-70% trace metal grade nitric acid - was used as a *blank* for the background calibration in ICP-MS. The *blank* solution was used as the reference for Al concentration (< 0.014 ppb) and Ti concentration (< 0.007 ppb).

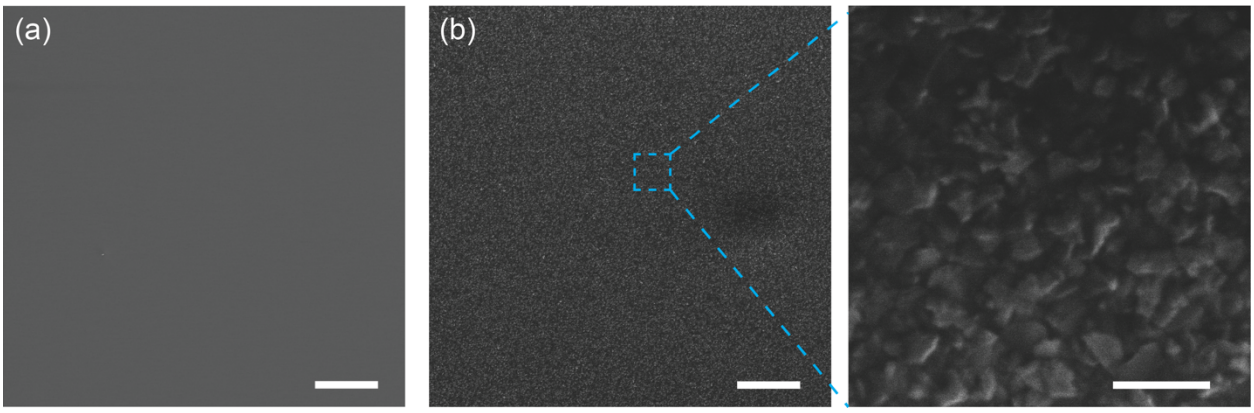
Metal	Units	Specifications	Test Value
Aluminum (Al)	ppb	<= 1	< 1
Titanium (Ti)	ppb	<= 0.5	< 0.5

Supplemental Table 2.4 Tafel fit parameters of uncoated and ALD TiO_x coated EP Al 1100, ALD TiO_x coated EP Al 1100 shows 2 – 4 times higher polarization resistance compared to the uncoated Al substrate indicated improved corrosion resistance. The ALD TiO_x deposited with R2 recipe displayed the highest positive E_{corr} corresponding to its best corrosion resistance property under electrolyzers working condition (2.4V vs. NHE in 1 mM sulfuric acid).

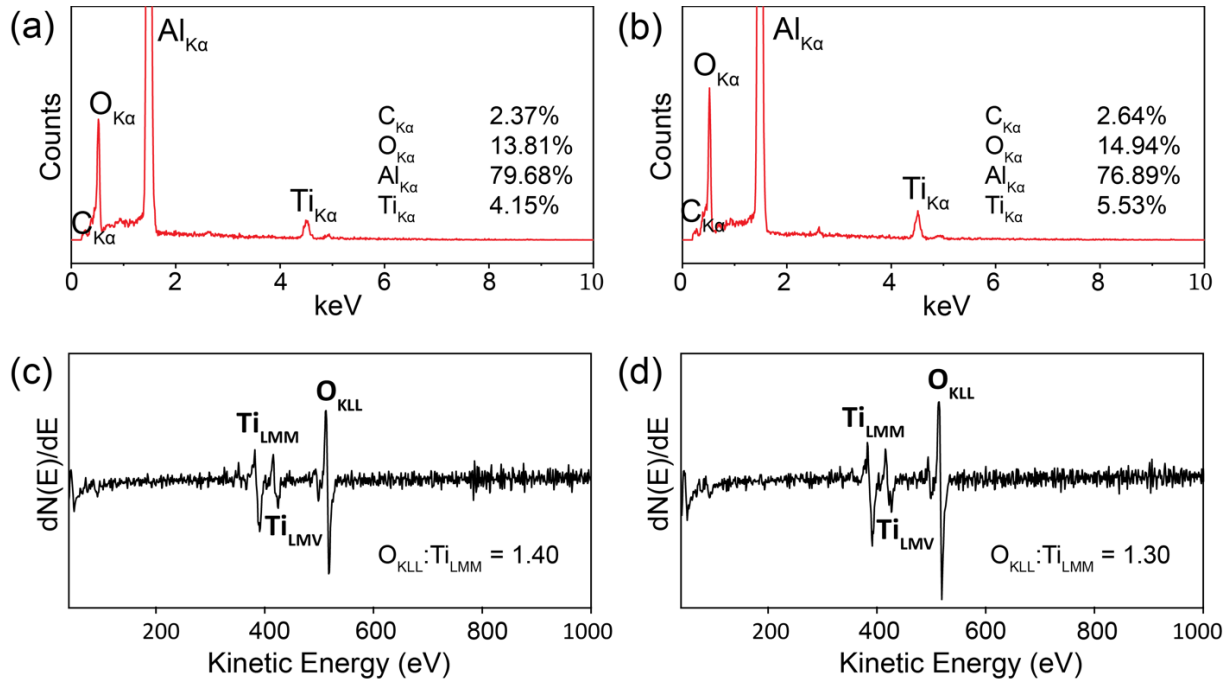
Sample	I_{corr} (nA cm^{-2})	E_{corr} (mV)	R_p ($\Omega \cdot cm^2$)
Uncoated	26.0	10.0	1.51×10^6
R1 recipe coated	18.0	-8.4	2.76×10^6
R2 recipe coated	9.6	40.1	6.29×10^6
R3 recipe coated	18.6	-14.5	4.25×10^6

Supplemental Table 2.5 ICP-MS results of repeat test for 50 nm ALD TiO_x coated with different recipe (R1: 100 ms $TiCl_4$ + 2 s purge + 50 ms H_2O + 2 s purge, R2: 150 ms $TiCl_4$ + 2 s purge + 50 ms H_2O + 2 s purge, and R3: 150 ms $TiCl_4$ + 2 s purge + 25 ms H_2O + 2 s purge) on EP Al substrate after potentiostatic test in 1 mM H_2SO_4 at 2.4 V vs. NHE, ~0 ppb (<0.1 ppb) Al detected from ICP-MS was able to be repeated multiple times. Same trend of Al and Ti ion concentration was identified for the three different ALD recipes proved that the corrosion resistance of the optimization for O : Ti stoichiometry with ALD pulse length is repeatable from ALD run to ALD run and sample to sample.

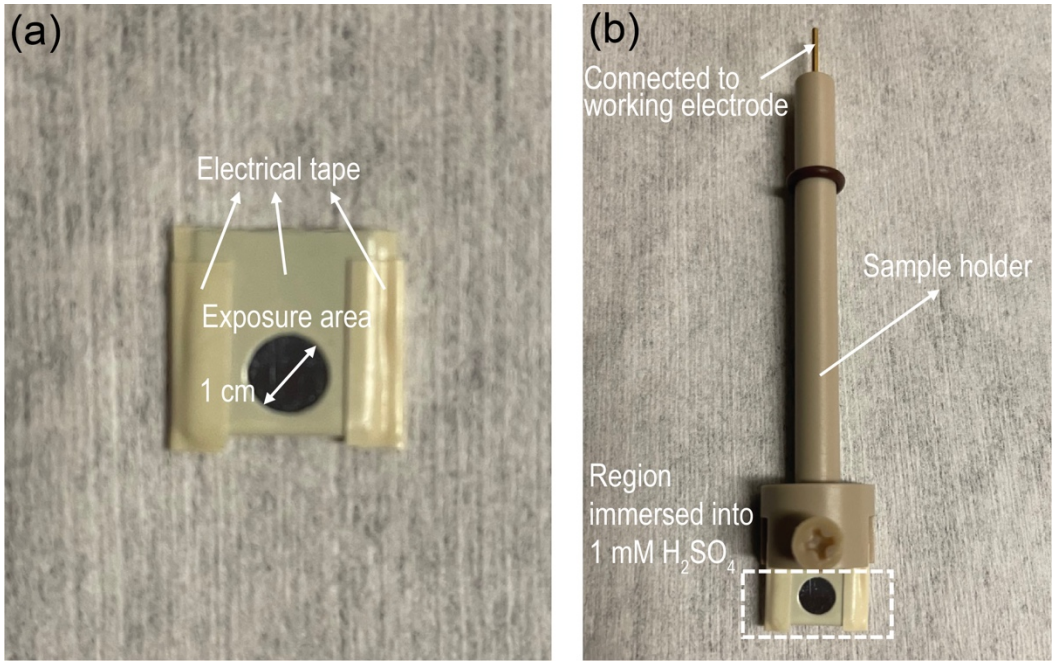
Recipe	Test 1		Test 2		Test 3	
	Al (ppb)	Ti (ppb)	Al (ppb)	Ti (ppb)	Al (ppb)	Ti (ppb)
R1 recipe coated	11.2	0.30	11.5	0.38	9.6	0.34
R2 recipe coated	0.0	0.14	0.0	0.12	0.0	0.15
R3 recipe coated	6.0	0.26	8.4	0.24	5.0	0.26



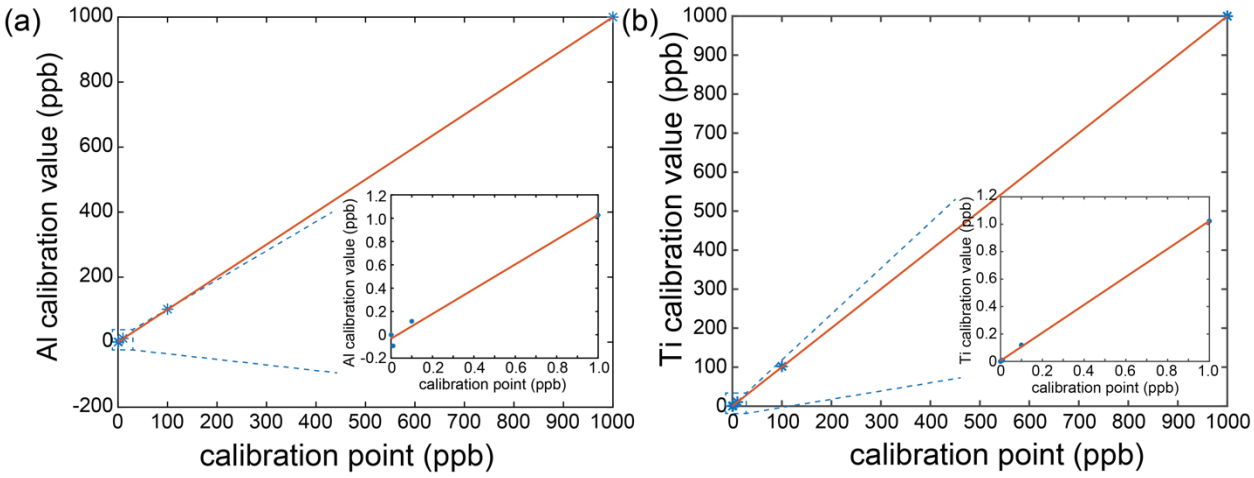
Supplemental Figure 2.1 SEM Images of ALD TiO_x deposited at different temperatures (a) **R1** (100 ms $TiCl_4$ + 2 s purge + 50 ms H_2O + 2 s purge) ALD TiO_x deposited on Si at 120°C (the scale bar is 5 µm), (b) **R1** ALD TiO_x deposited on Si at 250°C (the scale bar is 5 µm) and a zoom in image polycrystalline TiO_x was synthesized at high temperature (the scale bar is 500 nm).



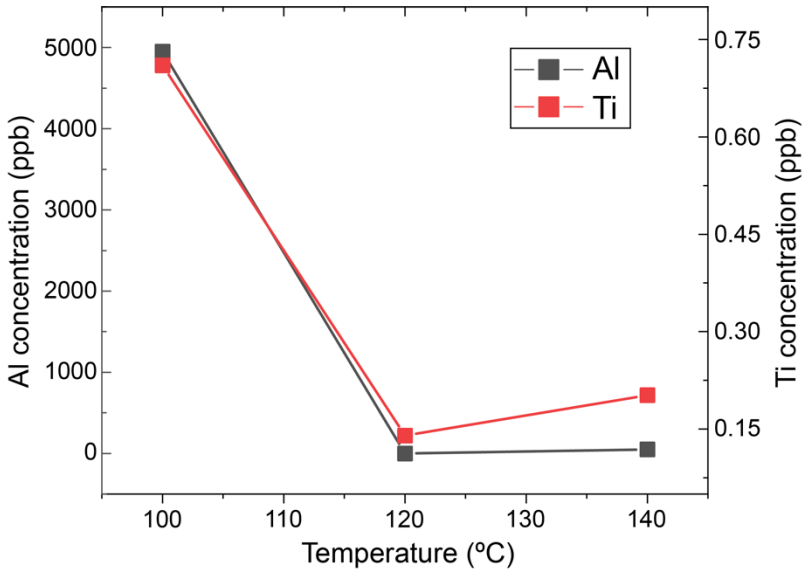
Supplemental Figure 2.2 AES and EDS characterization on different ALD TiO_x (a) SEM EDS characterization of ALD TiO_x deposited with recipe R1, (b) SEM EDS characterization of ALD TiO_x deposited with recipe R3, (c) AES characterization of ALD TiO_x deposited with recipe R1, (d) AES characterization of ALD TiO_x deposited with recipe R3. Different oxidation level of TiO_x was derived successfully via optimizing the ALD recipes ($TiCl_4$ and H_2O pulse length.



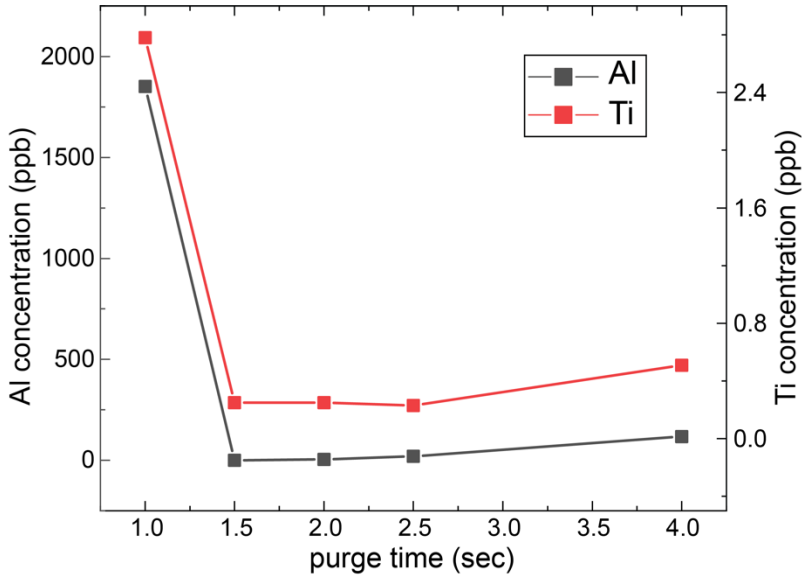
Supplemental Figure 2.3 Images of tested sample for corrosion test (potentiostatic test) (a) prepared Al sample covered with electrical tape shows the dimension of exposure area, (b) prepared Al sample connected to the sample holder indicated the region immersed into the solution during potentiostatic test, in the case that the reactive area was controlled to be ~0.785 cm^2.



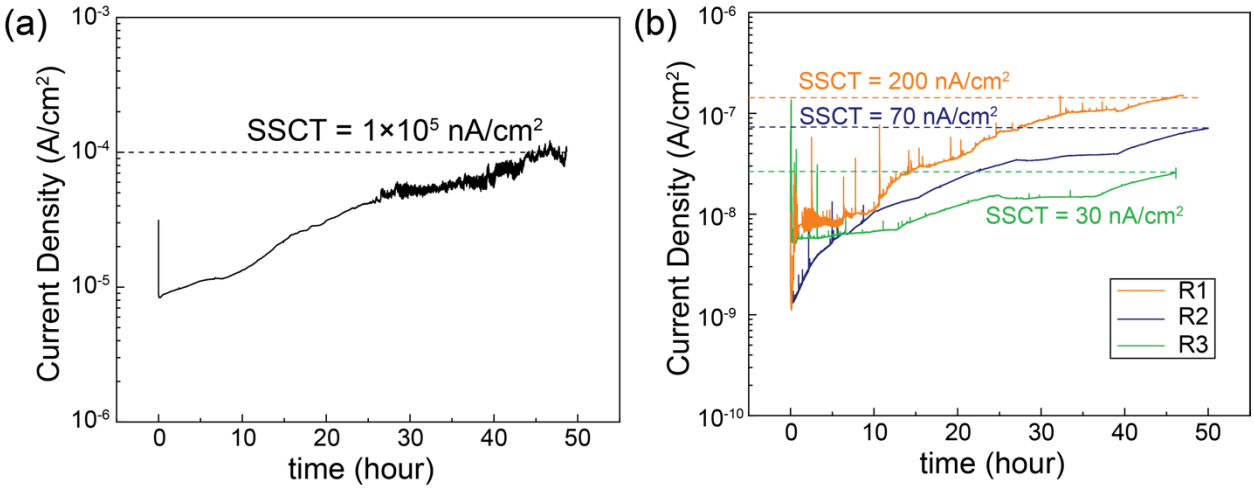
Supplemental Figure 2.4 ICP-MS calibration curve for Al and Ti ions. The measurement of Al^{3+} and Ti^{4+} concentration in solution after the potentiostatic testing was calibrated in a wide range - through the *blank* (forced zero) to 1000 ppb. The Al^{3+} has an accuracy calibrated at 0.1 ppb level and Ti^{4+} has an accuracy at 0.01 ppb level.



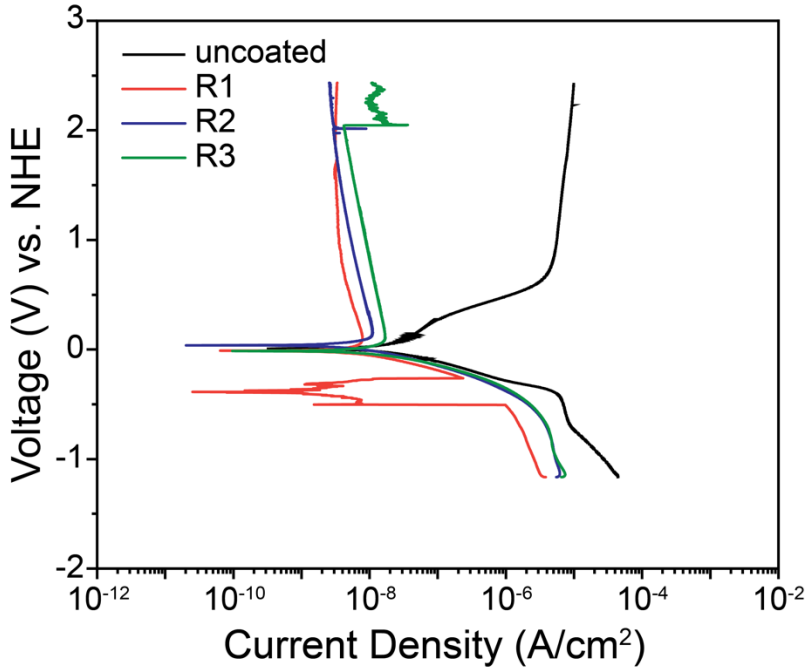
Supplemental Figure 2.5 ICP-MS characterization for ALD TiO_x temperature optimization, the temperature optimization of ALD TiO_x (**R2**) shows that the TiO_x deposited at 120 °C has the best corrosion resistance (lowest Al^{3+} and Ti^{4+} detected from ICP-MS)



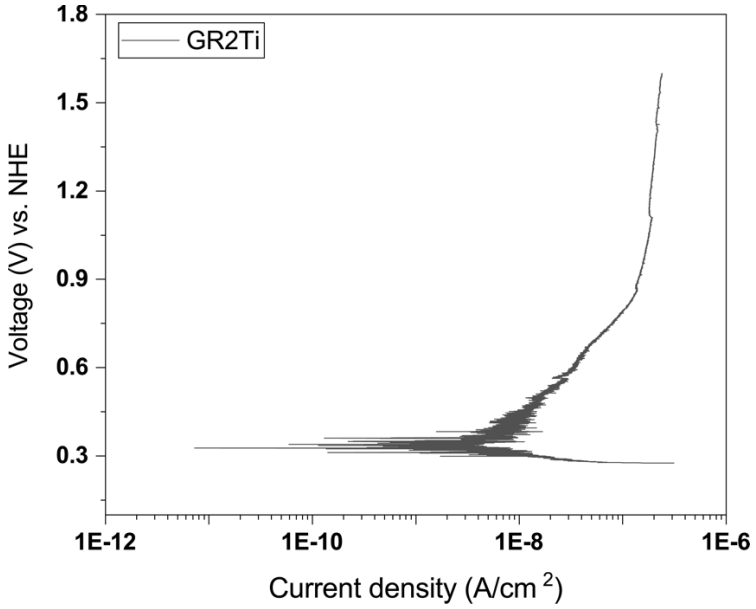
Supplemental Figure 2.6 ICP-MS characterization for ALD TiO_x purge time optimization, the purge time optimization of ALD TiO_x (150ms $TiCl_4$ + 50ms H_2O) shows that the TiO_x deposited with purge time of 1.5s – 2.5s has the best corrosion resistance (lowest Al^{3+} and Ti^{4+} detected from ICP-MS), indicated that the corrosion resistant TiO_x need combination of gas CVD and surface ALD which can be tuned via the optimization of ALD purge time.



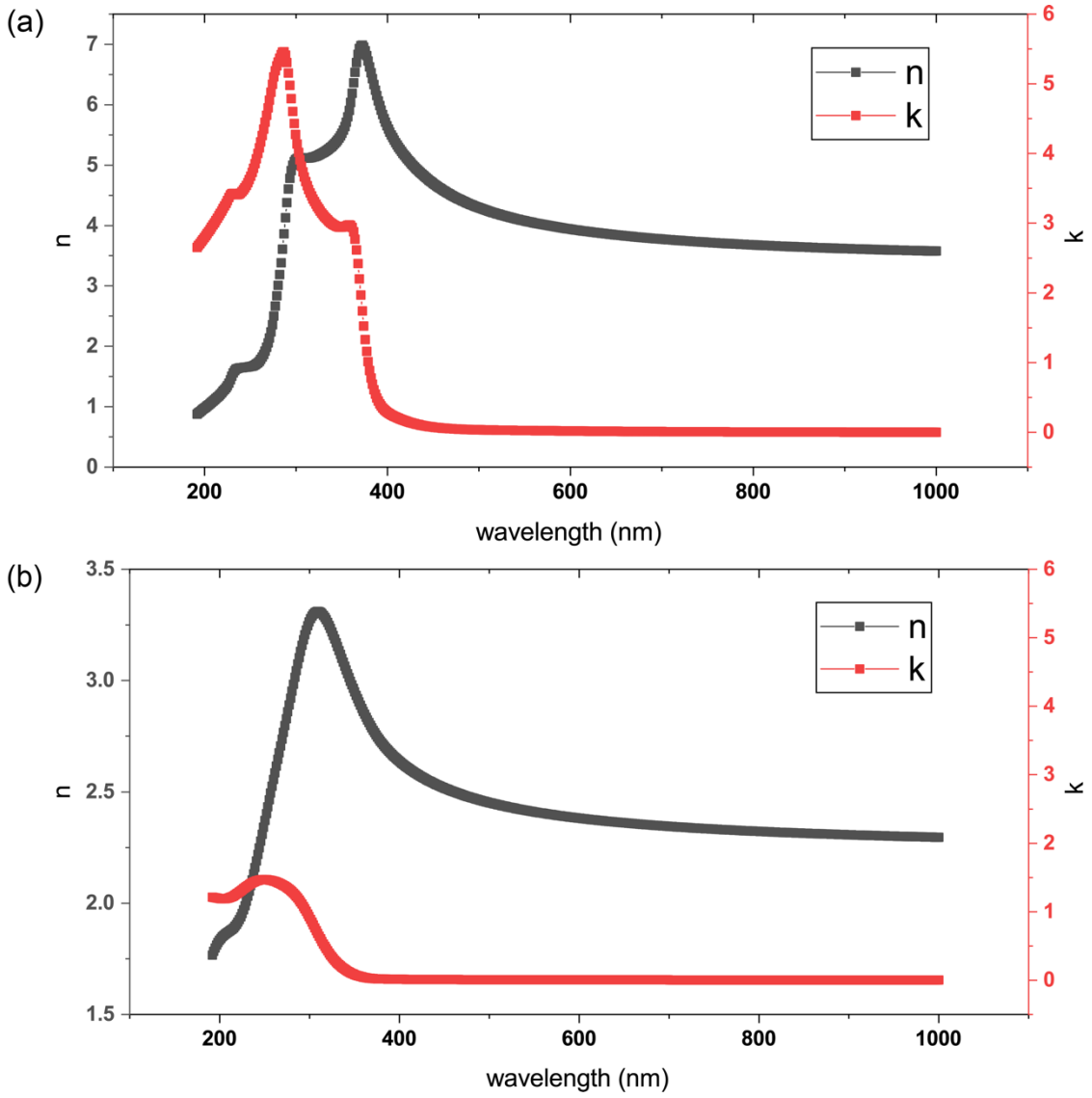
Supplemental Figure 2.7 Potentiostatic test of uncoated and ALD TiO_x coated Al substrate, (a) potentiostatic test of uncoated EP Al 1100 shows a repassivation process at the initial point (decrease of current density) and a high steady state current density at 50 hours indicated a high corrosion rate of Al substrate, (b) ALD TiO_x coated EP Al 1100 resulted in orders of magnitude lower steady state current density at 50 hours in the potentiostatic test, and ALD TiO_x coated with R3 also has an initial passivation process (rapid drop of current density) indicated existed pinholes that have Al substrate exposure to the sulfuric acid.



Supplemental Figure 2.8 Polarization curves of uncoated and ALD TiO_x coated Al substrate, ALD TiO_x coated EP Al 1100 revealed lower corrosion current density compared to the uncoated EP Al 1100. The ALD TiO_x coated with R2 recipe manifested the highest positive corrosion potential and low J_{corr}.



Supplemental Figure 2.9 Polarization curves of GR2 Ti, The GR2 Ti electrode has a J_{corr} of ~ 10 nA cm^{-2} and E_{corr} of ~ 300 mV. Our ALD TiO_x coated Al with recipe R2 has the same scale of corrosion current density compared to the GR2 Ti electrode indicated that our ALD TiO_x coated Al could be a feasible replacement of Ti electrode.



Supplemental Figure 2.10 Optical constant vs. nm of (a) Si and (b) TiO_x, the ALD TiO_x thickness was measured on Si assuming monolayer TiO_x on Si substrate with the optical constant for (a) Si and (b) TiO_x

2.11 Acknowledgements

This work was performed in part at the San Diego Nanotechnology Infrastructure (SDNI) of UCSD, a member of the National Nanotechnology Coordinated Infrastructure, which is supported by the National Science Foundation (Grant ECCS-2025752). The authors would like to

thank Dr. Neal Arakawa, of the Environmental and Complex Analysis Laboratory at UC, San Diego for assistance with the ICP-MS measurements.

Chapter 2, in full, is a reprint of the material as it appears in "Enhanced Corrosion Resistance in Aluminum-Based Electrolyzer Components via Stoichiometry Tuned Atomic Layer-Deposited TiO_x Films." *ACS Applied Materials & Interfaces* 16, no. 27 (2024): 35043-35052 by Kesong Wang, Adam Paxson, Thomas I. Valdez, Ahmet Erlat, Ping-Che Lee, Seonguk Yun, Pranjali Khajanji, Zichen Zhang, Andrew C. Kummel, and Prabhakar Bandaru. The dissertation author was the primary investigator and author of this paper.

2.12 References

(1) Jiang, S. P.; Li, Q. Fuel Cell Electrochemistry. In *Introduction to Fuel Cells*; Springer Singapore: Singapore, 2022; pp 69–122. https://doi.org/10.1007/978-981-10-7626-8_3.

(2) Kovač, A.; Paranos, M.; Marciuš, D. Hydrogen in Energy Transition: A Review. *Int J Hydrogen Energy* **2021**, *46* (16), 10016–10035. https://doi.org/10.1016/j.ijhydene.2020.11.256.

(3) Falcão, D. S.; Pinto, A. M. F. R. A Review on PEM Electrolyzer Modelling: Guidelines for Beginners. *J Clean Prod* **2020**, *261*, 121184. https://doi.org/10.1016/j.jclepro.2020.121184.

(4) Nafeh, A. E. A. Hydrogen Production from a PV/PEM Electrolyzer System Using a Neural-network-based MPPT Algorithm. *International Journal of Numerical Modelling: Electronic Networks, Devices and Fields* **2011**, *24* (3), 282–297. https://doi.org/10.1002/jnm.778.

(5) Hou, Y.; Lv, J.; Quan, W.; Lin, Y.; Hong, Z.; Huang, Y. Strategies for Electrochemically Sustainable H_2 Production in Acid. *Advanced Science* **2022**, *9* (7). https://doi.org/10.1002/advs.202104916.

(6) Calcerrada, A. B.; de la Osa, A. R.; Llanos, J.; Dorado, F.; de Lucas-Consuegra, A. Hydrogen from Electrochemical Reforming of Ethanol Assisted by Sulfuric Acid Addition. *Appl Catal B* **2018**, *231*, 310–316. https://doi.org/10.1016/j.apcatb.2018.03.028.

(7) Sun, C.-W.; Hsiau, S.-S. Effect of Electrolyte Concentration Difference on Hydrogen Production during PEM Electrolysis. *Journal of Electrochemical Science and Technology* **2018**, *9* (2), 99–108.

(8) Park, I. K.; Ahn, C.-Y.; Lee, J. H.; Lee, D. W.; Lee, C. H.; Cho, Y.-H.; Sung, Y.-E. Three-Dimensionally Interconnected Titanium Foam Anode for an Energy-Efficient Zero Gap-Type Chlor-Alkali Electrolyzer. *Int J Hydrogen Energy* **2019**, *44* (31), 16079–16086. https://doi.org/10.1016/j.ijhydene.2019.04.230.

(9) Choi, H.; Kim, O.-H.; Kim, M.; Choe, H.; Cho, Y.-H.; Sung, Y.-E. Next-Generation Polymer-Electrolyte-Membrane Fuel Cells Using Titanium Foam as Gas Diffusion Layer. *ACS Appl Mater Interfaces* **2014**, *6* (10), 7665–7671. https://doi.org/10.1021/am500962h.

(10) McCafferty, E. Thermodynamics of Corrosion: Pourbaix Diagrams. In *Introduction to Corrosion Science*; Springer New York: New York, NY, 2010; pp 95–117. https://doi.org/10.1007/978-1-4419-0455-3_6.

(11) Xing, Y.; Li, H.; Avgouropoulos, G. Research Progress of Proton Exchange Membrane Failure and Mitigation Strategies. *Materials* **2021**, *14* (10), 2591. https://doi.org/10.3390/ma14102591.

(12) Feng, Q.; Yuan, X.; Liu, G.; Wei, B.; Zhang, Z.; Li, H.; Wang, H. A Review of Proton Exchange Membrane Water Electrolysis on Degradation Mechanisms and Mitigation Strategies. *J Power Sources* **2017**, *366*, 33–55. https://doi.org/10.1016/j.jpowsour.2017.09.006.

(13) Perks, C.; Mudd, G. Titanium, Zirconium Resources and Production: A State of the Art Literature Review. *Ore Geol Rev* **2019**, *107*, 629–646. https://doi.org/10.1016/j.oregeorev.2019.02.025.

(14) Sverdrup, H. U.; Sverdrup, A. E. An Assessment of the Global Supply, Recycling, Stocks in Use and Market Price for Titanium Using the WORLD7 Model. *Sustainable Horizons* **2023**, *7*, 100067. https://doi.org/10.1016/j.horiz.2023.100067.

(15) Hatch, J. E. *Aluminum Association. Aluminum: Properties and Physical Metallurgy*; ASM international, 1984.

(16) Saji, S.; Yasuhara, K.; Hori, S. Mechanical Properties of 7075 Aluminum Alloy at 6&Ndash;130 K. *Transactions of the Japan Institute of Metals* **1987**, *28* (10), 773–780. https://doi.org/10.2320/matertrans1960.28.773.

(17) Altıparmak, S. C.; Yardley, V. A.; Shi, Z.; Lin, J. Challenges in Additive Manufacturing of High-Strength Aluminium Alloys and Current Developments in Hybrid Additive Manufacturing. *International Journal of Lightweight Materials and Manufacture* **2021**, *4* (2), 246–261. https://doi.org/10.1016/j.ijlmm.2020.12.004.

(18) Buchheit, R. G. A Compilation of Corrosion Potentials Reported for Intermetallic Phases in Aluminum Alloys. *J Electrochem Soc* **1995**, *142* (11), 3994–3996. https://doi.org/10.1149/1.2048447.

(19) Adams, F. V.; Akinwamide, S. O.; Obadele, B.; Olubambi, P. A. Comparison Study on the Corrosion Behavior of Aluminum Alloys in Different Acidic Media. *Mater Today Proc* **2021**, *38*, 1040–1043. https://doi.org/10.1016/j.matpr.2020.05.781.

(20) Dan, A.; Bijalwan, P. K.; Pathak, A. S.; Bhagat, A. N. A Review on Physical Vapor Deposition-Based Metallic Coatings on Steel as an Alternative to Conventional Galvanized Coatings. *J Coat Technol Res* **2022**, *19* (2), 403–438. https://doi.org/10.1007/s11998-021-00564-z.

(21) Sun, W.; Wang, L.; Yang, Z.; Li, S.; Wu, T.; Liu, G. Fabrication of Polydimethylsiloxane-Derived Superhydrophobic Surface on Aluminium via Chemical Vapour Deposition Technique for Corrosion Protection. *Corros Sci* **2017**, *128*, 176–185. https://doi.org/10.1016/j.corsci.2017.09.005.

(22) Fu, J.; Sun, Y.; Ji, Y.; Zhang, J. Fabrication of Robust Ceramic Based Superhydrophobic Coating on Aluminum Substrate via Plasma Electrolytic Oxidation and Chemical Vapor Deposition Methods. *J Mater Process Technol* **2022**, *306*, 117641. https://doi.org/10.1016/j.jmatprotec.2022.117641.

(23) George, S. M. Atomic Layer Deposition: An Overview. *Chem Rev* **2010**, *110* (1), 111–131. https://doi.org/10.1021/cr900056b.

(24) Santinacci, L. Atomic Layer Deposition: An Efficient Tool for Corrosion Protection. *Curr Opin Colloid Interface Sci* **2023**, *63*, 101674. https://doi.org/10.1016/j.cocis.2022.101674.

(25) Sammelselg, V.; Netšipailo, I.; Aidla, A.; Tarre, A.; Aarik, L.; Asari, J.; Ritslaid, P.; Aarik, J. Chemical Resistance of Thin Film Materials Based on Metal Oxides Grown by Atomic Layer Deposition. *Thin Solid Films* **2013**, *542*, 219–224. https://doi.org/10.1016/j.tsf.2013.06.079.

(26) Ohring, M. *Materials Science of Thin Films: Depositon and Structure*, 2nd ed.; Elsevier, 2001.

(27) Singh, A. K.; Adstedt, K.; Brown, B.; Singh, P. M.; Graham, S. Development of ALD Coatings for Harsh Environment Applications. *ACS Appl Mater Interfaces* **2019**, *11* (7), 7498–7509. https://doi.org/10.1021/acsami.8b11557.

(28) Liu, X.; Yang, Q.; Li, Z.; Yuan, W.; Zheng, Y.; Cui, Z.; Yang, X.; Yeung, K. W. K.; Wu, S. A Combined Coating Strategy Based on Atomic Layer Deposition for Enhancement of Corrosion Resistance of AZ31 Magnesium Alloy. *Appl Surf Sci* **2018**, *434*, 1101–1111. https://doi.org/10.1016/j.apsusc.2017.11.032.

(29) Cremers, V.; Puurunen, R. L.; Dendooven, J. Conformality in Atomic Layer Deposition: Current Status Overview of Analysis and Modelling. *Appl Phys Rev* **2019**, *6* (2). https://doi.org/10.1063/1.5060967.

(30) Panjan, P.; Drnovšek, A.; Gselman, P.; Čekada, M.; Panjan, M. Review of Growth Defects in Thin Films Prepared by PVD Techniques. *Coatings* **2020**, *10* (5), 447. https://doi.org/10.3390/coatings10050447.

(31) Morosanu, C. E. *Thin Films by Chemical Vapour Deposition*; Elsevier, 2016; Vol. 7.

(32) Seo, S.-W.; Jung, E.; Lim, C.; Chae, H.; Cho, S. M. Moisture Permeation through Ultrathin TiO$_{2}$ Films Grown by Atomic Layer Deposition. *Applied Physics Express* **2012**, *5* (3), 035701. https://doi.org/10.1143/APEX.5.035701.

(33) Fusco, M.; Oldham, C.; Parsons, G. Investigation of the Corrosion Behavior of Atomic Layer Deposited Al2O3/TiO2 Nanolaminate Thin Films on Copper in 0.1 M NaCl. *Materials* **2019**, *12* (4), 672. https://doi.org/10.3390/ma12040672.

(34) Hefny, M. M.; Mazhar, A. A.; El-Basiouny, M. S. Dissolution Behaviour of Titanium Oxide in H_2SO_4 and NaOH from Impedance. and Potential Measurements. *British Corrosion Journal* **1982**, *17* (1), 38–41. https://doi.org/10.1179/000705982798274633.

(35) Nowotny, M. K.; Bak, T.; Nowotny, J. Electrical Properties and Defect Chemistry of TiO_2 Single Crystal. I. Electrical Conductivity. *J Phys Chem B* **2006**, *110* (33), 16270–16282. https://doi.org/10.1021/jp0606210.

(36) Pham, H. H.; Wang, L.-W. Oxygen Vacancy and Hole Conduction in Amorphous TiO_2. *Physical Chemistry Chemical Physics* **2015**, *17* (1), 541–550. https://doi.org/10.1039/C4CP04209C.

(37) Smolinka, T.; Bergmann, H.; Garche, J.; Kusnezoff, M. The History of Water Electrolysis from Its Beginnings to the Present. In *Electrochemical Power Sources: Fundamentals, Systems, and Applications*; Elsevier, 2022; pp 83–164. https://doi.org/10.1016/B978-0-12-819424-9.00010-0.

(38) Kozlovskiy, A.; Shlimas, I.; Dukenbayev, K.; Zdorovets, M. Structure and Corrosion Properties of Thin TiO2 Films Obtained by Magnetron Sputtering. *Vacuum* **2019**, *164*, 224–232. https://doi.org/10.1016/j.vacuum.2019.03.026.

(39) Tepe, S. A.; Danışman, M.; Cansever, N. Crystallization of TiO2 on Sputter Deposited Amorphous Titanium Thin Films. *Mater Chem Phys* **2022**, *282*, 125965. https://doi.org/10.1016/j.matchemphys.2022.125965.

(40) Vincent, T.; Hsu, J.; Wu, V.; Wills, J. *Routine determination of ultratrace elements in semiconductor grade nitric acid by the Thermo Scientific iCAP RQ ICP-MS*. thermofisher scientific website. https://www.thermofisher.com/order/catalog/product/BRE731416 (accessed 2024-02-23).

(41) Seah, M. P. Quantification in AES and XPS. In *Quantitative Microbeam Analysis*; Routledge, 2017; pp 1–42.

(42) Abd Mutalib, M.; Rahman, M. A.; Othman, M. H. D.; Ismail, A. F.; Jaafar, J. Scanning Electron Microscopy (SEM) and Energy-Dispersive X-Ray (EDX) Spectroscopy. In *Membrane Characterization*; Elsevier, 2017; pp 161–179. https://doi.org/10.1016/B978-0-444-63776-5.00009-7.

(43) Goldstein, J. I.; Newbury, D. E.; Michael, J. R.; Ritchie, N. W.; Scott, J. H. J.; Joy, D. C. *Scanning Electron Microscopy and X-Ray Microanalysis*; springer, 2017.

(44) Cliff, G.; Lorimer, G. W. The Quantitative Analysis of Thin Specimens. *J Microsc* **1975**, *103* (2), 203–207. https://doi.org/10.1111/j.1365-2818.1975.tb03895.x.

(45) Woodruff, D. P. *Modern Techniques of Surface Science*, Third edition.; Cambridge university press, 2016; Vol. 1.

(46) Chang, C. C. Auger Electron Spectroscopy. *Surf Sci* **1971**, *25* (1), 53–79. https://doi.org/10.1016/0039-6028(71)90210-X.

(47) Shimizu, R. Quantitative Analysis by Auger Electron Spectroscopy. *Jpn J Appl Phys* **1983**, *22* (11R), 1631. https://doi.org/10.1143/JJAP.22.1631.

(48) Abdulagatov, A. I.; Yan, Y.; Cooper, J. R.; Zhang, Y.; Gibbs, Z. M.; Cavanagh, A. S.; Yang, R. G.; Lee, Y. C.; George, S. M. Al_2O_3 and TiO_2 Atomic Layer Deposition on Copper for Water Corrosion Resistance. *ACS Appl Mater Interfaces* **2011**, *3* (12), 4593–4601. https://doi.org/10.1021/am2009579.

(49) Marin, E.; Lanzutti, A.; Paussa, L.; Guzman, L.; Fedrizzi, L. Long Term Performance of Atomic Layer Deposition Coatings for Corrosion Protection of Stainless Steel. *Materials and Corrosion* **2015**, *66* (9), 907–914. https://doi.org/10.1002/maco.201408012.

(50) Bard, A. J.; Faulkner, L. R.; White, H. S. *Electrochemical Methods: Fundamentals and Applications*; John Wiley & Sons, 2022.

(51) Colin, J.; Serna, S.; Campillo, B.; Florez, O.; Gonzalez-Rodriguez, J. G. Corrosion Performance of a Rapidly Solidified NiAl Intermetallic Macroallolled with Fe in 0.5 MH2so4. *Int J Electrochem Sci* **2007**, *2* (12), 947–957.

(52) Perez, N. *Electrochemistry and Corrosion Science Second Edition*, 2nd ed.; Springer, 2016.

(53) J. Burton, *Certificate of Analysis*, Fair Lawn, **2023**.

Chapter 3 TiO_x/Al_2O_3 laminate atomic layer deposited (ALD) films to enable corrosion prot4ection of aluminum screens and porous components in water electrolyzers

3.1 Abstract

This study presents a multi-step approach to enhance the corrosion resistance of aluminum (Al) screens used in the flow fields of water electrolyzers, allowing for the higher thermal conductivity material, Al, to replace titanium (Ti) in electrolyzer gas diffusion components. The approach involves electropolishing, O_2 treatment, and conformal atomic layer deposition (ALD) of an Al_2O_3 adhesion layer followed by a bilayer TiO_x protection coating on the Al screens. It is shown that optimized coatings reduce corrosion current density by four orders of magnitude compared to uncoated Al, with a corrosion rate of ~7 nm per year, ensuring protection of components with the complex geometries of the electrolyzer gas diffusion layer (GDL) flow field. This work provides a viable pathway to replace expensive titanium with abundant, cost-effective aluminum.

3.2 Introduction

The increasing global demand for clean and sustainable energy has propelled green hydrogen[1] to the forefront of research and industrial development[2,3], with applications spanning transportation[4], electricity generation[5], and energy storage[5,6]. Water electrolysis, powered by renewable energy sources, is a leading method for green hydrogen production[7,8]. **Fig. 3.1(a)** illustrates the working mechanism of a proton exchange membrane water electrolyzer (PEMWE), highlighting the process of water splitting into hydrogen and oxygen[9]. The related layout of the anode compartment is shown in **Fig. 3.1(b)**, comprising a catalyst layer, a gas diffusion layer (GDL), and a bipolar plate[10]. The GDL, typically formed from a porous transport layer (PTL) and a flow field constructed from multilayer meshed metal screens, plays a crucial role in facilitating

efficient gas transport[10] by ensuring uniform distribution and removal of the oxygen byproduct from the electrodes, while simultaneously supplying coolant water flow[11].

GDLs in proton exchange membrane (PEM) water electrolyzers presently rely on titanium (Ti) based components[12], incorporating low resistivity, high thermal conductivity, and electrochemical stability[13] under typical water electrolyzer operating conditions (low pH < 5 and high electrical potential ~2.4 V vs. RHE)[14–16]. However, the high cost and limited availability of Ti[17,18] pose significant challenges for widespread utilization. Moreover, Ti is susceptible to anodization at high voltages resulting in the accumulation of surface oxides[19], which increases electrical and thermal resistance. Such an effect then necessitates the application of a thin, precious metal coating, such as platinum (Pt)[13,20,21]. This additional requirement further escalates the cost associated with Ti utilization. Consequently, exploring cost-effective alternatives is crucial. Aluminum (Al) is an attractive alternative, with lower density, higher electrical conductivity, and higher thermal conductivity[22,23]. However, the susceptibility of Al to corrosion under electrolyzer operating conditions[24] must be controlled and our work indicates that this may be done through the use of optimized adhesion layers *along* with conformal protection layers, where pinholes large enough to permit electrolyte flow and induce corrosion of the underlying film and substrate are effectively eliminated.

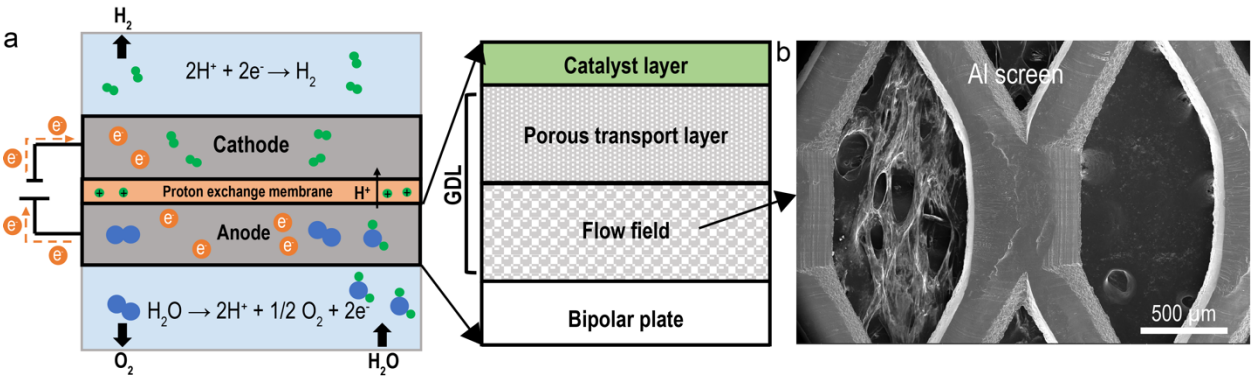


Figure 3.1 Schematic representation of **(a)** proton exchange membrane (PEM) water electrolyzer and the constituent anode pack configuration with the gas diffusion layer (GDL), indicating the meshed aluminum (Al) screens used in the flow field. **(b)** Scanning electron microscope (SEM) image of a typical Al screen, coating of which involves intricate geometry and must contend with intrinsic as well as extrinsic roughness at various scales.

As may be deduced from **Fig. 3.1(b),** a key challenge in protecting the Al flow field screens would be achieving conformal and uniform coatings given their intricate geometry and roughness. Among various thin-film deposition techniques, atomic layer deposition (ALD) is a promising approach due to its capability for producing such high-quality coatings with precise atomic-scale thickness control[25,26]. Indeed, compared to physical vapor deposition (PVD) – which has issues related to uniform coverage on complex surfaces[27]-, and sol-gel techniques – which suffer from poor adhesion and mechanical instability[28,29]-, ALD enables the formation of dense, predominantly defect-free films with high-quality interfaces, making it suitable for the corrosion protection of Al screens.

In this study, the development of an optimized multi-step process is reported comprising (i) electropolishing (*EP*), (ii) oxygen treatment, followed by an (iii) adhesion layer, and (iv) multiple layer protective coatings for the Al screens. The results indicate that a ~50 nm optimized ALD coating can provide sufficient corrosion protection for a typical water electrolyzer stack, with

an operational lifespan of ~60,000 hours[30], assuming that all other failure mechanisms not addressed in this study are effectively mitigated.

3.3 Experimental section

Materials and sample preparation

The mesh aluminum (Al 1100, wt. % composition: 99.0–99.95% Al, 0.05–0.20% Cu, ≤0.95% Fe, ≤0.05% Mg, ≤0.95% Si, ≤0.1% Zn) screen, as shown in **Fig. 3.1(b),** was considered as a possible replacement for Ti to constitute the flow field in the gas diffusion layer (GDL) of the water electrolyzer. The meshed Al samples were initially diced into 1.2 cm × 1.5 cm pieces and subsequently electropolished (*EP*) in a mixture of phosphoric acid and sulfuric acid (4:1), stirred at 200 rpm, at 80 °C under a constant applied voltage of 5 V. The voltage for the *EP* was identified, from the current *(I)* – voltage (*V*) characteristics, shown in **Fig. S3.1** (*Supporting Information*). Following *EP*, the samples were rinsed in 28-30% ammonium hydroxide (NH_4OH) at room temperature for 30 seconds. The cleaned samples were then subjected to ultrasonic cleaning, consecutively in acetone, isopropanol (IPA), and deionized (DI) water, for 5 minutes each, with nitrogen blow-dry between each cleaning step to remove excess solvents.

Oxygen treatment for removal of surface contaminations

The carbonaceous residues and contaminants on the *EP* Al samples that could interfere with conformal atomic layer deposition (ALD) were removed by subjecting the samples to (a) an oxygen plasma treatment (using an Oxford Plasma Lab 80 Plus RIE), and subsequently to (b) oxygen annealing at 450 °C for 30 minutes (in an AccuThermo AW 610 rapid thermal processor: RTP).

Atomic layer deposition (ALD) of multi-layer protection film

Using ALD (Beneq TFS 200), an Al_2O_3 adhesion layer was first deposited on the aluminum substrate at 250 ℃ followed by a TiO_x corrosion protection layer at 120 ℃. For Al_2O_3 deposition, trimethylaluminum (TMA) and H_2O were used as the precursors, with a typical ALD cycle consisting of a 100 ms TMA pulse, followed by a 3 s nitrogen gas purge, a 100 ms H_2O pulse, and a 5 s purge. TiO_x deposition used titanium tetrachloride ($TiCl_4$) and H_2O as precursors with a typical ALD cycle including 150 ms $TiCl_4$ and 50 ms H_2O pulses, based on a previously optimized recipe[31]. To mitigate the formation of pinholes on relatively rough substrates, a short-purge ALD TiO_x process (1 s purge time) was employed as a seed layer, prior to the outer corrosion protection layer. The related process combines gas-phase chemical vapor deposition (CVD) with surface ALD to enhance film conformity. The outer layer was applied using a long-purge ALD TiO_x process (2 s purge time). The deposition rates of Al_2O_3 and TiO_x, were monitored by recording the film thicknesses using ellipsometry (J.A. Woollam M-20000D), at ~0.1 nm and ~0.04 nm per cycle, respectively.

Surface characterization

The surface morphology and topography of the unpolished (*UP*) and *EP* Al screens were characterized through both optical microscopy and atomic force microscopy (AFM: Park NX20). Tapping mode AFM (NSC15/Al BS AFM tip, Park Systems), was deployed to assess the roughness of the samples over several 10 μm × 10 μm regions before and after *EP*. The penetration ability and compositional uniformity of the ALD layers through the porous transport layer (PTL) of the GDL was investigated using scanning electron microscopy (SEM) and energy dispersive spectroscopy (EDS). The interfacial morphology of the ALD layers was characterized using transmission electron microscopy (TEM: ThermoFisher Talos 200X).

Corrosion testing

The robustness of the ALD coatings and the coated substrates were tested in sulfuric acid solutions at a molarity of 1 mM (pH 3), under a constant voltage of 2.4 V (*vs.* the reversible hydrogen electrode, RHE), corresponding to typical conditions used for commercial water electrolyzers[14–16]. A three-electrode setup was employed for the corrosion tests, with the test sample as the working electrode (WE), the RHE as the reference electrode (RE), and a Pt wire as the counter electrode (CE). The electrical potential difference corresponding to the test voltage was applied between the WE and the RE. In the potentiostatic (PS) tests, the Al screen samples, with a sampling area of ~2.5 cm² (surface area estimated as shown in **Fig. S3.2** of *the Supporting Information*), were immersed in the solution for up to 50 hours. The samples were left in the solution for 5 minutes prior to testing to determine the open circuit potential (E_{OC}). During PS testing, the current density (J) was monitored (using a Gamry 5000E potentiostat). Electrochemical impedance spectroscopy (EIS) was performed before and after the PS testing over a frequency range of 1 MHz to 0.2 Hz with 10 points per decade and a 10 mV AC perturbation applied to the 2.4 V DC. EIS data fitting was done using Gamry Echem Analyst® software, with specific resistance – capacitance circuit models.

Additionally, potentiodynamic (PD) tests were conducted both before and after the PS testing, with voltage scans ranging from -0.6 V *vs.* E_{OC} to 2.4 V *vs.* RHE in 1 mM H_2SO_4. The corrosion current density (J_{corr}) and corrosion potential (E_{corr}) were recorded from the polarization curves, and Tafel fits were performed within the -50 mV to 50 mV *vs*. E_{OC} region. The polarization resistance (R_p) was estimated using the Stern-Geary relation[32,33]:

$$R_p = \frac{\beta_a \beta_c}{2.303 J_{corr}(\beta_a + \beta_c)} \qquad (3.1)$$

where β_a and β_c are the Tafel slopes for the anodic and cathodic regions, respectively. All measurements were repeated at least three times to assess the random error.

Inductively coupled plasma mass spectrometry (ICP-MS)

The loss of Ti (in the form of Ti^{4+} ions) from the coating, as well as Al (in the form of Al^{3+} ions) from the Al screen, was monitored at the 0.1 ppb and 0.01 ppb levels, respectively using ICP-MS (iCAP RQ), with detection limits of 0.3 ng L^{-1} for Al and 0.8 ng L^{-1} for Ti[34]. Typically, ~2 ml samples of the acid solutions were removed and tested periodically during the potentiostatic (PS) testing. The Al^{3+} and Ti^{4+} concentrations were carefully calibrated over a range of 0.01 ppb to 1000 ppb in 1% trace metal nitric acid (blank), diluted from TraceMetal™ Grade nitric acid (Fisher Chemical™), to ensure the accuracy of the test results. The blank (1% trace metal nitric acid) was set to zero for reference, and all obtained values equal to or smaller than zero were treated as indicating no loss in this study.

A coating layer was developed to enhance the corrosion resistance of Al screens in the flow field structures of the water electrolyzers (**Fig. 3.1(b))** and to mitigate the potential damage[35,36] caused by Al^{3+} ions to the membrane layer. The coating process, illustrated in **Fig. 3.2**, is mainly composed of five steps starting with (i) dicing of the screens (Diced screens shown as "Original material" in Fig. 2), (ii) electropolishing to reduce surface roughness, (iii) oxygen plasma and annealing treatments to reduce surface contamination - typically from hydrocarbons-, (iv) deposition of an ALD Al_2O_3 adhesion layer to enhance the bond between the underlying Al screen and a top ALD TiO_x layer, and finally (v) application of a corrosion-resistant TiO_x layer, which includes a short purge (1s) ALD TiO_x followed by a long purge (2s) ALD TiO_x layer. The deposition of an adhesion layer was found necessary to potentially eliminate pinholes at the screen

– TiO_x interface. The surface pretreatment processes in steps (ii) and (iii) are further discussed in Section 3.1, while the ALD deposition pertinent to steps (iv) and (v) is discussed in Section 3.5.

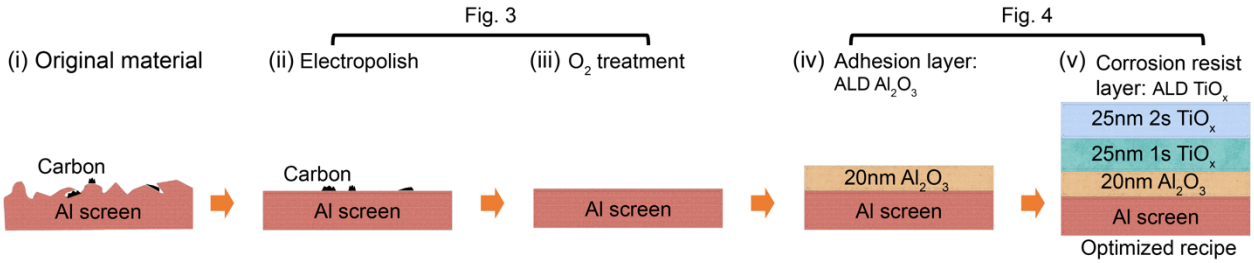


Figure 3.2 Schematic of fabrication processes related to corrosion protection layers, (i) the diced aluminum 1100 screens – with surface roughness and contamination, followed by **(ii)** electropolishing to reduce surface roughness, **(iii)** O_2 plasma and annealing to remove carbon contamination, **(iv)** thin ALD Al_2O_3 adhesion layer, and **(v)** corrosion resistant ALD TiO_x layer with short (1 s) and long (2 s) purge time. Details related to **(ii)** and **(iii)** will be further elaborated in **Fig. 3.3,** while aspects related to **(iv)** and **(v)** will be discussed in **Fig. 3.4.**

The layer and interfacial structure of the ALD coatings on the Al screens was quantified using TEM, as indicated in **Fig. S3.3(a)** of *the Supporting Information*. Multiple distinct layers were observed: (1) an AlO_x layer was seen adjacent to the screen, presumably formed due to the oxygen plasma and annealing treatments, (2) the 20 nm ALD Al_2O_3 *adhesion* layer, (3) two 25 nm layers of ALD TiO_x *corrosion protection* layers (the first layer arising from the short purge and the second from the long purge cycles). The ALD layers seem amorphous in character and successive layers appear distinct. The atomic fractions, as determined through EDS, of the elements shown in **Fig. S3.3(b)** of the *Supporting Information* indicate uniform stoichiometry. Further TEM analysis and EDS mapping of the sample is presented in **Fig. S3.4** of the *Supporting Information*.

3.4 Surface treatment optimization

To enhance the surface smoothness and mitigate the formation of pinholes during subsequent coating process, the diced Al screens were first electropolished (*EP*). The substantial reduction of the roughness at the center joint location shown in **Fig. 3.1(b)** is indicated in **Fig. 3.3(b)**. Further, Atomic Force Microscopy (AFM) measurements, shown in **Fig. S3.1b** (*Supporting Information*), indicate a significant reduction in surface roughness from ~80 nm to ~10 nm after the *EP* treatment. The effectiveness of *EP* in reducing pinhole formation during ALD deposition of Al_2O_3 and TiO_x coatings were tested through the ICP-MS characterization of the test solution into which the coated screen samples were immersed during the potentiostatic (PS) test. It was seen *e.g.,* **Fig. 3.3(c),** that when *EP* was utilized, the Al^{3+} concentration in the solution was ~30× lower compared to when unpolished (*UP*) Al samples were used. It was noted that in *both* the *EP* and *UP* cases, the quantity of Ti^{4+} observed in ICP-MS was low and virtually unchanged: **Fig. 3.3(d)**. This is consistent with a small pinhole in the TiO_x layer leading to substantial dissolution of the Al substrate, which is more prone to corrosion than the TiO_x layer when exposed to the acid solution. Such corrosion behavior is in agreement with the previous studies on ALD TiO_x coatings for Al substrates[31], and further supported by the TEM analysis in **Fig. S3.5** (*Supporting Information*).

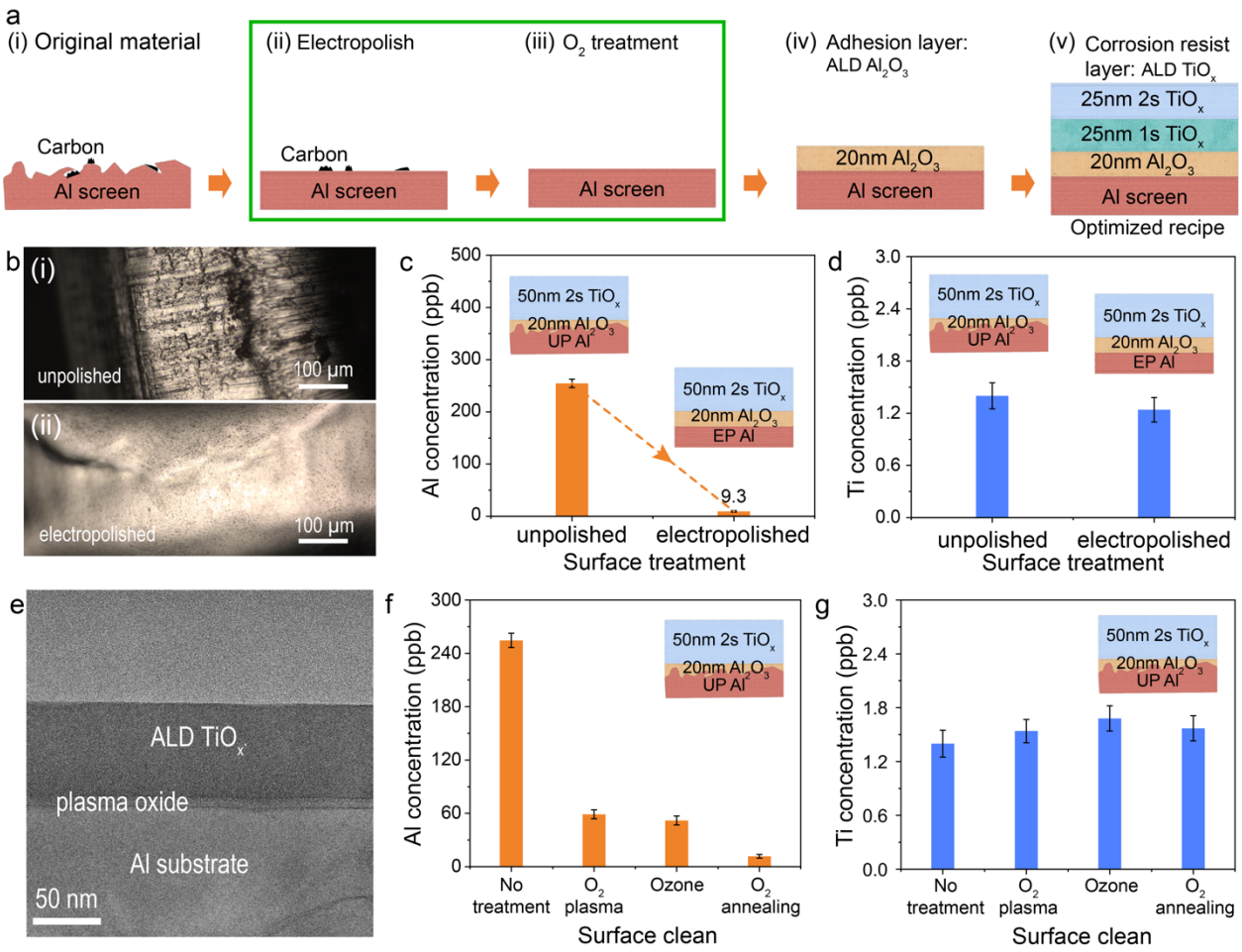


Figure 3.3 Characterization of surface treatment on corrosion resistance of Aluminum screens *prior* to ALD adhesion and protection layers (a) Investigating the influence of *EP* and oxygen treatment, **(b)** optical images contrasting the rough and the smooth surfaces of the unpolished (*UP*) and electropolished (*EP*) Al screens**.** ICP-MS determination of **(c)** Al^{3+}, and **(d)** Ti^{4+} following potentiostatic (PS) testing of the coated screens (see *inset*) in pH3 H_2SO_4 for 50 hours. **(e)** TEM characterization of oxide formed after oxygen plasma exposure of the substrate. ICP-MS determination of **(f)** Al^{3+}, and **(g)** Ti^{4+} following PS testing of the coated screens (see *inset*), subject to the specified oxygen cleaning treatments. While O_2 plasma and ozone surface treatments resulted in a reduction of Al^{3+} by more than four times, oxygen annealing prior to ALD deposition was found to yield much lower values. The robustness of the coating, in all cases, is shown by the relatively constant values for Ti^{4+}.

Surface contamination (for example from ambient hydrocarbons) can disrupt conformal ALD, leading to pinhole formation and preventing interaction between the Al screen substrate and ALD precursors[37–39]. To remove the hydrocarbons, oxygen treatments involving oxygen plasma,

oxygen annealing, and ozone, were utilized. It was shown that, in addition to removing the contaminants, oxygen plasma treatment generates a thin, uniform layer of oxide on the Al screen substrate, as shown in **Fig. 3.3(e)**. A detailed TEM EDS characterization for the plasma oxide layer is presented in **Fig. S3.6** (*Supporting Information*). ICP-MS analysis post-PS testing (**Fig. S3.7** of *the Supporting Information*) was used to confirm that the oxygen plasma treatment reduces Al substrate corrosion. When the plasma treatment was applied to both the top and bottom of the substrate, a factor of two decrease in the Al corrosion was observed, compared to when only one side was treated.

When UV-ozone cleaning or oxygen annealing—was utilized for surface contaminant removal separately, the latter was particularly useful in substantially reducing the Al substrate corrosion: **Fig. 3.3(f).** The Al^{3+} concentration was detected to be more than 20 times lower in the sample with O_2 annealing compared to the sample without any O_2 treatment. While the Al^{3+} concentration, as detected through ICP-MS, was sensitive to oxygen treatment, the Ti^{4+} concentration remained largely unaffected: **Fig. 3.3(g),** with the implication that the Al substrate is more prone to corrosion in the presence of pinholes in the protection layer (ALD Al_2O_3/TiO_x), predominantly residing in the TiO_x layer.

3.5 Protection layer optimization

ALD was used to deposit both an adhesion layer (Al_2O_3) and corrosion protection (TiO_x) layers. First, a 20 nm Al_2O_3 interlayer was introduced between the Al substrate and the TiO_x layer to improve interfacial adhesion[40,41] and this facilitated a six-fold reduction in Al^{3+} concentration: **Fig. 3.4(b).** The adhesion layer is expected to reduce ALD TiO_x pinhole formation.

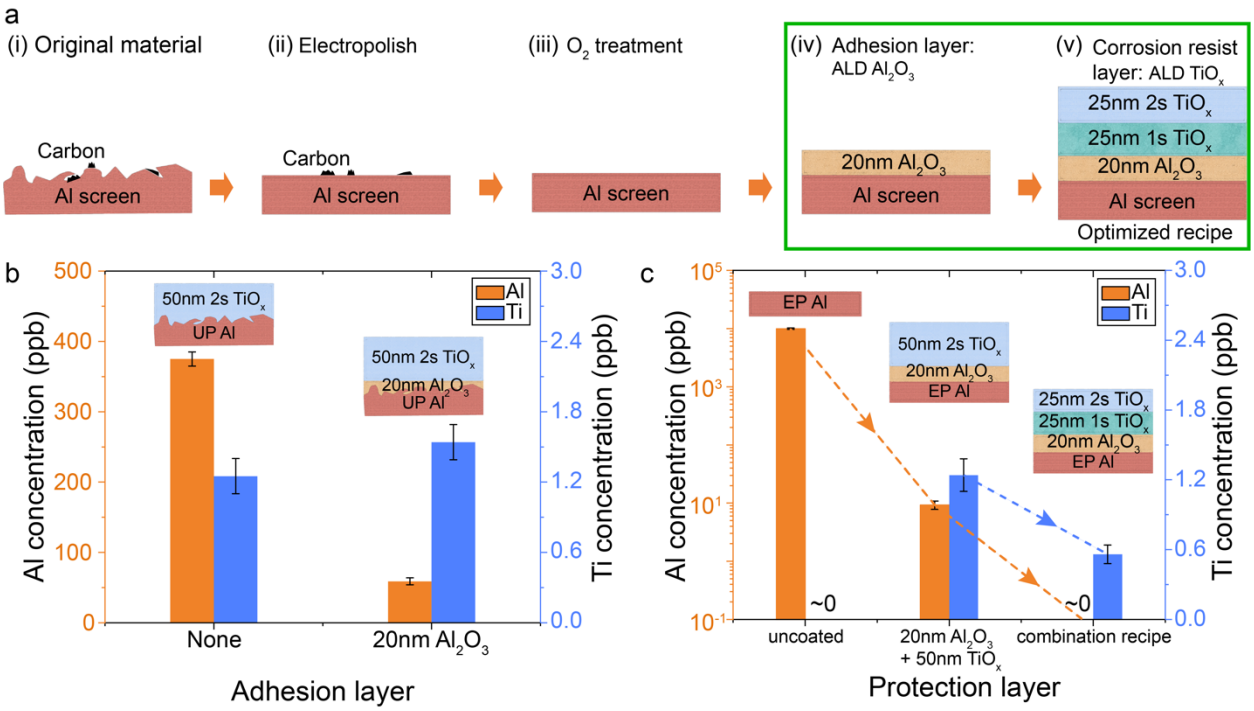


Figure 3.4 Characterization of the influence of adhesion and protection layers on corrosion resistance of Aluminum screens (a) Investigating the corrosion optimized layers. The concentrations of Al^{3+} and Ti^{4+}, as determined after PS testing by ICP-MS, for **(b)** 50 nm TiO_x-coated *UP* Al screen, without (*left*) and with (*right*) a 20 nm Al_2O_3 adhesion layer, showing substantial reduction of the Al substrate corrosion, and (c) uncoated (*left*), 20 nm Al_2O_3 + 50 nm TiO_x-coated (*middle*), 20 nm Al_2O_3 + 50 nm bilayer TiO_x-coated (*right*) *EP* Al screens. The optimized coating layers on the *right* side of **(c)** demonstrate significantly improved corrosion resistance.

Following the deposition of the ALD Al_2O_3 adhesion layer, a bilayer TiO_x coating composed of a 25 nm short purge (1 s) followed by a 25 nm long purge (2 s) ALD layer, was deposited. While long purge ALD promotes conformal film growth through self-limiting surface reactions[42], short purge ALD introduces precursor overlap resulting in a mixed gas-phase chemical vapor deposition (CVD) and surface ALD regime[43,44] (see **Fig. S3.8a** of *the Supporting Information*). AFM was used to confirm the distinct morphologies for both the layers, where it was seen that long purge ALD TiO_x yields a uniform film, while the short purge ALD TiO_x exhibited particle formation indicative of gas-phase CVD (see **Fig. S3.8b** of *the Supporting*

Information). It was also observed that while using long purge times for ALD TiO_x was sufficient for superior corrosion protection on smooth, *e.g.* mechanically polished (MP), Al 1100 substrates, ALD TiO_x synthesized using short purge times was more effective on the rougher Al screen surfaces – with respect to the Al dissolution. (**Figs. S3.9a** of *the Supporting Information*). The short purge ALD is better for rough surface here because we have some overlap structures on Al screen sample with high aspect ratio that long purge ALD is not able to penetrate in, while the short purge ALD with gas phase CVD provide particle precipitation on those overlap texture to form a seed layer for the subsequent coating. Additionally, long purge ALD TiO_x consistently exhibited a lower dissolution rate across both MP Al 1100 and Al screen samples (**Fig. S3.9b** of *the supporting information*). Consequently, a bilayer TiO_x coating procedure was implemented on the Al screens to leverage the respective advantages of *both* short and long purge time ALD, for maximal corrosion resistance of both the Al substrate as well as the ALD protection layer. A summary of the benefits of each optimized process, including surface pretreatments and ALD protection layers, along with their contributions to the improvement of corrosion resistance for the aluminum flow field, is provided in **Table S3.1** of *the Supporting Information*.

The results presented in **Fig. 3.4c** demonstrate that the combination of optimal surface pretreatment processes (plasma treatment on both sides of an *EP* substrate in addition to oxygen gas annealing) and an adhesion layer of ALD Al_2O_3 significantly improves the corrosion resistance of the Al screens. The Al^{3+} concentration, detected via ICP-MS, after the PS testing was reduced by three orders of magnitude, demonstrating notable enhancement in corrosion resistance. The subsequent usage of a bilayer ALD TiO_x further mitigates Al corrosion to ~ 0 ppb, *i.e.,* below the detection limit of 0.3 ng L^{-1} of the instrument[34] and a two-fold reduction in the detected Ti^{4+}. The

corrosion rate (*C.R.*) of the ALD TiO_x layer, was then estimated to be ~7 nm $year^{-1}$ based on the relation:

$$C.R. = \frac{[C_{Ti}]V_{sol} \cdot 24\ hr/day \cdot 365\ day/year}{\rho_x A t} \qquad (4.2)$$

Here, C_{Ti} is the Ti^{4+} concentration as recorded by ICP-MS, V_{sol} is the volume of the test solution (~80 mL), ρ_x is the density of TiO_x (~4.23 g cm^{-3}), A is the sampling area (~2.5 cm^2), and t is the testing time (~50 hours), assuming a constant dissolution rate throughout the PS testing. Based on these findings, a 50 nm thick corrosion-resistant ALD TiO_x layer may be projected as sufficient to provide protection of Al substrates, assuming a typical operational lifetime of 60,000 hours for water electrolyzers[30].

3.6 Electrochemical study for uncoated and optimal recipe coated Al screens

Electrochemical testing was used to understand the differences in corrosion mechanisms of the coated and uncoated Al screen substrates. Four orders of magnitude lower current density (*J*) was recorded for an Al screen coated with the optimized recipe, mainly attributed to the enhanced corrosion resistance as indicated in the previous section, compared to the uncoated Al screen: **Fig. 5(a)**.

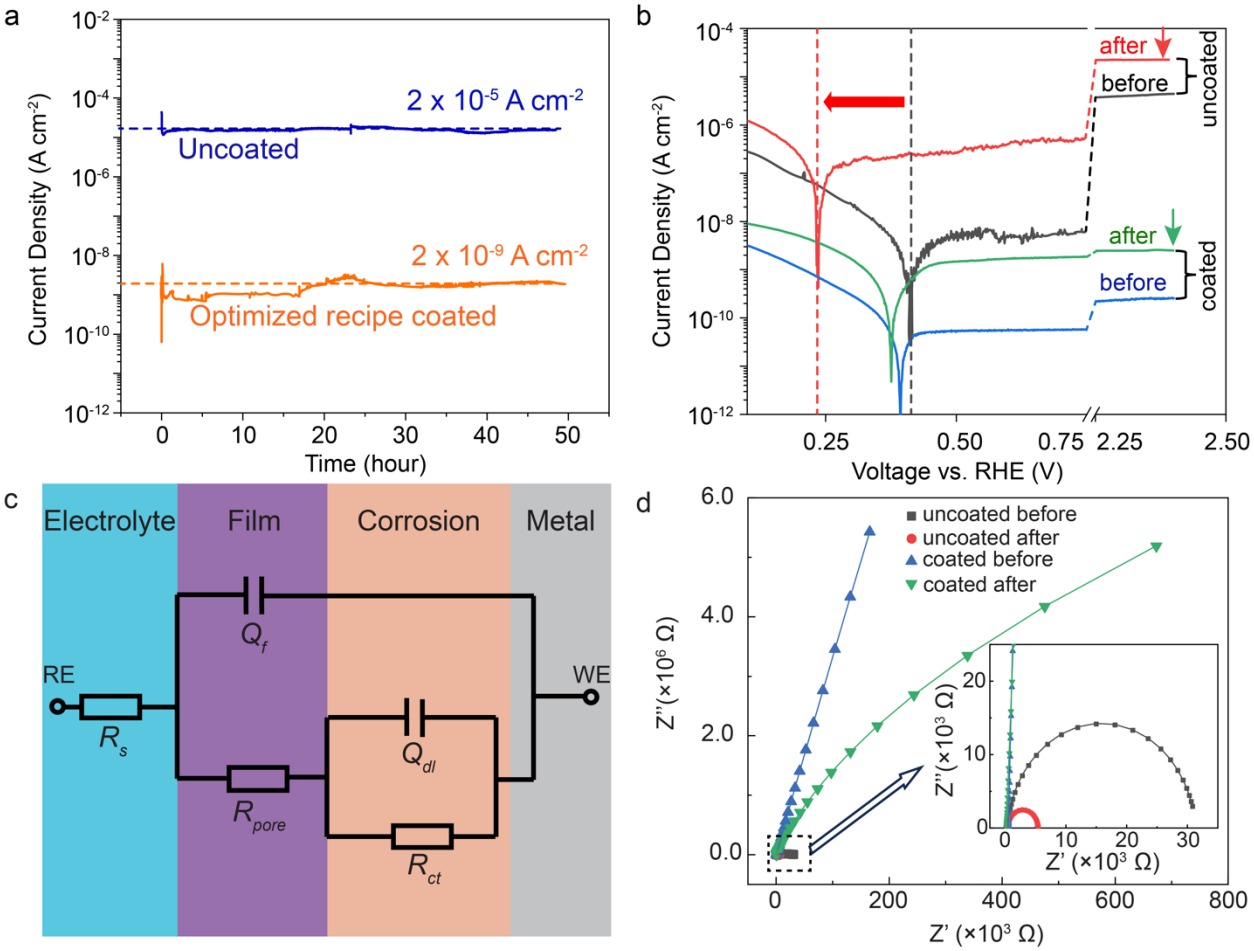


Figure 3.5 Electrochemical characterization contrasting the behavior of uncoated and optimally coated Al screens (a) The variation of current density (J) with time for uncoated and coated Al screens, over a potentiostatic (PS) test (in pH 3 H_2SO_4 at 2.4 V *vs.* RHE). The lower J for the optimally coated sample indicates four orders of magnitude enhanced corrosion resistance. **(b)** Polarization curves *before* and *after* PS testing. A more stable E_{corr} coupled with lower J was observed for the coated samples. **(c)** A plausible equivalent circuit used for the data fit from electrochemical impedance spectroscopy (EIS). The background resistance of the electrolyte (R_s), the resistance related to the porosity in the film (R_{pore}), along with the capacitive characteristics, at the coating – test solution interface, defined in terms of a constant phase element (CPE) for the film and double-layer characteristics - represented by Q_f and Q_{dl}, respectively, are indicated. **(d)** Nyquist plot for the uncoated and coated Al screens, measured at 2.4 V *vs.* RHE in pH 3 H_2SO_4 before and after the PS testing (1 MHz to 0.2 Hz). A higher impedance (Z) measured for the coated sample indicates improved corrosion resistance.

J approaches a steady state value of ~ 2 nA cm^{-2} (= J_o) during the PS testing for the optimally coated samples, implying that the *C.R.* of the ALD protection layer would remain constant over the electrolyzer lifetime, assuming no additional degradation takes place.

Potentiodynamic (PD) tests were performed both before and after the PS testing, with the related polarization curves[45] shown in **Fig. 3.5(b)**. The J (at 2.4 V *vs*. the RHE) obtained from the polarization curve after PS testing corresponds to the J_o observed in the PS testing. It is noted that the jump in the J at ~1.6 V (vs. RHE) corresponds to the onset of oxygen evolution. Tafel analysis[46] of the polarization curve was used to estimate the corrosion potential (E_{corr}), corrosion current density (J_{corr}), and polarization resistance (R_p). The relevant Tafel fitting parameters are summarized in **Table 3.1**. A two orders of magnitude reduction in the J_{corr} of the optimally coated Al screens, compared to the uncoated Al screen, observed both before and after the PS testing, is indicative of enhanced (and maintained) corrosion resistance. It was observed that the E_{corr} of the uncoated sample shifted to a more negative value after the PS testing, suggestive of dissolution of the native oxide layer into the acid solution, further exposing the Al substrate over time. Two orders of magnitude increase in the R_p (**Table 3.1**), through the use of the coatings, further supports the improved corrosion resistance provided by the ALD layers.

Table 3.1 Tafel fitting parameters for the uncoated and optimally coated Al screens, both before and after the potentiostatic test. The coated sample exhibits an order of magnitude higher polarization resistance compared to the uncoated sample, indicating significantly enhanced corrosion resistance.

Sample	J_{corr} **(nA cm^{-2})**	E_{corr} **(mV)**	R_p **(Ω cm^2)**
Uncoated (before PS)	3.7	427	1.8×10^7
Uncoated (after PS)	4.3×10^2	235	3.6×10^5
coated (before PS)	9.6×10^{-2}	393	1.2×10^9
coated (after PS)	2.3	398	8.6×10^7

Electrochemical impedance spectroscopy (EIS) measurements were performed at 2.4 V (*vs.* RHE) before and after the potentiostatic (PS) testing, with an aim of further understanding typical electrochemical corrosion related parameters that may be relevant to water electrolyzer[14–16] operation. A well-established equivalent electrical circuit model for corrosion behavior[47,48], as shown in **Fig. 3.5 (c)**, was employed to fit the measured EIS data. The model incorporates the background resistance of the electrolyte (R_s), the resistance related to the porosity in the film (R_{pore}), along with the capacitive characteristics defined in terms of a constant phase element (CPE). The CPE attributes for the film and double-layer characteristics are represented by Q_f and Q_{dl}, , and described through the impedance definition[49]:

$$Z_{CPE} = \frac{1}{Q(j\omega)^{\alpha}} \qquad (4.3)$$

Here, Q is the nominal capacitance, and α represents the exponent related to the CPE characteristic, *e.g.,* $\alpha = 1$ for an ideal capacitor, and $\alpha = 0.5$, when the charge storage is determined by purely diffusional characteristics. Additionally, the charge transfer resistance R_{ct}, related to chemical reactions such as film corrosion and oxygen evolution at the film-electrolyte interface, was also estimated from the fits to the EIS data: **Fig. 3.5(d)**. A further magnification, at high frequency, indicating the R_s and R_{pore}, is shown in **Fig. S3.10** of the *Supporting Information*. The EIS fitting parameters, derived from the equivalent circuit model, are summarized in **Table 3.2**.

Table 3.2 The obtained fits of the electrolyte resistance (R_s), porosity related resistance (R_{pore}), and the constant phase element (CPE) related to the film (Q_f) and double-layer characteristics (Q_{dl}) and associated exponents (α_f and α_{dl}) estimated from the equivalent circuit model related to the EIS spectrum of **Fig. 5(d)** for uncoated and optimally coated Al screen at 2.4 V (*vs.* RHE) in pH 3 H_2SO_4 *before* and *after* PS testing. A substantially increased R_{ct} , when the optimized coatings are used, clearly indicates enhanced corrosion resistance of the Al screen.

Sample	R_s (Ω cm^2)	R_{pore} (Ω cm^2)	Q_f (Ω^{-1} cm^{-2}s^a)	α_f	Q_{dl} (Ω^{-1} cm^{-2}s^a)	α_{dl}	R_{ct} (Ω cm^2)
Uncoated before	68	400	2.3×10^{-8}	0.69	2.3×10^{-6}	0.95	3.1×10^{4}
Uncoated after	102	440	2.0×10^{-7}	0.54	2.7×10^{-6}	1.00	5.0×10^{3}
coated before	46	560	1.1×10^{-9}	0.84	1.5×10^{-7}	0.98	6.0×10^{9}
coated after	94	540	5.8×10^{-9}	0.78	1.5×10^{-7}	0.97	6.8×10^{7}

From **Table 3.2,** an increase in R_s was observed for both the optimal recipe-coated and uncoated Al screens *after* the PS testing, which may be attributed to the formation of microbubbles on the surface during oxygen evolution, yielding an effective decrease in the electroactive surface area. A higher R_{pore} estimated for the coated Al screen suggests a lower porosity of the ALD protection layer relative to the uncoated Al screen (with porous and relatively higher surface area native oxide). While the Q_f is small and relatively constant for the coated samples, a larger Q_f was estimated for the uncoated Al screen. Further, the order of magnitude increase subsequent to PS testing implies the inherent charge instability in the uncoated samples. Diffusional limitations to charge storage, relevant to the greater porosity in the uncoated samples, is indicated by an α_f close to 0.5. Alternately, the α_f is closer to unity in the conformal, relatively porosity free coated samples. It is noted that the α_{dl} is generally close to unity indicating that the double layer attributes

do not differ significantly, between the coated and uncoated samples. The contrast between the Q_{dl} is also less significant between the coated and uncoated samples, with a smaller value in the former case, which may be attributed to the reduced surface area provided by the conformal and uniform ALD layers compared to the non-uniformity on the uncoated Al screen. Notably, orders of magnitude higher R_{ct} were observed for the optimal recipe-coated Al screen, compared to the uncoated Al screen, indicating substantially reduced corrosion currents, and improvement in corrosion resistance. The four orders of magnitude difference in R_{ct} is consistent with the J_o contrast noted in **Fig. 3.5(a)**.

3.7 ALD penetration ability and distribution uniformity study

While the beneficial use of adhesion and corrosion protection layers on Al screens to reduce corrosion has been demonstrated, the full effectiveness of ALD in complex geometries as shown in **Fig. 3.1** is yet unclear. To validate the feasibility of applying optimized ALD films to several flow field related layers in GDLs, the permeation through the PTL of the GDL was studied. **Fig. 3.6a(i)** shows an optical image of a 40 nm ALD TiO_x-coated GDL, composed of a PTL, Al screen, and a back plate. It was observed that the TiO_x coating uniformly covers the Al screen and back plate through the PTL. The small uncoated region, on the periphery, is due to the aluminum foil placed around the GDL pack to ensure that precursor gas flow only occurs through the top to the bottom of the stack. **Fig. 3.6a(ii)** indicates a consistent Ti atomic percentage of 3.8 ± 0.2% , determined by EDS, at different locations of the Al screen, demonstrating the stoichiometric uniformity of the coating. Similarly, **Fig. 3.6 (b)** shows a 50 nm ALD Al_2O_3-coated GDL pack, consisting only of a PTL and a back plate, also confirming the penetration of the ALD Al_2O_3 that was used as an adhesion layer through the PTL, with good uniformity. The relatively low atomic

percentage is attributed to the high-energy electron beam (10 keV) employed to ensure the collection of the Ti Kα signal, which resulted in increased signal contribution from the substrate.

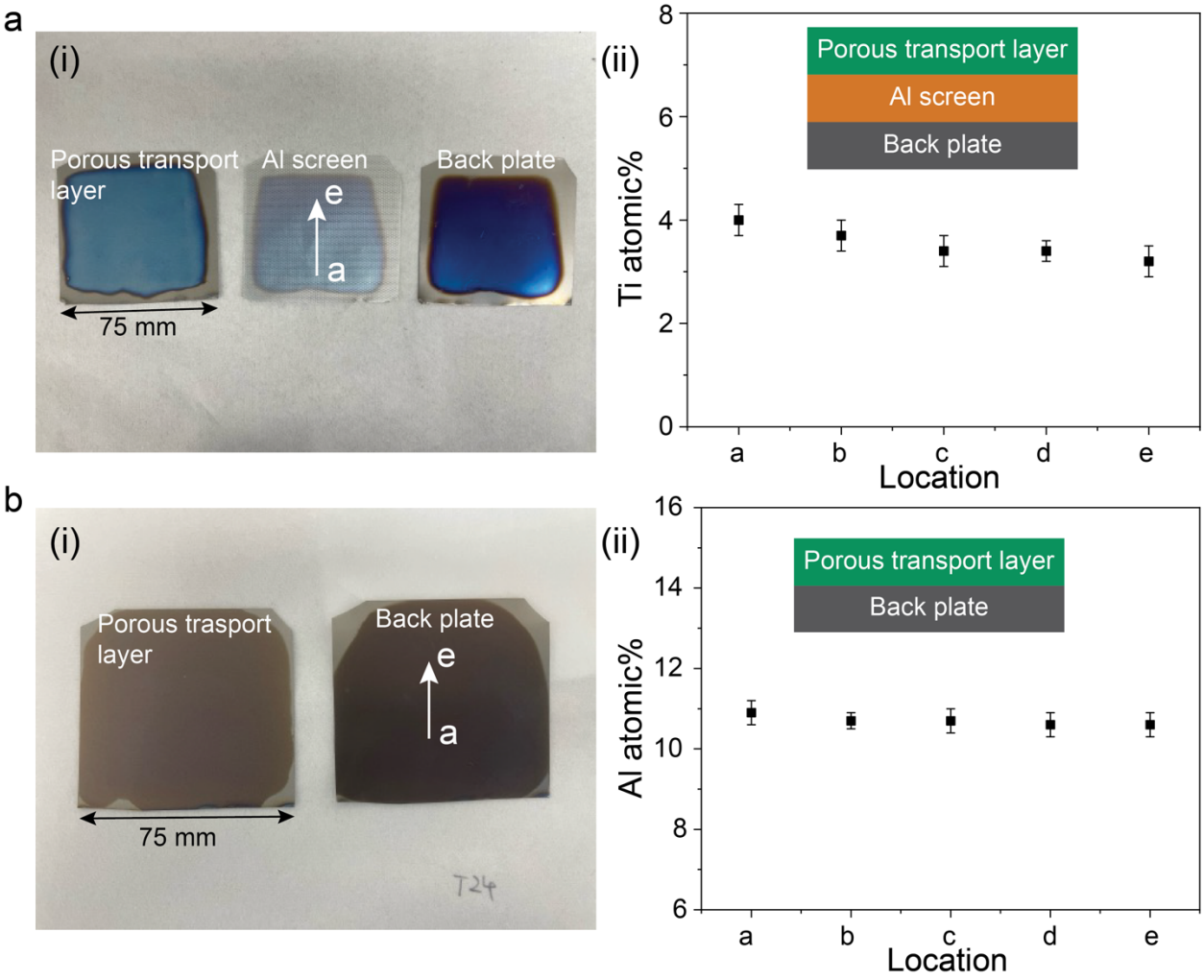
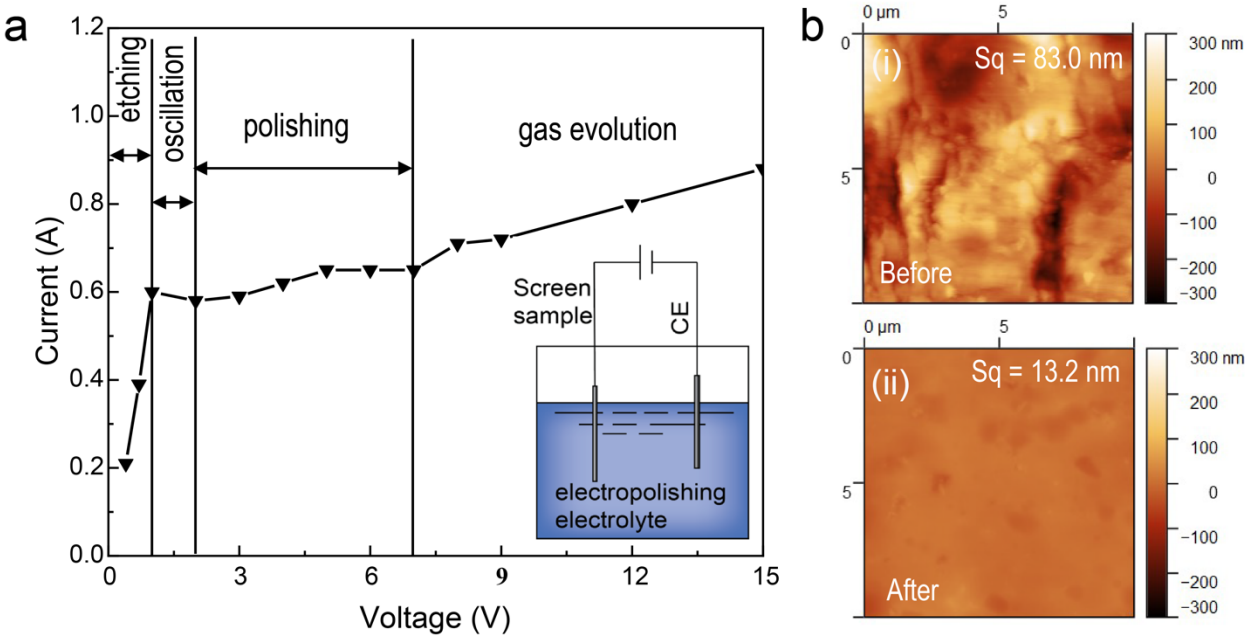


Figure 3.6 Evidence of ALD permeation and uniformity of stoichiometry through successive layers, in the flow field. (a) The ALD TiO_x was coated through successive layers, as seen in the optical images, starting from the top porous transport layer (PTL), middle Al screen, and the solid Ti (Grade 2) back plate, with uniform Ti stoichiometry, **(b)** ALD Al_2O_3 was coated through successive layers, starting from the top PTL and the backplate, with uniform Al stoichiometry. The locations of the EDS for the stoichiometry determination are indicated as (a) → (e).

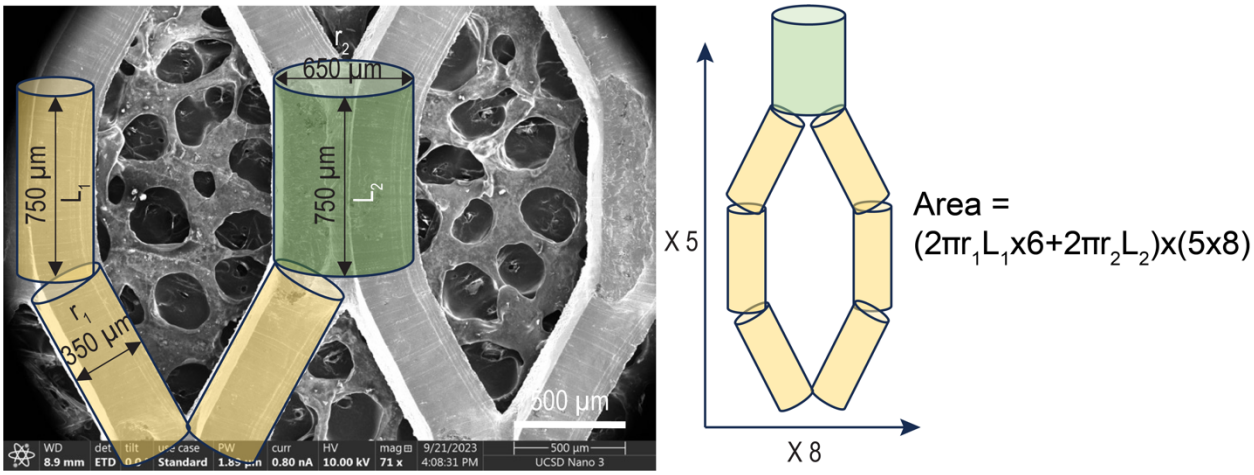
3.8 Conclusion

This study demonstrates that aluminum could be used instead of titanium in PEM water electrolyzer components, such as those used in the flow field of a gas distribution layer, with appropriate ALD coatings. Detailed structural, elemental, and electrochemical characterization was utilized for correlating the corrosion characteristics to practical electrolyzer working conditions, *i.e.,* low pH and high applied voltages in both potentiostatic and potentiodynamic conditions. Excellent and robust corrosion resistance (~ 7 nm $year^{-1}$ for ALD TiO_x) was obtained through carefully optimized (i) polishing, (ii) surface contaminant removal, (iii) introduction of an Al_2O_3 adhesion layer to prevent pinhole formation, followed by two ALD TiO_x corrosion protection layers with (iv) short purge, and (v) long purge times. It is estimated that a 50 nm thick ALD coating would be adequate to withstand a typical water electrolyzer lifespan of ~ 60,000 hours[30]. It was also shown that the ALD may be used for complex geometries, with successive layers of differing porosities, as relevant for practical electrolyzer devices. Our work paves the way for cost-effective alternatives to presently used materials and would help in the proliferation of green hydrogen production, with alternate applications to other technologies, including aerospace[50], railway infrastructure[51], and the automotive sector[52].

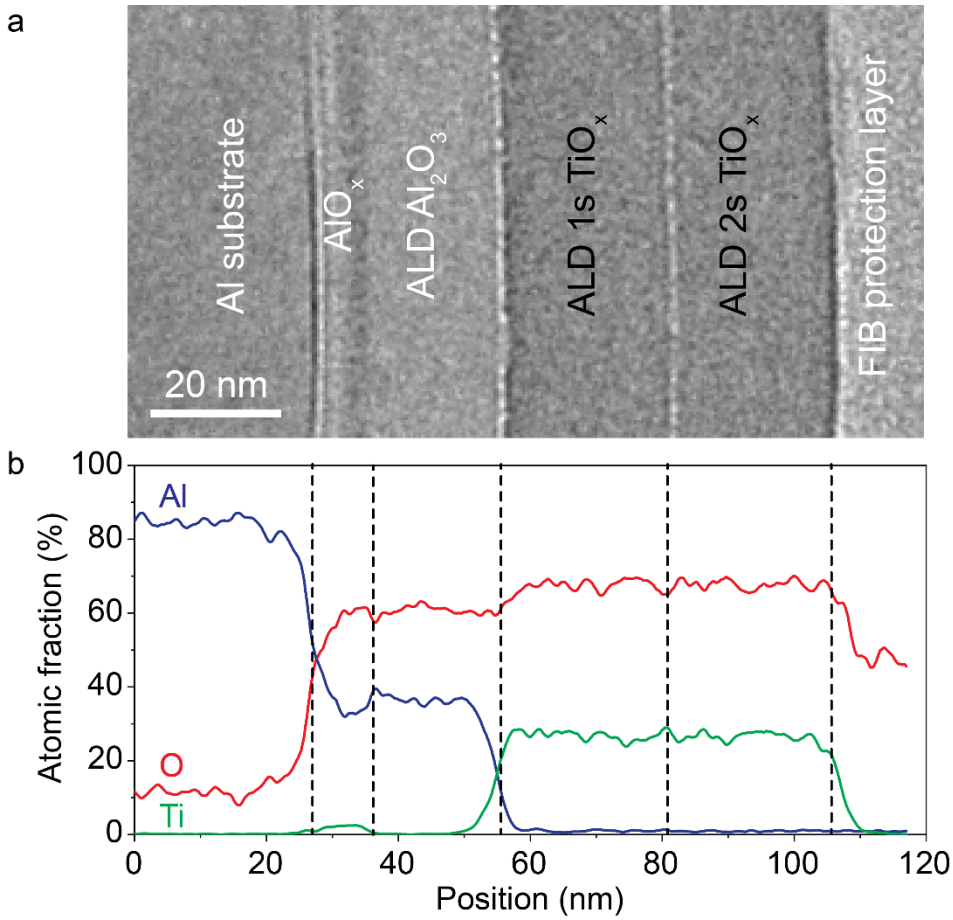
3.9 Supporting information



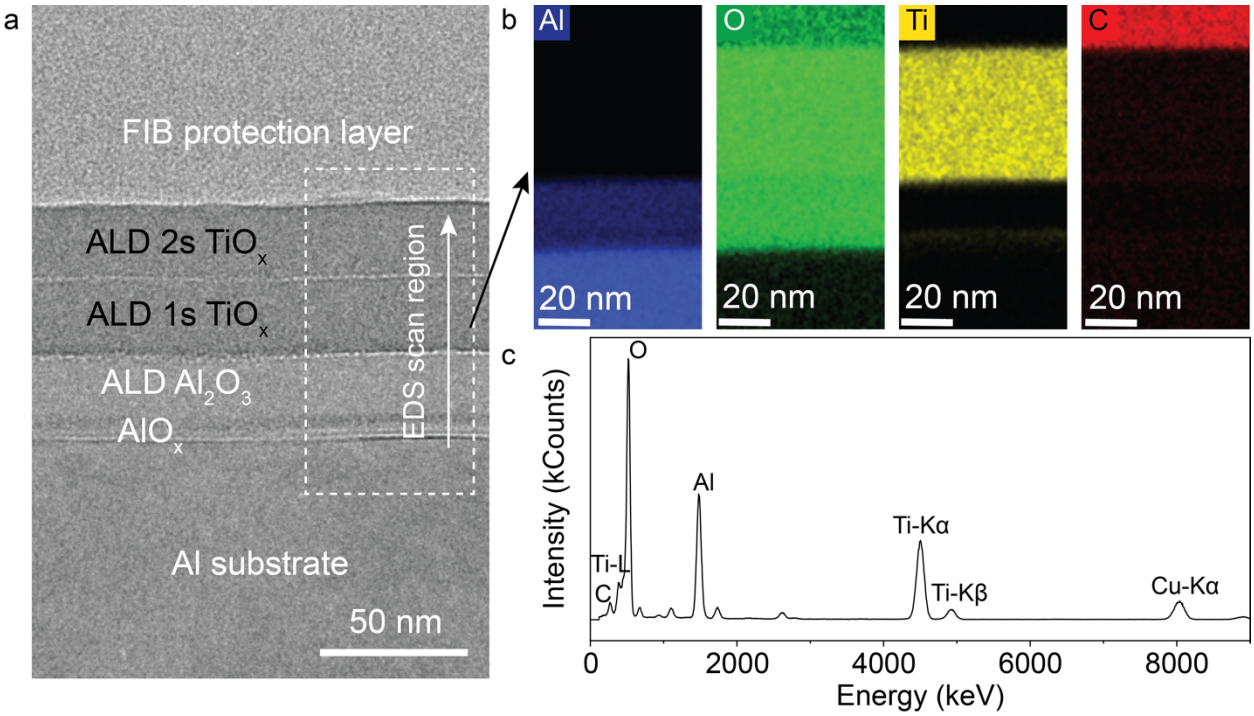
Supplemental Figure 3.1 (a) Determination of Electrical current (*I*) – voltage (*V*) characteristics for optimal electropolishing (*EP*) of meshed aluminum (Al), used as screens in the flow field of the gas diffusion layer (GDL) of water electrolyzers. The Al sample was *EP* in a two electrodes setup, and the *I-V* curve exhibited four stages corresponding to, (i) etching, (ii) oscillation, (iii) polishing, and (iv) gas evolution. 5V was used for the *EP* corresponding to the plateau of the curve, **(b)** Atomic Force Microscopy (AFM) images of the top surface of the Al screen (i) before, and (ii) after the *EP*, indicating a six-fold reduction in the *RMS* surface roughness from ~ 83 nm to ~ 13 nm, subsequent to *EP*.



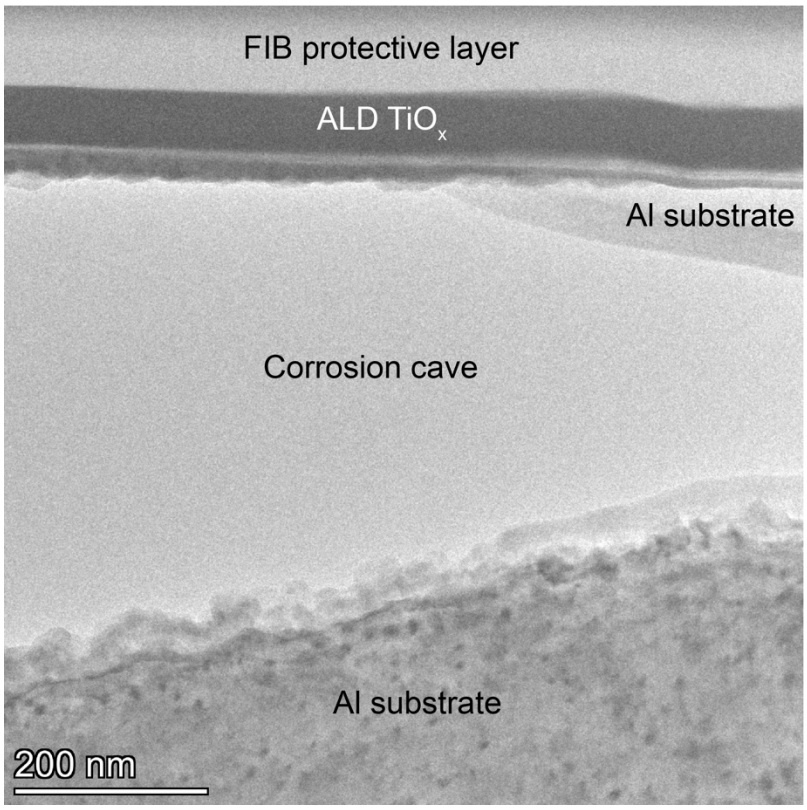
Supplemental Figure 3.2 Surface area estimation for Al screen sample. The surface area was estimated through modeling the Al screen as consisting of forty units arranged in an 8 × 5 grid, comprising six small and one large cylinder/s.



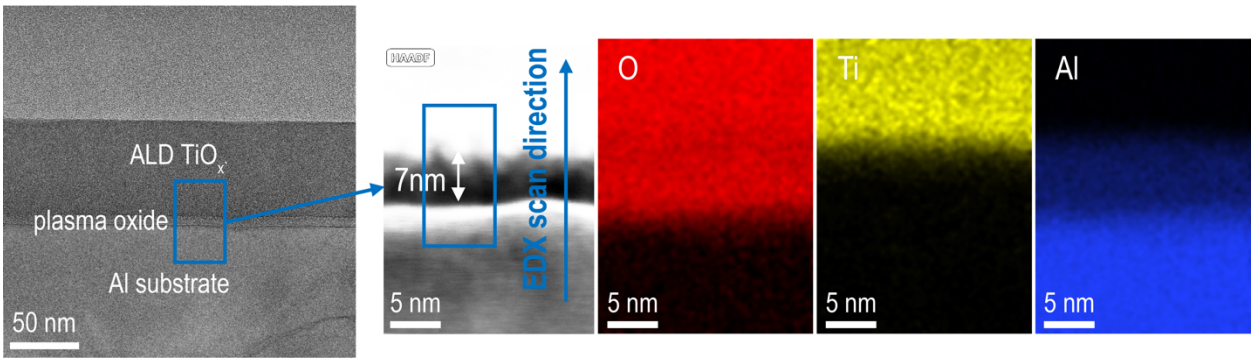
Supplemental Figure 3.3 Cross section transmission electron microscopy (TEM) characterization of the influence of surface treatment and ALD layers on Al screens (a) TEM bright field image of the AlO_x interfacial layer, Al_2O_3 adhesion layer, and TiO_x protection layers on the *EP* Al screens. **(b)** Energy-dispersive x-ray spectroscopy (EDS) imaging indicating the distribution of elements. Successive layers appear distinct with white borders of presumably lower density material, due to process interruption prior to the deposition of the next layer. A similar phenomenon has been reported in several previous studies involving cross-sectional TEM analysis of multilayer thin films[53,54].



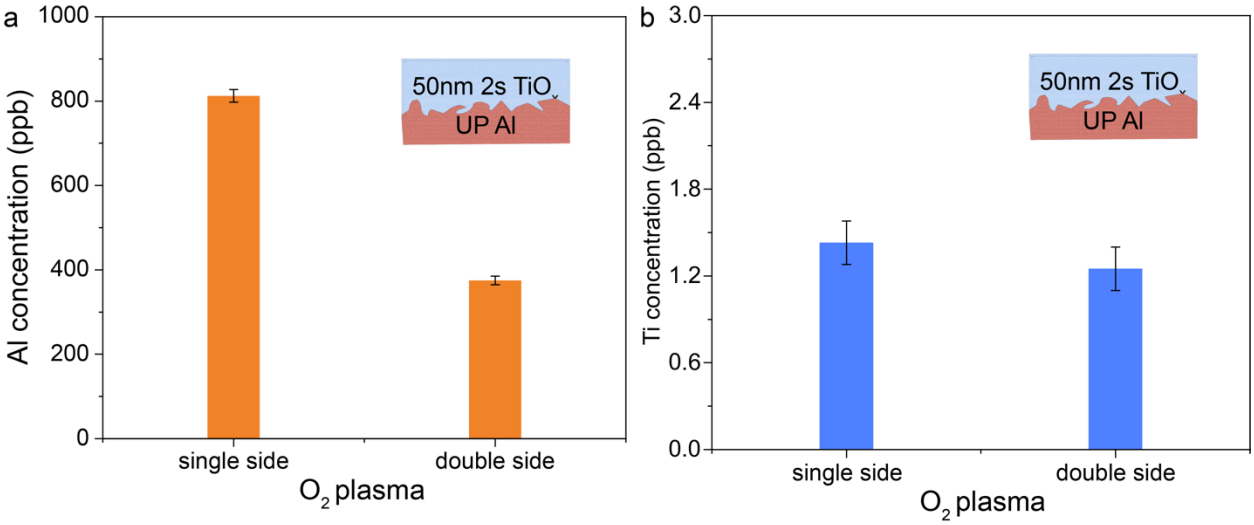
Supplemental Figure 3.4 Cross section transmission electron microscopy (TEM) of Al substrates, with the optimized surface treatment and subsequent coating (a) TEM bright field image indicating the AlO_x interfacial layer (from the surface oxygen treatment), the Al_2O_3 adhesion layer, and TiO_x protection layers on the *EP* Al screens. **(b)** Energy-dispersive x-ray spectroscopy (EDS) imaging indicating the distribution of elements. **(c)** x-ray spectra of the EDS mapping region, indicating Ti, Al, and O; the spurious Cu peak is from the TEM grid sample holder.



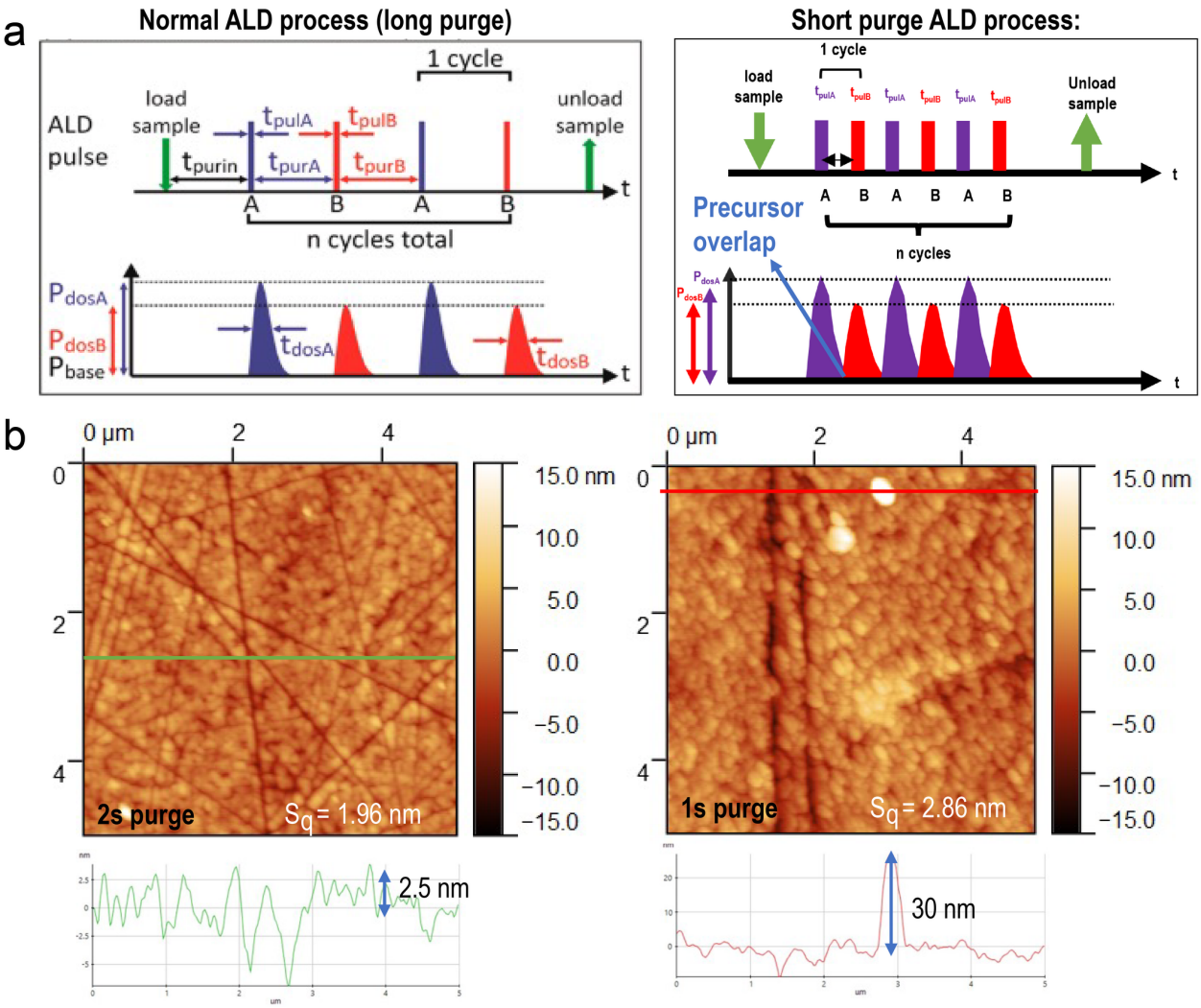
Supplemental Figure 3.5 TEM characterization of corrosion in Al screen due to pinholes in the ALD protection layer. A large corrosion cavity(”cave”) was observed beneath the ALD TiO_x layer, indicating the susceptibility of the Al substrate to the acid solution. The formation of even a small pinhole in the ALD protection layer can then result in significant corrosion of the underlying Al.



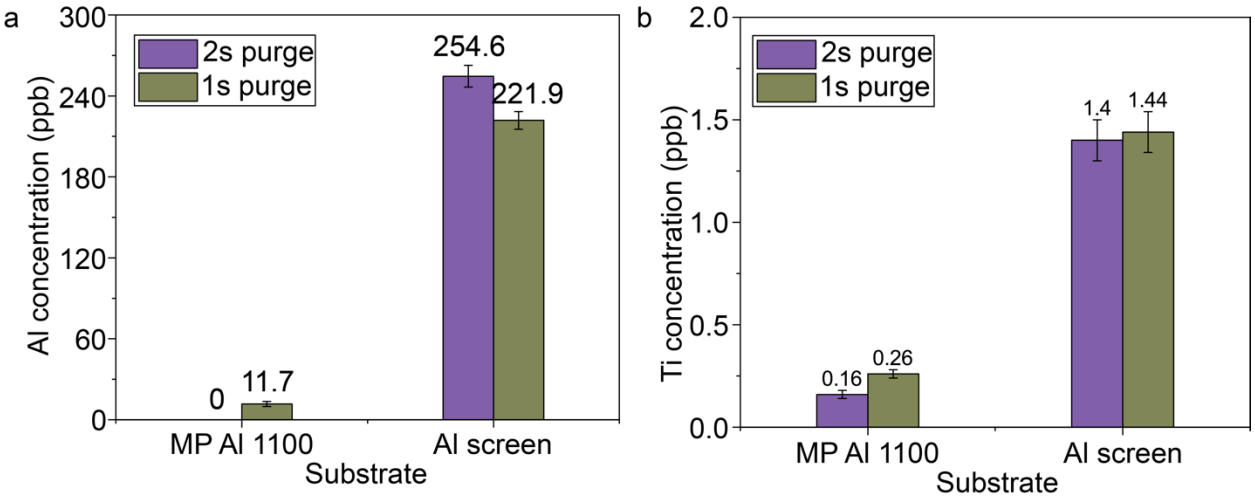
Supplemental Figure 3.6 TEM and EDS characterization of oxide formed after oxygen plasma exposure of the substrate. A thin uniform layer of oxide was formed following oxygen plasma treatment on Al screen, as confirmed by the TEM image and corresponding region-specific energy dispersive spectroscopy (EDS) mapping.



Supplemental Figure 3.7 Determination of the Al^{3+} and Ti^{4+} concentration through ICP-MS analysis for ALD TiO_x coated Al screen subject to oxygen plasma treatment on one/single side and double/both sides after PS testing. The Al corrosion was then deduced to be much reduced when *both* sides of the screen were exposed to the plasma. The surface contaminants, such as hydrocarbons, are more effectively removed and Al corrosion is diminished, by preventing pinholes in the succeeding ALD layers. The **Ti^{4+}** concentration was less affected by the plasma treatment, consistent with the aspect of the robustness of the TiO_x layer.



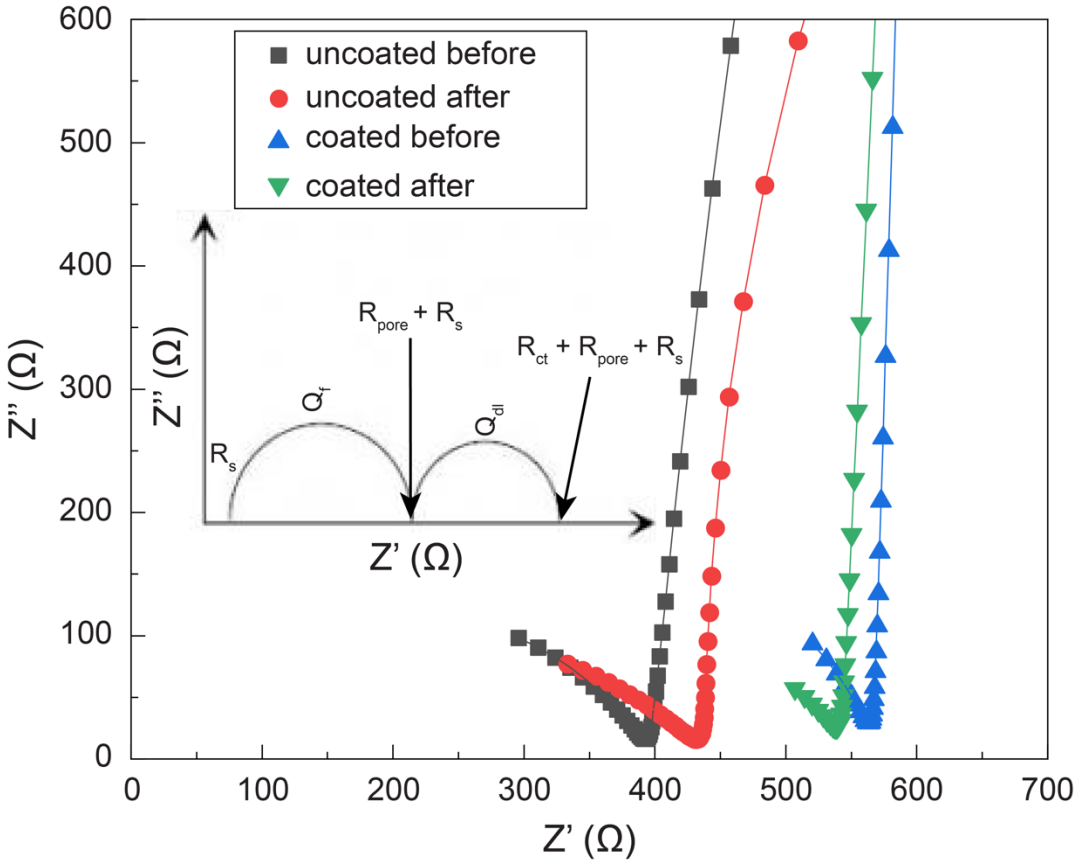
Supplemental Figure 3.8 Schematic of processes related to the long purge (2s) and short purge (1s) ALD TiO_x. (a) (*left*) The long purge cycle ALD process with self-limiting reactions, where all precursor residuals are purged after each cycle, and (*right*) the short purge ALD process, where precursor overlap between cycles leads to a combination of surface ALD as well as gas-phase CVD[55,56]. **(b)** AFM images of the surface of 50 nm thick long purge ALD TiO_x (*left*) and short purge ALD TiO_x (*right*) films coated on flat aluminum (mechanically polished Al 1100). The long purge ALD TiO_x forms a conformal film, whereas the short purge ALD TiO_x generates small particles, indicative of gas-phase CVD, on the Al substrate. (Both short purge and long purge ALD TiO_x were deposited at 120°C with pulse length of 150 ms $TiCl_4$ and 50 ms H_2O)



Supplemental Figure 3.9 Determination of the (a) Al^{3+} and (b) Ti^{4+} concentration through ICP-MS analysis of 50 nm TiO_x synthesized by long purge (2 s) ALD and short purge (1 s) ALD TiO_x coated on flat Al (MP Al 1100) and Al screens, after the PS testing. While the Al and Ti loss are small for smooth/mechanically polished (MP) Al, the Al loss may be reduced by using a short purge (1 s) cycle in addition to the long purge (2 s) cycle). The long purge, providing a conformal coating offers better corrosion resistance for flat surfaces, while the short purge, combining gas-phase CVD with surface ALD, enhances corrosion resistance on rough surfaces, such as the Al screens, through preventing pinhole formation. In (b) a lower Ti^{4+} concentration for the long purge ALD TiO_x on both MP Al 1100 and Al screens indicates that the related TiO_x is more corrosion resistant to the acid solution, with a slightly lower dissolution rate compared to short purge ALD TiO_x.

Supplemental Table 3.1 Benefits of each optimized process, including surface treatment and ALD protection layer, along with the detailed contributions and improvements to the corrosion resistance of the aluminum flow field.

TREATMENT		CONTRIBUTION	IMPROVEMENT
SURFACE PRETREATMENT	EP	Reduce surface roughness	Reduced Al corrosion by ~30×
	O_2 plasma	Remove surface contamination, generate uniform plasma oxide	Reduced Al corrosion by ~4×
	O_2 annealing	Remove surface contamination, generate uniform thermal oxide	Reduced Al corrosion by ~20×
ALD PROTECTION LAYER	Al_2O_3	Improve interfacial adhesion	Reduced Al corrosion by ~6×
	Short purge TiO_x	Act as seed layer for subsequent coating to eliminate pinhole formation	Reduce Al corrosion to ~0 ppb level, reduce TiO_x corrosion by ~2×
	Long purge TiO_x	Corrosion resistant layer with low dissolution rate	



Supplemental Figure 3.10 EIS Nyquist plot for the high frequency (1250 Hz - 1MHz) region of uncoated and optimal recipe coated Al screens, measured at 2.4 V (*vs.* RHE) in pH3 H_2SO_4 before and after the PS testing. The obtained circuit parameters from the data are indicated in Table 2 , of the main text. A higher pore resistance (R_{pore}) for the Al screens coated with the optimal recipe compared to the uncoated Al screens, suggesting a reduction in porosity or an increase in the compactness of the ALD protection layer. Schematic of the EIS plot, indicating the R_s, R_{pore}, R_{ct}, Q_f, and Q_{dl}, is shown in the inset figure.

3.10 Acknowledgement

This work was partially conducted at the San Diego Nanotechnology Infrastructure (SDNI) of UCSD, a member of the National Nanotechnology Coordinated Infrastructure, supported by the National Science Foundation (Grant ECCS-2025752). The authors would like to thank Dr. Neal Arakawa of the Environmental and Complex Analysis Laboratory at UC San Diego for his assistance with the ICP-MS measurements. Additionally, the authors express their gratitude to

Yaneth Hernandez for her contributions to the development and interpretation of the corrosion tests and results.

Chapter 3, in full, is a reprint with permission from Kesong Wang, "TiO_x/Al_2O_3 laminate atomic layer deposited (ALD) films to enable corrosion protection of aluminum screens and porous components in water electrolyzers", manuscript submitted to *ACS Applied Materials & Interfaces*, by Kesong Wang, Adam Paxson, Thomas I. Valdez, Ahmet Gün Erlat, Ping-Che Lee, Andrew C. Kummel, Prabhakar R. Bandaru. The dissertation author was the primary researcher and author of this paper.

3.11 Reference

(1) Islam, A.; Islam, T.; Mahmud, H.; Raihan, O.; Islam, Md. S.; Marwani, H. M.; Rahman, M. M.; Asiri, A. M.; Hasan, Md. M.; Hasan, Md. N.; Salman, Md. S.; Kubra, K. T.; Shenashen, M. A.; Sheikh, Md. C.; Awual, Md. R. Accelerating the Green Hydrogen Revolution: A Comprehensive Analysis of Technological Advancements and Policy Interventions. *Int J Hydrogen Energy* **2024**, *67*, 458–486. https://doi.org/10.1016/j.ijhydene.2024.04.142.

(2) Sebbagh, T.; Şahin, M. E.; Beldjaatit, C. Green Hydrogen Revolution for a Sustainable Energy Future. *Clean Technol Environ Policy* **2024**, *26* (12), 4017–4040. https://doi.org/10.1007/s10098-024-02995-9.

(3) Hassan, Q.; Algburi, S.; Sameen, A. Z.; Salman, H. M.; Jaszczur, M. Green Hydrogen: A Pathway to a Sustainable Energy Future. *Int J Hydrogen Energy* **2024**, *50*, 310–333. https://doi.org/10.1016/j.ijhydene.2023.08.321.

(4) Salvi, B. L.; Subramanian, K. A. Sustainable Development of Road Transportation Sector Using Hydrogen Energy System. *Renewable and Sustainable Energy Reviews* **2015**, *51*, 1132–1155. https://doi.org/10.1016/j.rser.2015.07.030.

(5) Yue, M.; Lambert, H.; Pahon, E.; Roche, R.; Jemei, S.; Hissel, D. Hydrogen Energy Systems: A Critical Review of Technologies, Applications, Trends and Challenges. *Renewable and Sustainable Energy Reviews* **2021**, *146*, 111180. https://doi.org/10.1016/j.rser.2021.111180.

(6) Zhang, F.; Zhao, P.; Niu, M.; Maddy, J. The Survey of Key Technologies in Hydrogen Energy Storage. *Int J Hydrogen Energy* **2016**, *41* (33), 14535–14552. https://doi.org/10.1016/j.ijhydene.2016.05.293.

(7) Nasser, M.; Megahed, T. F.; Ookawara, S.; Hassan, H. A Review of Water Electrolysis–Based Systems for Hydrogen Production Using Hybrid/Solar/Wind Energy Systems. *Environmental Science and Pollution Research* **2022**, *29* (58), 86994–87018. https://doi.org/10.1007/s11356-022-23323-y.

(8) Nnabuife, S. G.; Hamzat, A. K.; Whidborne, J.; Kuang, B.; Jenkins, K. W. Integration of Renewable Energy Sources in Tandem with Electrolysis: A Technology Review for Green Hydrogen Production. *Int J Hydrogen Energy* **2024**. https://doi.org/10.1016/j.ijhydene.2024.06.342.

(9) Alkhaldi, S.; Aziz, M.; Amrite, A.; Prasad, A. K. Parametric Study of PEM Water Electrolyzer Performance. *J Appl Electrochem* **2025**, *55* (2), 327–343. https://doi.org/10.1007/s10800-024-02187-9.

(10) Park, S.; Lee, J.-W.; Popov, B. N. A Review of Gas Diffusion Layer in PEM Fuel Cells: Materials and Designs. *Int J Hydrogen Energy* **2012**, *37* (7), 5850–5865. https://doi.org/10.1016/j.ijhydene.2011.12.148.

(11) Majlan, E. H.; Rohendi, D.; Daud, W. R. W.; Husaini, T.; Haque, M. A. Electrode for Proton Exchange Membrane Fuel Cells: A Review. *Renewable and Sustainable Energy Reviews* **2018**, *89*, 117–134. https://doi.org/10.1016/j.rser.2018.03.007.

(12) Tao, Y.; Wu, M.; Hu, M.; Xu, X.; Abdullah, M. I.; Shao, J.; Wang, H. High-performance Porous Transport Layers for Proton Exchange Membrane Water Electrolyzers. *SusMat* **2024**, *4* (4). https://doi.org/10.1002/sus2.230.

(13) Teuku, H.; Alshami, I.; Goh, J.; Masdar, M. S.; Loh, K. S. Review on Bipolar Plates for Low-temperature Polymer Electrolyte Membrane Water Electrolyzer. *Int J Energy Res* **2021**, *45* (15), 20583–20600. https://doi.org/10.1002/er.7182.

(14) Calcerrada, A. B.; de la Osa, A. R.; Llanos, J.; Dorado, F.; de Lucas-Consuegra, A. Hydrogen from Electrochemical Reforming of Ethanol Assisted by Sulfuric Acid Addition. *Appl Catal B* **2018**, *231*, 310–316. https://doi.org/10.1016/j.apcatb.2018.03.028.

(15) Hou, Y.; Lv, J.; Quan, W.; Lin, Y.; Hong, Z.; Huang, Y. Strategies for Electrochemically Sustainable H $_2$ Production in Acid. *Advanced Science* **2022**, *9* (7). https://doi.org/10.1002/advs.202104916.

(16) Nafeh, A. E. A. Hydrogen Production from a PV/PEM Electrolyzer System Using a Neural-network-based MPPT Algorithm. *International Journal of Numerical Modelling: Electronic Networks, Devices and Fields* **2011**, *24* (3), 282–297. https://doi.org/10.1002/jnm.778.

(17) Perks, C.; Mudd, G. Titanium, Zirconium Resources and Production: A State of the Art Literature Review. *Ore Geol Rev* **2019**, *107*, 629–646. https://doi.org/10.1016/j.oregeorev.2019.02.025.

(18) Sverdrup, H. U.; Sverdrup, A. E. An Assessment of the Global Supply, Recycling, Stocks in Use and Market Price for Titanium Using the WORLD7 Model. *Sustainable Horizons* **2023**, *7*, 100067. https://doi.org/10.1016/j.horiz.2023.100067.

(19) Jáquez-Muñoz, J. M.; Gaona-Tiburcio, C.; Mendez-Ramirez, C. T.; Carrera-Ramirez, M. G.; Baltazar-Zamora, M. A.; Santiago-Hurtado, G.; Lara-Banda, M.; Estupiñan-Lopez, F.; Nieves-Mendoza, D.; Almeraya-Calderon, F. Corrosion of Anodized Titanium Alloys. *Coatings* **2024**, *14* (7), 809. https://doi.org/10.3390/coatings14070809.

(20) Wang, S.-H.; Peng, J.; Lui, W.-B. Surface Modification and Development of Titanium Bipolar Plates for PEM Fuel Cells. *J Power Sources* **2006**, *160* (1), 485–489. https://doi.org/10.1016/j.jpowsour.2006.01.020.

(21) Jung, H.-Y.; Huang, S.-Y.; Ganesan, P.; Popov, B. N. Performance of Gold-Coated Titanium Bipolar Plates in Unitized Regenerative Fuel Cell Operation. *J Power Sources* **2009**, *194* (2), 972–975. https://doi.org/10.1016/j.jpowsour.2009.06.030.

(22) Hatch, J. E. *Aluminum Association. Aluminum: Properties and Physical Metallurgy*; ASM international, 1984.

(23) Zheng, X.; Han, C.; Lee, C.-S.; Yao, W.; Zhi, C.; Tang, Y. Materials Challenges for Aluminum Ion Based Aqueous Energy Storage Devices: Progress and Prospects. *Prog Mater Sci* **2024**, *143*, 101253. https://doi.org/10.1016/j.pmatsci.2024.101253.

(24) Low, H. C.; Lim, B. H.; Masdar, M. S.; Rosli, M. I. Understanding the Factors Influencing the Corrosion of Bipolar Plate to the Performance and Durability of Unitized Regenerative Proton Exchange Membrane Fuel Cell: A Review. *Int J Hydrogen Energy* **2024**, *57*, 420–430. https://doi.org/10.1016/j.ijhydene.2024.01.010.

(25) Zhao, Y.; Zhang, L.; Liu, J.; Adair, K.; Zhao, F.; Sun, Y.; Wu, T.; Bi, X.; Amine, K.; Lu, J.; Sun, X. Atomic/Molecular Layer Deposition for Energy Storage and Conversion. *Chem Soc Rev* **2021**, *50* (6), 3889–3956. https://doi.org/10.1039/D0CS00156B.

(26) Oviroh, P. O.; Akbarzadeh, R.; Pan, D.; Coetzee, R. A. M.; Jen, T.-C. New Development of Atomic Layer Deposition: Processes, Methods and Applications. *Sci Technol Adv Mater* **2019**, *20* (1), 465–496. https://doi.org/10.1080/14686996.2019.1599694.

(27) Awan, T. I.; Afsheen, S.; Kausar, S. Advanced Deposition Techniques. In *Thin Film Deposition Techniques*; Springer Nature Singapore: Singapore, 2025; pp 161–187. https://doi.org/10.1007/978-981-96-1364-9_6.

(28) Figueira, R. B. Hybrid Sol–Gel Coatings for Corrosion Mitigation: A Critical Review. *Polymers (Basel)* **2020**, *12* (3), 689. https://doi.org/10.3390/polym12030689.

(29) Wu, L.-K.; Wu, J.-J.; Wu, W.-Y.; Cao, F.-H.; Jiang, M.-Y. Sol–Gel-Based Coatings for Oxidation Protection of TiAl Alloys. *J Mater Sci* **2020**, *55* (15), 6330–6351. https://doi.org/10.1007/s10853-020-04466-0.

(30) Smolinka, T.; Bergmann, H.; Garche, J.; Kusnezoff, M. The History of Water Electrolysis from Its Beginnings to the Present. In *Electrochemical Power Sources: Fundamentals, Systems, and Applications*; Elsevier, 2022; pp 83–164. https://doi.org/10.1016/B978-0-12-819424-9.00010-0.

(31) Wang, K.; Paxson, A.; Valdez, T. I.; Erlat, A.; Lee, P.-C.; Yun, S.; Khajanji, P.; Zhang, Z.; Kummel, A. C.; Bandaru, P. Enhanced Corrosion Resistance in Aluminum-Based Electrolyzer Components via Stoichiometry Tuned Atomic Layer-Deposited TiO_x Films. *ACS Appl Mater Interfaces* **2024**, *16* (27), 35043–35052. https://doi.org/10.1021/acsami.4c05450.

(32) Chiappim, W.; Watanabe, M.; Dias, V.; Testoni, G.; Rangel, R.; Fraga, M.; Maciel, H.; dos Santos Filho, S.; Pessoa, R. MOS Capacitance Measurements for PEALD TiO2 Dielectric Films Grown under Different Conditions and the Impact of Al2O3 Partial-Monolayer Insertion. *Nanomaterials* **2020**, *10* (2), 338. https://doi.org/10.3390/nano10020338.

(33) Daubert, J. S.; Hill, G. T.; Gotsch, H. N.; Gremaud, A. P.; Ovental, J. S.; Williams, P. S.; Oldham, C. J.; Parsons, G. N. Corrosion Protection of Copper Using Al_2O_3, TiO_2, ZnO, HfO_2, and ZrO_2 Atomic Layer Deposition. *ACS Appl Mater Interfaces* **2017**, *9* (4), 4192–4201. https://doi.org/10.1021/acsami.6b13571.

(34) Vincent, T.; Hsu, J.; Wu, V.; Wills, J. *Routine determination of ultratrace elements in semiconductor grade nitric acid by the Thermo Scientific iCAP RQ ICP-MS*. thermofisher scientific website. https://www.thermofisher.com/order/catalog/product/BRE731416 (accessed 2024-02-23).

(35) Choi, J.-H.; Eun Kang, H.; Kim, D.-J.; Soo Yoon, Y. A Comprehensive Review of Stainless-Steel Bipolar Plate Coatings and Their Role in Mitigating Corrosion in Aggressive Proton-Exchange Membrane Fuel Cells Environments. *Chemical Engineering Journal* **2024**, *493*, 152662. https://doi.org/10.1016/j.cej.2024.152662.

(36) Liu, T.; Tao, Y.; Wang, Y.; Hu, M.; Zhang, Z.; Shao, J. Towards Cost-Effective and Durable Bipolar Plates for Proton Exchange Membrane Electrolyzers: A Review. *Fuel* **2024**, *368*, 131610. https://doi.org/10.1016/j.fuel.2024.131610.

(37) Hong, J.; Porter, D. W.; Sreenivasan, R.; McIntyre, P. C.; Bent, S. F. ALD Resist Formed by Vapor-Deposited Self-Assembled Monolayers. *Langmuir* **2007**, *23* (3), 1160–1165. https://doi.org/10.1021/la0606401.

(38) Yang, H.-C.; Xie, Y.; Chan, H.; Narayanan, B.; Chen, L.; Waldman, R. Z.; Sankaranarayanan, S. K. R. S.; Elam, J. W.; Darling, S. B. Crude-Oil-Repellent Membranes by Atomic Layer Deposition: Oxide Interface Engineering. *ACS Nano* **2018**, *12* (8), 8678–8685. https://doi.org/10.1021/acsnano.8b04632.

(39) Lee, J.; Lee, J.; Ahn, J.; Park, T. J.; Kim, W. Area-Selective Atomic Layer Deposition Using Vapor Dosing of Short-Chain Alkanethiol Inhibitors on Metal/Dielectric Surfaces. *Adv Mater Interfaces* **2022**, *9* (13). https://doi.org/10.1002/admi.202102364.

(40) Shehabeldeen, T. A.; El-Shafai, N. M.; El-Mehasseb, I. M.; Yin, Y.; Ji, X.; Shen, X.; Zhou, J. Improvement of Microstructure and Mechanical Properties of Dissimilar Friction Stir Welded Aluminum/Titanium Joints via Aluminum Oxide Nanopowder. *Vacuum* **2021**, *188*, 110216. https://doi.org/10.1016/j.vacuum.2021.110216.

(41) Wu, T.-M.; Tong, J.-Z.; Hsieh, J.-H. J.; Yang, Y. Sen. Improvement of Interfacial Adhesion of Al/Cr Films Deposited on Indium Tin Oxide Coated Glasses by Interfacial Oxidation. *Surf Coat Technol* **2004**, *183* (1), 89–95. https://doi.org/10.1016/j.surfcoat.2003.09.055.

(42) Lu, J.; Elam, J. W.; Stair, P. C. Atomic Layer Deposition—Sequential Self-Limiting Surface Reactions for Advanced Catalyst "Bottom-up" Synthesis. *Surf Sci Rep* **2016**, *71* (2), 410–472. https://doi.org/10.1016/j.surfrep.2016.03.003.

(43) Elers, K. -E.; Blomberg, T.; Peussa, M.; Aitchison, B.; Haukka, S.; Marcus, S. Film Uniformity in Atomic Layer Deposition. *Chemical Vapor Deposition* **2006**, *12* (1), 13–24. https://doi.org/10.1002/cvde.200500024.

(44) Zhang, Z.; Passlack, M.; Pitner, G.; Kuo, C.-H.; Ueda, S. T.; Huang, J.; Kashyap, H.; Wang, V.; Spiegelman, J.; Lam, K.-T.; Liang, Y.-C.; Liew, S. L.; Hsu, C.-F.; Kummel, A. C.; Bandaru, P. Sub-Nanometer Interfacial Oxides on Highly Oriented Pyrolytic Graphite and Carbon Nanotubes Enabled by Lateral Oxide Growth. *ACS Appl Mater Interfaces* **2022**, *14* (9), 11873–11882. https://doi.org/10.1021/acsami.1c21743.

(45) Bard, A. J.; Faulkner, L. R.; White, H. S. *Electrochemical Methods: Fundamentals and Applications*, Third.; John Wiley & Sons: Oxford, 2022.

(46) McCafferty, E. Validation of Corrosion Rates Measured by the Tafel Extrapolation Method. *Corros Sci* **2005**, *47* (12), 3202–3215. https://doi.org/10.1016/j.corsci.2005.05.046.

(47) Orazem, M. E.; Tribollet, B. *Electrochemical Impedance Spectroscopy*, 1st ed.; Kelly, R., Ed.; The Electrochemical Society (ECS): New Jersey, 2008; Vol. 906.

(48) Mansfeld, F.; Shih, H.; Greene, H.; Tsai, C. H. Analysis of EIS Data for Common Corrosion Processes. *Electrochemical impedance: analysis and interpretation. ASTM International.* **1993**, No. 1188, 37–53.

(49) Brug, G. J.; van den Eeden, A. L. G.; Sluyters-Rehbach, M.; Sluyters, J. H. The Analysis of Electrode Impedances Complicated by the Presence of a Constant Phase Element. *J Electroanal Chem Interfacial Electrochem* **1984**, *176* (1–2), 275–295. https://doi.org/10.1016/S0022-0728(84)80324-1.

(50) Pecho, P.; Veľký, P.; Bugaj, M.; Kajánek, D. Assessment of Aircraft Coating Resistance to Lighting Strikes and Long-Term Environmental Impact. *Aerospace* **2023**, *10* (3), 269. https://doi.org/10.3390/aerospace10030269.

(51) Lazorenko, G.; Kasprzhitskii, A.; Nazdracheva, T. Anti-Corrosion Coatings for Protection of Steel Railway Structures Exposed to Atmospheric Environments: A Review. *Constr Build Mater* **2021**, *288*, 123115. https://doi.org/10.1016/j.conbuildmat.2021.123115.

(52) Kumar, A.; Singh, J. OVERVIEW ON CORROSION IN AUTOMOTIVE INDUSTRY AND THERMAL POWER PLANT. *Proceedings on Engineering Sciences* **2022**, *4* (1), 13–22. https://doi.org/10.24874/PES04.01.003.

(53) Chang, S.-J.; Wang, S.-Y.; Huang, Y.-C.; Chih, J. H.; Lai, Y.-T.; Tsai, Y.-W.; Lin, J.-M.; Chien, C.-H.; Tang, Y.-T.; Hu, C. Van Der Waals Epitaxy of 2D *h* -AlN on TMDs by Atomic Layer Deposition at 250 °C. *Appl Phys Lett* **2022**, *120* (16). https://doi.org/10.1063/5.0083809.

(54) Riedl, T.; Winkler, T.; Schmidt, H.; Meyer, J.; Schneidenbach, D.; Johannes, H.-H.; Kowalsky, W.; Weimann, T.; Hinze, P. Reliability Aspects of Organic Light Emitting Diodes. In *2010 IEEE International Reliability Physics Symposium*; IEEE, 2010; pp 327–333. https://doi.org/10.1109/IRPS.2010.5488809.

(55) Elers, K. -E.; Blomberg, T.; Peussa, M.; Aitchison, B.; Haukka, S.; Marcus, S. Film Uniformity in Atomic Layer Deposition. *Chemical Vapor Deposition* **2006**, *12* (1), 13–24. https://doi.org/10.1002/cvde.200500024.

(56) Zhang, Z.; Passlack, M.; Pitner, G.; Kuo, C.-H.; Ueda, S. T.; Huang, J.; Kashyap, H.; Wang, V.; Spiegelman, J.; Lam, K.-T.; Liang, Y.-C.; Liew, S. L.; Hsu, C.-F.; Kummel, A. C.; Bandaru, P. Sub-Nanometer Interfacial Oxides on Highly Oriented Pyrolytic Graphite and Carbon Nanotubes Enabled by Lateral Oxide Growth. *ACS Appl Mater Interfaces* **2022**, *14* (9), 11873–11882. https://doi.org/10.1021/acsami.1c21743.

Chapter 4 Improved corrosion resistance and electrical characteristics of titanium, with atomic layer deposited (ALD) TiO_x coating

4.1 Abstract

Titanium (Ti), widely used in proton exchange membrane (PEM) based water electrolyzers, is prone to oxidation and related corrosion given the high operating voltages (> 2 V) and low pH (⩽5) conditions. Here, it is shown that a thin layer of ALD (atomic layer deposition) TiO_x can serve as a barrier for drastically reducing the corrosion of Ti. The robustness of the coatings was evaluated at high potentials (2.4V *vs.* RHE - reversible hydrogen electrode), in low pH and at elevated temperature (80ºC). A low TiO_x dissolution rate (< ~5 nm $year^{-1}$) along with five orders of magnitude enhanced current density, was observed for the ALD TiO_x coated Ti compared to uncoated Ti.

4.2 Introduction

Titanium has been widely used in aerospace[1], automotive[2], and biomedical[3] applications, based on its high specific strength and superior corrosion resistance[4–6]. Titanium can be anodized at high applied electrical potential, and such a process which can be used for self-coloring has been shown to yield high corrosion resistance[7–10]. The anodic oxide layer formed on the surface of Ti via anodization[11] has been shown to improve wear resistance and surface lubricity, as well as exhibit controllable dielectric characteristics and aesthetics[12].

Anodization based surface oxide formation is usually not desirable for Ti used in water electrolyzers operating at high voltages (> 2 V), as the oxide increases electrical contact resistance and reduces thermal conductivity of the anode current collectors[13]. Further, the corrosion rate of the oxide layer tends to increase with thickness[8] due to enhanced porosity[14], especially in low pH

(<5), high voltage, and high temperature (80°C) working conditions which make it easier to form porous anodic oxide. Consequently, a coating layer to protect the Ti substrate from corrosion while maintaining high electrical conductivity[13] is desired. Given that coatings involving noble metals, *e.g.,* Pt, Au, are expensive[13,15,16], an alternative cost-effective strategy to prevent Ti oxidation while preserving desirable Ti attributes is necessary.

Among the various coating technologies, atomic layer deposition (ALD) has emerged as a highly promising coating technique due to its ability to produce uniform, conformal, and pinhole-free thin films with precise atomic-scale control over thickness[17–19]. In comparison to physical vapor deposition (PVD) and sol-gel, ALD offers superior performance, particularly for corrosion resistant coatings[20–22]. For instance, PVD has issues related to uniform coverage on complex surfaces[23,24], while sol-gel coatings suffer from poor adhesion and mechanical instability[25,26]. Alternately, ALD, enables dense, defect-free films with high-quality interfaces[27], making it particularly suitable for rough substrates, *e.g.,* ALD TiO_x coatings are used in the semiconductor industry[28–30] and for corrosion protection[20–22], with excellent mechanical and thermal stability[31]-suitable for harsh operating conditions.

In the present study, it is shown that TiO_x deposited by ALD may be used as a viable coating and protection layer for Ti in the anode current collectors of water electrolyzers, and beneficial alternative to naturally formed anodic oxide layers. The ALD TiO_x coating was tested for several days at typical electrolyzer working conditions, *i.e.,* at (i) high voltages, ~ 2.4 V (with respect to the reversible hydrogen electrode: RHE), (ii) low pH (≤5), and (iii) elevated temperatures, up to ~ 80ºC. A proposed mechanism of corrosion protection by ALD TiOx *vs.* anodized Ti is schematically illustrated in **Fig. 4.1**. The oxygen generated at the anode can diffuse through the passive film formed on uncoated Ti and promote further oxidation of the metal[32,33].

This oxygen expansion within the anodic film induces the formation of pores in the anodic oxide layer[34]. In contrast, the non-porous ALD TiO_x serves as an effective diffusion barrier, inhibiting the permeation of oxygen and thereby preventing the continued growth of the oxide layer.

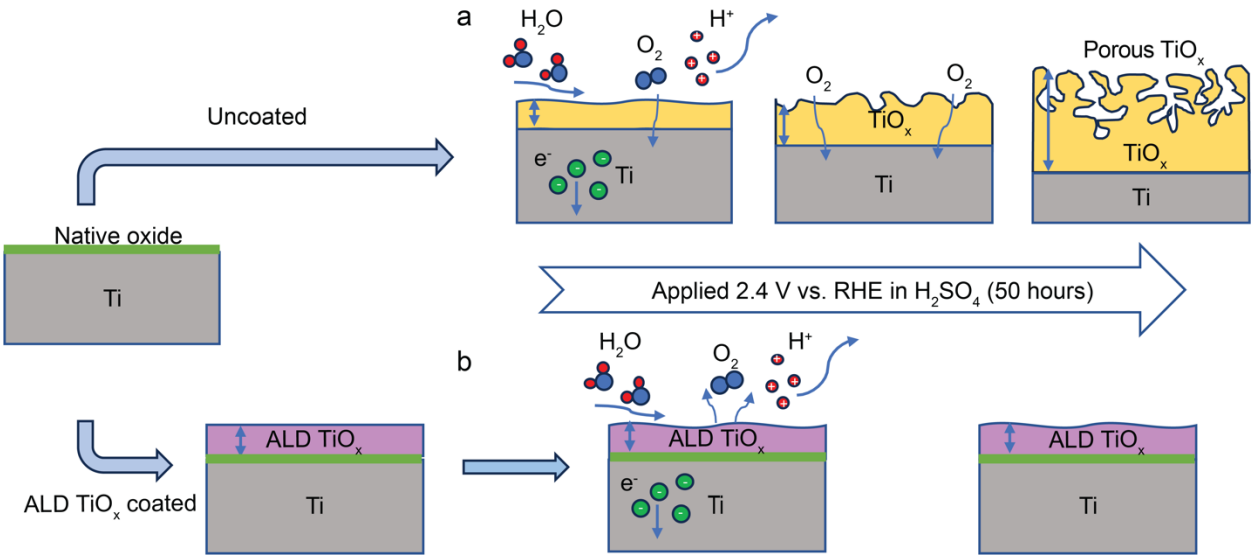


Figure 4.1 Proposed Mechanism for Corrosion Protection by ALD TiOx. Schematic of (a) anodization for uncoated, *vs.* (b) coated Ti in sulfuric acid (H_2SO_4) at electrolyzer working conditions, *i.e.,* with applied voltage (2.4 V *vs.* RHE) at elevated temperatures. While a thick layer of porous anodic oxide which is readily etched is generated on the native oxide and combined as one layer in the former case (*top*), the non-porous ALD TiO_x coating is etch resistant and preserves desirable Ti characteristics by preventing further oxide growth (*bottom*).

In the present study, the differences in the (a) structural morphology, (b) corrosion resistance, and (c) electrical conductivity of the uncoated *vs.* ALD TiO_x coated GR2 Ti (Grade 2 titanium) are documented. The characteristics of the oxide formation were investigated through detailed transmission electron microscopy (TEM) analysis. The corrosion resistance of the uncoated Ti as well as the ALD TiO_x coated Ti were analyzed through electrochemical measurements. It was shown that the ALD TiO_x improved the corrosion resistance while maintaining high electrical conductivity – significantly improving upon the attributes of the

uncoated Ti. The ALD TiO_x-coated titanium in this study demonstrates a corrosion current density three orders of magnitude lower than that previously recorded in previous studies of patterned Pt-TiO_x-coated titanium deployed as an anode current collector in water electrolyzers[35]. Additionally, the ALD TiO_x-coated Ti exhibited a significantly lower interfacial contact resistance (ICR) of approximately 1 $m\Omega \cdot cm^2$, compared to [36], say, Au-TiO_2-coated Ti, with an ICR of 4.2 $m\Omega \cdot cm^2$. The use of ALD TiO_x coatings is then advocated to open new avenues for robust and economically fabricated anode current collectors in electrolyzers.

4.3 Experimental Section

The details related to (i) specific material selection and pretreatment, (ii) ALD TiO_x deposition, (iii) electrochemical analysis, (iv) corrosion resistance measurements, and (v) electrical conductivity investigations will be discussed next.

Titanium sample preparation

Grade 2 titanium (GR2 Ti) (McMaster, Inc.) (Ti 99.02%, Al 0-0.10%, C 0.08% max, Fe 0.30% max, V 0-0.10%, other 0.40% max) was chosen for this study based on the attributes of good ductility[37] and corrosion resistance[38], and typical use in electrolyzers[39,40]. The GR2 Ti was cut into 1 cm x 1 cm x 0.075 cm samples and then mechanically polished (MP) using a Struers grinding and polishing apparatus (Tegramin, Struers *Inc.*) to a root mean square (*RMS*) roughness of $\leq$ 4 nm. The Ti samples were first polished on Tech-Cloth (Allied High-Tech Products. Inc.) using diamond suspension solution (DiaDuo-2 1 μm) with an applied compression of 30 N, with sample and stage rotation speeds of 200 rpm and 150 rpm, respectively. The samples were further polished on Final-P (Allied High-Tech Products. Inc.) using a silica suspension solution (OP-S 0.25 μm) with applied compression of 10 N, and sample and stage rotation speeds of 150 rpm.

Subsequently, the samples were ultrasonically cleaned, in (i) acetone, (ii) isopropanol (IPA), and (iii) deionized (DI) water, for 5 min each with a nitrogen blow dry after each step.

Atomic layer deposition (ALD) of TiO_x coating on Ti substrates

The TiO_x films on GR2 Ti samples were deposited by ALD (Beneq TFS 200), using $TiCl_4$ (99.99+% - Ti, Strem Chemicals, Inc..) and deionized H_2O (Veolia Water Technologies) precursors. A typical ALD cycle consisted of the following four successive steps, *i.e.,* (i) a $TiCl_4$ pulse, (ii) a N_2 gas purge, (iii) a H_2O pulse, and (iv) a N_2 gas purge. The N_2 purge gas was supplied from a liquid N_2 tank and then passed through a gas purifier (Entegris). Typical substrate temperatures of 120℃ and pulse lengths of 150 ms $TiCl_4$ and 50 ms H_2O, with an interval purge time of 2 s, for the ALD TiO_x were used, based on prior work[41]. A typical TiO_x growth rate of ~ 0.04 nm $cycle^{-1}$ was observed and enabled growth of films in the thickness range of 10 nm to 100 nm. The thickness was measured by ellipsometry (J.A. Woollam M-20000D) using the spectral variation of the relevant optical constants, see **Figure S4.1** in the *Supporting Information.* Transmission electron microscopy (ThermoFisher Talos 200X) was used to analyze the morphology and structure of the films as well as to confirm the film thickness.

Evaluation of the electrochemical stability through potentiostatic and potentiodynamic corrosion testing

For potentiostatic (PS) tests, the uncoated and ALD TiO_x coated GR2 Ti samples (with a typical sample area ~ 0.8 cm^2) were immersed in sulfuric acid solutions of different pH (pH 3, pH 5) at three representative temperatures (25°C, 55°C, and 80°C) for ~50 hours and subjected to an applied potential of 2.4V (*vs.* RHE). The pH 5 testing conditions were selected to simulate those relevant to electrolyzer operation as noted in previous studies[13]. In contrast, pH 3 was chosen to create a more aggressive testing environment. Additionally, elevated temperature testing at 80°C

was employed both as a model for accelerated anodization and to simulate the operational conditions of electrolyzers. The water bath containing the sulfuric acid was heated using a 1 L resin mantle (Glas-Col) with a temperature controller (Model 270; J-KEM). A three-electrode measurement setup, with the Ti samples as the working electrode (WE), the RHE as the reference electrode (RE), and a Pt wire as the counter electrode (CE), was used for testing with a Gamry Interface 5000E potentiostat (see **Figure S4.2** in the *Supporting Information*). All voltages reported in this study are relative to RHE. The temperature was stabilized for at least 5 mins prior to testing to determine the open circuit potential (E_{OC}). Electrochemical impedance spectroscopy (EIS) was performed both before and after the PS testing over a frequency range of 1 MHz to 0.2 Hz at 10 points per decade and a 10 mV AC perturbation on the applied 2.4 V DC. The EIS data fitting was performed using Gamry Echem Analyst® software, and the results are reported here with a relative error less than 5%.

Subsequent to the EIS and PS tests, potentiodynamic (PD) tests were performed at 80°C with voltage scans over the range of -0.6 V *vs.* E_{OC} to 1.6 V *vs.* the RHE. Here, the variation of the corrosion current density (J_{corr}) and corrosion potential (E_{corr}) were recorded from the polarization curves, and Tafel fits were performed within -50 mV to 50 mV *vs.* the E_{OC} region. The polarization resistance (R_p) was estimated through the Stern-Geary relation:

$$R_p = \frac{\beta_a \beta_c}{2.303 J_{corr}(\beta_a + \beta_c)}$$ [42,43] (4.1)

where β_a and β_c are the Tafel slopes of the anodic and cathodic regions, respectively. All measurements were repeated at least three times to estimate the random error.

Estimating elemental loss through inductively coupled plasma mass spectrometry (ICP-MS)

The loss of Ti (in the form of Ti^{4+} ions) from the anodic TiO_x as well as the ALD TiO_x films were monitored with a resolution of 0.01 ppb (parts per billion) using ICP-MS (iCAP RQ)

with a detection limit of 0.8 ng L^{-1} [44]. Typically, ~ 2 ml samples of the acid solutions were collected and tested over the duration of the potentiostatic testing. The Ti^{4+} concentrations were calibrated over a range of 0.01 ppb to 1000 ppb in 1% trace metal nitric acid (blank) which is diluted from TraceMetal™ Grade nitric acid (Fisher Chemical™). The blank (1% trace metal nitric acid) was forced to zero for reference.

Monitoring the electrical conductivity of the ALD TiO_x layers

Ni (50 nm in thickness) was deposited at ~ 1.5 Å s^{-1} on the uncoated and ALD TiO_x coated GR2 Ti after electrochemically testing using electron beam evaporation (Temescal, base pressure of ~ 5×10^{-7} Torr) and a shadow mask to yield 150 μm diameter electrodes. On the back side of the substrate, 2 nm thickness of Ti was sputter deposited at 100W, 2.3 mTorr (Denton Discovery 18) followed by 100 nm thickness of Au (at 200W, 2.5 mTorr) for electrical contacts. The current (I) – voltage (V) measurements were performed using a semiconductor device analyzer (Agilent B1500A) by applying a voltage sweep from 0 V to 2 V on the top contact while I was recorded from the back contact.

The structural and spectroscopic analysis was correlated with the electrochemical and electrical conductivity characteristics for the ALD TiO_x coated *and* uncoated Ti substrates. The ALD coatings confer superior corrosion resistance and maintain the ability to deliver electrical conductivity suitable for high performance electrolyzer applications.

4.4 Oxide Formation as a Function of pH and Temperature

The structural morphology, as well as the electrochemical attributes of the anodic oxide on Ti subjected to different pH and temperature conditions, was studied using TEM imaging and TEM energy dispersive spectroscopy (EDS). Representative results at five different testing conditions,

where the samples were immersed in sulfuric acid for 50 hours at 2.4 V (*vs.* the RHE), *i.e.*, (i) pH3 at 25°C, (ii) pH3 at 55°C, (iii) pH3 at 80°C, (vi) pH5 at 25°C, (v) pH5 at 80°C are shown in Figure 2. The thickness of the anodic oxide films on the uncoated Ti, was measured *via* ellipsometry as shown in **Fig. 4.2a**, with the corresponding TEM images in **Fig. 4.2b**.

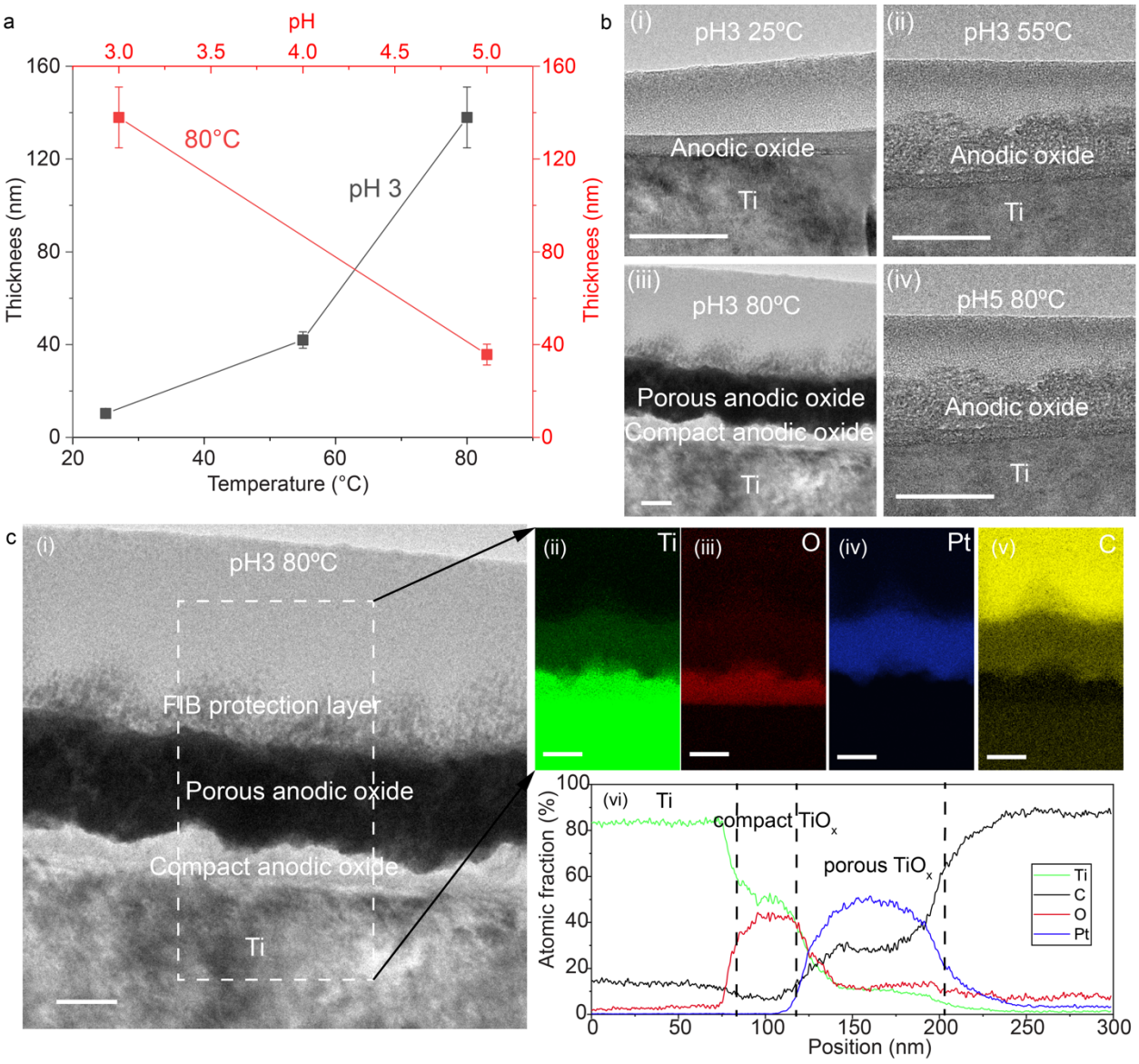


Figure 4.2 TEM characterization of anodic oxide on GR2 Ti after potentiostatic (PS) test in H_2SO_4 at 2.4 V (vs. RHE). **(a)** Oxide thickness estimated from ellipsometry as a function of temperature in pH3 H_2SO_4 (black), and as a function of pH at 80℃ (red). **(b)** The related TEM images of oxide films formed on GR2 Ti. **(c)** (i) TEM image of the formed anodic oxide after the PS test in pH3 H_2SO_4 at 80℃. (ii-v) EDS mapping of the dashed rectangular region, and (vi) the variation of the atomic fraction from the bottom to the top. Two layers of anodic TiO_x , *i.e.,* a porous layer at the top and a compact layer at the bottom, were observed. The Pt and C were deposited by FIB for TEM sample preparation to protect the porous anodic oxide. The scale bars in the image represent 50 nm.

The thickness of the anodic oxide on the Ti was observed to vary with temperature and pH in the sulfuric acid test solution. It should be noted that Ti anodic oxide thicknesses of ~ 130 nm are typically produced at room temperature at much higher voltages (> 50 V) [7,8] whereas in the present study at 80ºC, the voltage for thick anodic oxide growth was only 2.4 V (*vs.* RHE). As shown in the TEM images of **Fig. 4.2** (also see **Figure S4.3** in *the Supporting Information* for TEM images for all the given test conditions), it was observed that with increased thickness, the porosity of the oxide film was enhanced – presumably due to the expansion of the oxygen bubbles through the film[34,45] accompanied by suspected physico-chemical interactions arising from the ingress of the test solution. Note that the porosity determination is indirect from inspection of the TEM images; for example, by infiltration of the Pt and C protection layers into the TiO_x. A double layer anodic oxide, observed through scanning TEM energy dispersive spectroscopy (STEM-EDS) scans of the cross section, was generated after the PS test at pH 3 and 80°C for 50 hours as shown in **Fig. 4.2c**. Here, the inner oxide layer was found to be compact with lower Ti : O ratio compared to the outer layer. While the uncoated Ti formed thicker anodic oxide after the immersion in sulfuric acid at 2.4 V *vs.* RHE at elevated temperature, it was observed that the ALD TiO_x coated Ti maintains the originally deposited thickness after the PS testing - as indicated in **Figure S4.4** in the Supporting Information. The unaltered thickness of the ALD TiO_x layer suggests that it serves as an effective diffusion barrier, preventing further oxidation and protecting the underlying Ti substrate from corrosion. Such an aspect was consistent over a range of concentration of the H_2SO_4 solutions.

4.5 Comparative ICP-MS analysis

The corrosion resistance of the oxide formed on GR2 Ti and ALD TiO_x were investigated by ICP-MS, analyzing the Ti^{4+} concentration (C_{Ti}) in the PS test solution as a function of immersion time: **Fig. 4.3**. Here, two different ALD TiO_x thickness for each pH condition were studied to better understand the corrosion resistance related to the ALD TiO_x thickness. Thicker ALD TiO_x was chosen for pH 3 to overcome the more aggressive condition and prevent ALD TiO_x being over etched during the PS test.

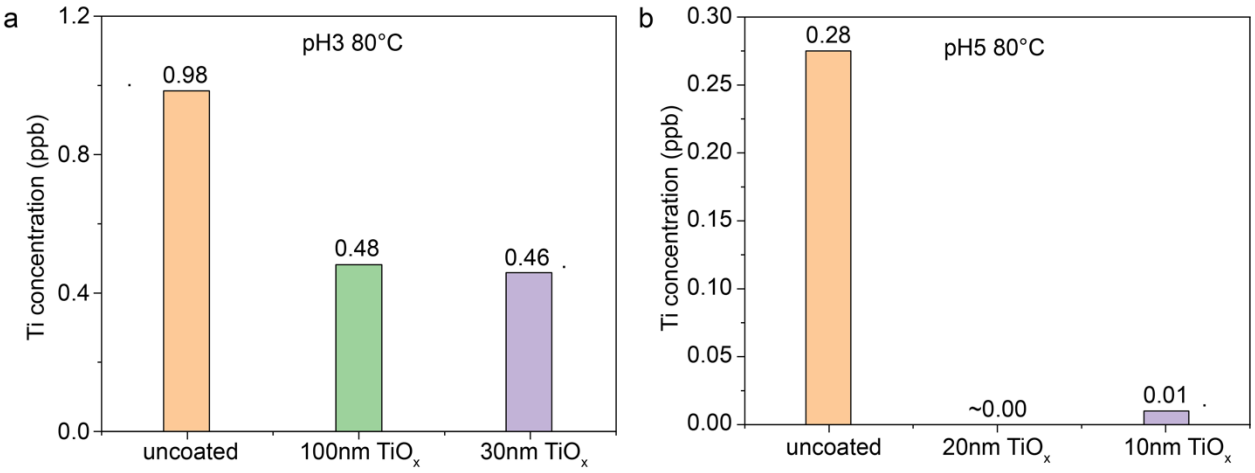


Figure 4.3 ICP-MS determination of the Ti (as Ti^{4+}), comparing uncoated Ti *with* ALD TiO_x coated Ti. ICP-MS after immersion in sulfuric acid and subject to 2.4 V (*vs.* RHE) in (a) pH 3, and (b) pH 5 solutions, at 80°C for 50 hours. The ALD TiO_x coated Ti was observed to be more corrosion resistant given the much lower detected Ti^{4+}.

ALD TiO_x coated Ti substrate has 2x lower corrosion rate at pH 3 and ⩾30x lower corrosion rate at pH 5 compared to uncoated Ti substrates. A metric related to a corrosion rate:

$$C.R. = \frac{[C_{Ti}]V_{sol} \cdot 24\ h \cdot 365\ d}{\rho_x A t} \qquad (4.2)$$

with V_{sol} as the volume of the test solution, ρ_x is the density of the TiO_x (~ 4.23 g cm^{-3}), A is the sampling area (~ 0.8 cm^2), t is the testing time (~ 50 hours) was employed to estimate the yearly corrosion rate assuming 365 d yr^{-1} and 24 hr day^{-1} operation. The *C.R.* of the ALD TiO_x coated Ti was < 5 nm $year^{-1}$ at pH 5 and 80°C. The outer porous oxide of lower density than the inner compact oxide would be expected to be more susceptible to corrosion. Here, a constant *C.R*. was assumed, as the C_{Ti} *vs.* time increased linearly (see **Figure S4.5** of *the Supporting Information*) and the measured current density during the PS test reached the steady state as further clarified through **Figure S4.6** of *the Supporting Information*. It was observed that the different thicknesses of ALD TiO_x exhibited similar *C.R.* under all tested pH conditions, indicating robust corrosion resistance. It may also be observed through a comparison of **Figs. 4.3(a)** and **(b)** that increasing the pH from 3 to 5 greatly reduces the relative rates of the dissolution of the Ti^{4+} from the ALD TiO_x coating. The observed phenomenon, whereby the corrosion rate of TiO_2 exhibits an exponential increase with higher concentrations of H_2SO_4, has been substantiated by multiple prior investigations in the field[46–48].

4.6 Electrochemical analysis of ALD TiO_x coated *vs.* uncoated Ti substrates

The electrical polarization curves[49] for the Ti samples with and without the ALD TiO_x are shown in **Fig. 4.4.** A lower current density $J = I/A$, with A as the sample area, was observed for all ALD TiO_x coated GR2 Ti samples compared to the uncoated samples. Tafel analysis over a small voltage range close to the origin (near the E_{oc} within ± 50 mV) of the polarization curve was performed to estimate the corrosion potential (E_{corr}), corrosion current density (J_{corr}), and polarization resistance (R_p). The obtained Tafel fit parameters are shown in **Table 4.1**.

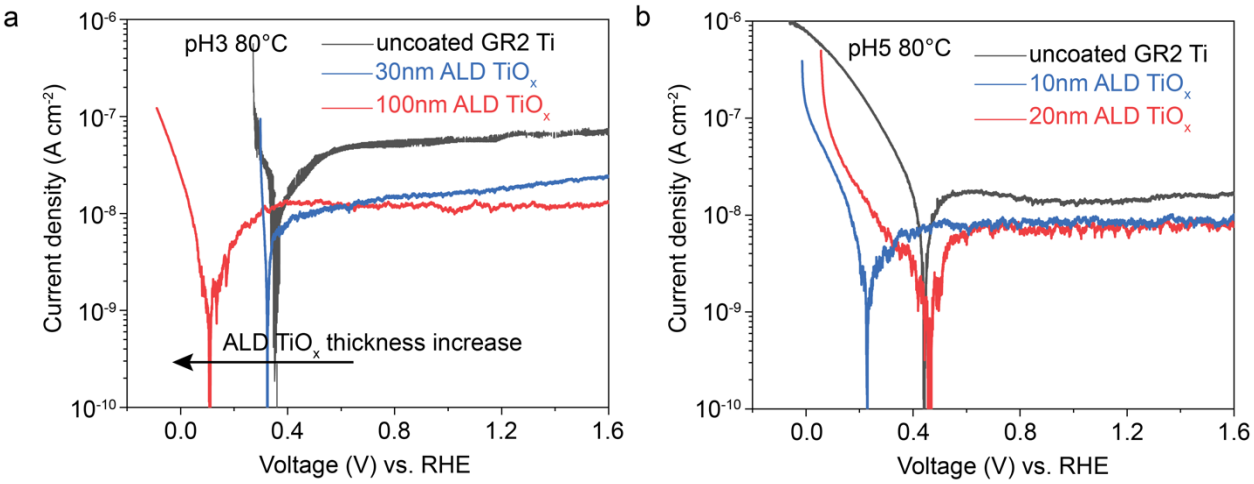


Figure 4.4 Comparison of the electrical polarization characteristics of uncoated *vs.* ALD TiO_x coated GR2 Ti samples. J-V after immersion of the samples in sulfuric acid at (a) pH3 80°C, and (b) pH5 80°C. The ALD TiO_x coated GR2 Ti generally has lower current density (*J*) compared to the uncoated Ti.

Table 4.1 Comparison of the Tafel fit parameters of uncoated and ALD TiO_x coated GR2 Ti, obtained from the experimental polarization curves, after the sample was tested in pH 3 and pH 5 H_2SO_4 at 80°C.

	Sample	J_{corr} (nA cm^{-2})	E_{corr} (mV)	R_p (Ω cm^{-2}) × 10^6
pH 3 80°C	**Uncoated**	72	402	0.33
	30 nm	10	163	2.8
	100 nm	13	112	8.5
pH 5 80°C	**Uncoated**	23	441	3.8
	10 nm	8	235	10.6
	20 nm	2	448	26.6

The ALD TiO_x coated Ti generally had much lower J_{corr}, with the decrease from the uncoated sample increasing at lower pH. For instance, it was noted that the ALD TiO_x (100 nm and 30 nm) coated GR2 Ti has a factor of seven lower J_{corr} (~10 nA cm^{-2}) compared to the uncoated GR2 Ti (72 nA cm^{-2}) in pH3 H_2SO_4, indicative of significantly reduced corrosion due to the ALD coating. Similarly, the 10 nm and 20 nm ALD TiO_x coated GR2 Ti had 3x and 10x lower J_{corr}, *i.e.,*

8 nA cm^{-2} and 2 nA cm^{-2} compared to the uncoated GR2 Ti (~ 23 nA cm^{-2}) in pH5 H_2SO_4. Furthermore, the J_{corr} was seen to be a weak function of the ALD coating thickness, with respect to the pH, varying in the range of ~ 2 *to* 13 nA cm^{-2}, for the tested pH conditions. It was also observed that the ALD TiO_x coated Ti samples generally have smaller E_{corr}, with increasing coating thickness, *e.g.,* ~ 112 mV for 100 nm TiO_x, and ~ 163 mV for 30 nm TiO_x, in pH 3 sulfuric acid compared to ~ 400 mV for the uncoated Ti. The smaller E_{corr} with ALD TiO_x observed at pH 3 H_2SO_4 suggests less stability to oxidation and could be correlated to a lower oxidation state than the nominal anodic oxide ($TiO_3 \cdot 2H_2O$ at pH 3 80ºC)[50,51] inferred from the Pourbaix diagram.

The difference in E_{corr} between ALD TiO_x and anodic oxide is less pronounced in the higher pH H_2SO_4 testing solution (pH 5). The smaller E_{corr} (235 mV) for the 10 nm ALD TiO_x coated GR2 Ti compared to the 20 nm ALD TiO_x coated and uncoated Ti (~450 mV) after PS testing is due to higher electrical conductivity with more oxygen generated and dissolved in the electrolyte during the PS test[52] , as will be further discussed in section 3.5. Harnessing the significantly lower J_{corr} due to the ALD coating, the related R_p was up to an order of magnitude larger for the TiO_x coated Ti compared with the uncoated samples, yielding another measure of the greater robustness to corrosion[53,54] in the former case. The improvement ratios of J_{corr} and R_p for ALD TiO_x-coated and uncoated Ti derived from the PD test cannot be directly compared to the ICP-MS results. This discrepancy arises because the PD measurement is related to E_{corr}, which indicates corrosion resistance in acidic solutions, while the ICP-MS data correspond to the operational conditions of the electrolyzer under an applied positive voltage of 2.4 V *vs.* RHE.

4.7 Electrochemical impedance spectroscopy (EIS) analysis

EIS was performed on both uncoated and ALD TiO_x coated Ti samples while immersed in pH 3 H_2SO_4. The EIS experiments were not performed for pH 5 related testing conditions due to the solution resistance exceeding the maximum impedance measurement limit of the instrument of 10 MΩ. **Fig. 4.5**(a) shows the measurements on the samples subjected to 2.4 V (vs. RHE) before and after the 50-hour PS testing. **Fig. 4.5 (b)** indicates a plausible equivalent electrical circuit model[55,56] to fit the measured EIS data. Here, the model incorporates the background resistance of the electrolyte R_s and the resistance related to the porosity in the oxide R_{pore} in addition to capacitive characteristics defined in terms of a constant phase element (CPE) - by Q_f and Q_{dl} associated with the film and double layer capacitance - through an impedance:

$$Z_{CPE} = \frac{1}{Q(j\omega)^{\alpha}}^{57} \qquad (4.3)$$

Here, Q is the nominal capacitance and α represents the exponent related to the CPE characteristic, *i.e.,* $\alpha = 1$ for an ideal capacitor, and α_f and α_{dl} are the exponents for Q_f and Q_{dl}, respectively. Further, the charge transfer resistance (R_{ct}) related to the chemical reactions, *e.g.,* film corrosion, oxidation, *etc.* at the film-electrolyte interface, has also been incorporated. **Table 4.2** shows the fit parameters related to the EIS experiments.

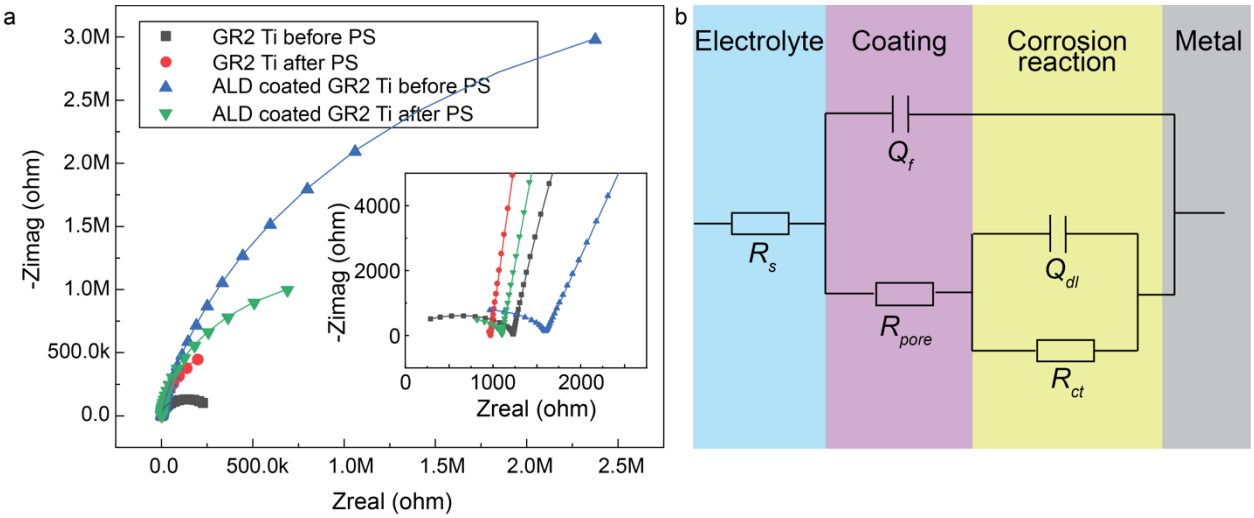


Figure 4.5 EIS measurements and modeling of the uncoated and ALD TiO_x coated Ti samples. (a) EIS measurements, with the samples indicated in the *inset labels,* subject to 2.4V (vs. RHE) in pH 3 H_2SO_4 at 80°C, before and after PS testing over ~50 hours. The lines represent fits to the data, as modeled through (b) an equivalent circuit model. Here, the electrolyte-related resistance: R_s, the resistance related to the porosity in the oxide: R_{pore} in addition to the constant phase elements, represented by Q_f and Q_{dl}, associated with the film and double layer capacitance, respectively are considered. The R_{ct} represents charge transfer reaction associated resistance.

Table 4.2 Fit parameters from modeling of the EIS spectra for GR2 Ti without *and* with 30 nm of ALD TiO_x coating at pH 3 and 80°C – of the experiments related to **Fig. 4.5(a)**.

Sample	R_s (Ω cm^2)	R_{pore} (Ω cm^2) ($\times 10^3$)	Q_f (Ω^{-1} cm^{-2} s^a) ($\times 10^{-11}$)	α_f	Q_{dl} (Ω^{-1} cm^{-2} s^a) ($\times 10^{-6}$)	α_{dl}	R_{ct} (Ω cm^2) ($\times 10^6$)
Uncoated before PS	29.5	1.2	27	0.79	1.4	0.95	0.3
Uncoated after PS	37.6	1.0	2.1	1.00	1.5	0.97	1.4
30 nm before PS	34.5	1.6	8.0	1.00	0.2	0.89	7.7
30 nm after PS	31.3	1.1	8.5	1.00	0.5	0.96	2.4

From the equivalent circuit fits, it was observed that the average background R_s was ~33.2 ± 3.6 Ω. A higher R_{pore} related to the ALD coated Ti substrate is indicative of lower porosity,

corresponding to the results observed from TEM imaging - as discussed in section 3.1 that the porous nature of the anodic oxide corresponds to the lower R_{pore}. While the oxide capacitance, associated with Q_f , is significantly decreased in the uncoated samples after the PS testing, consistent with porous oxide formation (**Fig. 4.2)**, further deterioration has been reduced due to the ALD coating. For instance, after PS testing, with ALD TiO_x, Q_f is relatively unchanged (of < 10%), in contrast to the order of magnitude change observed in the uncoated samples . With respect to the interfacial influences (associated with Q_{dl} and R_{ct}), it was noted that Q_{dl} is reduced by ~5x in average due to the ALD coatings. The reduction in porosity and the diminished surface area can be attributed to the observed decrease in Q_{dl}.. Concomitantly, the increased R_{ct}, for the ALD coated samples compared to the uncoated GR2 Ti, is representative of better immunity to chemical reactions[58] and associated corrosion resistance. Since a similar *C.R.* was observed for different thicknesses of ALD TiO_x coated Ti, the R_{ct} could be considered primarily as a function of the intrinsic chemical stability of the ALD TiO_x. Considering the higher *C.R.* and lower R_{ct} of the uncoated Ti, the degradation mechanisms over an extended operational period could involve both (a) the dissolution of the anodic oxide – at a high dissolution rate, and (b) the formation of a new anodic oxide layer. In contrast, for ALD TiO_x coated Ti, the degradation is likely limited to the dissolution of the ALD TiO_x layer, which occurs at a much lower dissolution rate.

In summary, it may be concluded that the ALD TiO_x coating of Ti helps in preserving stable oxide characteristics and hence the integrity of the underlying substrates under corrosive environments. Such stability may also be correlated to the lower leaching of Ti, pertinent to the ICP-MS results of **Fig. 4.3a**.

4.8 Electrical conductivity variation of the uncoated and ALD coated Ti samples

A significant difference in the electrical conductivity:

$$\sigma = \frac{l}{RA} \qquad (4.4)$$

between the uncoated and the ALD TiO_x coated samples was observed after the samples were subject to PS testing. Here, l is *either* the thickness of the anodic oxide layer (for uncoated samples) *or* that of the ALD TiO_x layer, R is the measured electrical resistance, and A is the area of the top gate. The uncoated samples indicated a σ of ~ 10^{-10} S m^{-1}, whereas the σ for the ALD samples was five orders of magnitude higher, at ~ 10^{-5} S m^{-1} . This substantial increase in conductivity corresponds to a significantly enhanced current density (J), as illustrated in **Figure 4.6**. The electrical conductivity of the ALD TiO_x-coated titanium was found to be further enhanced to ~ 0.1 S m^{-1} by removing the native oxide layer on the titanium substrate/s prior to the ALD TiOx deposition, as demonstrated in **Figure S4.7** in *the Supporting Information*. Consequently, a low ICR of ~ 1 mΩ·cm^2 was achieved, comparable to that of precious metal-coated Ti current collectors[36].

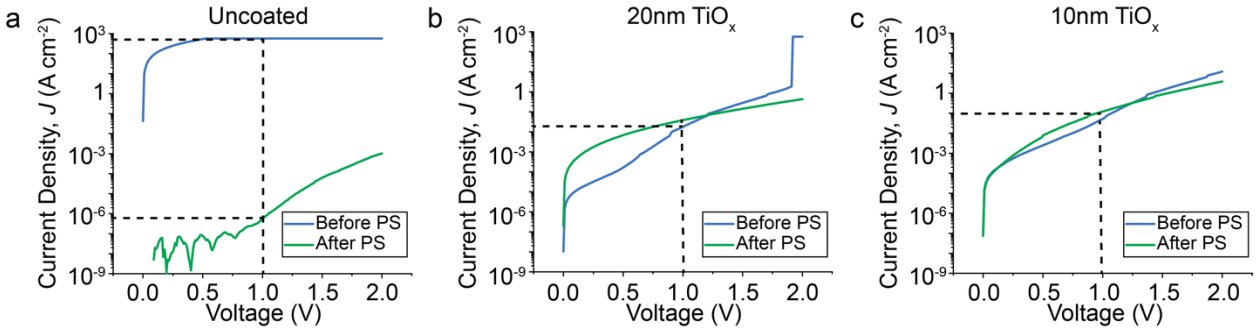


Figure 4.6 Current-voltage (J-V) characteristics before and after the PS testing. J-V for (a) uncoated, (b) 20 nm ALD TiO_x coated, and (c) 10 nm ALD TiO_x coated Ti samples in pH 5 H_2SO_4 at 80°C. Substantially decreased J after the testing was observed for the uncoated Ti - indicating thick anodic oxide formation. Conversely, the J in the ALD TiO_x coated Ti is robust with respect to testing, due to the coating serving as an oxygen diffusion barrier and preventing further anodization.

There was a drastic decrease in the measured J on the uncoated Ti samples, after the PS test, from ~ 100 A cm^{-2} to μA cm^{-2} observed at 1 V, corresponding to substantial oxide growth. However, the measured J was relatively constant before and after the PS test for all the ALD TiO_x coated Ti samples, implying negligible anodic (interfacial) oxide growth. Consequently, the electrical conductivity is maintained and robust, due to the ALD coating. It was noted that the J increased exponentially with reduced ALD coating thickness, *e.g.,* ~ 100 mA cm^{-2} *vs.* 20 mA cm^{-2} at 1 V for the 10 nm *vs.* 20 nm, TiO_x coating thickness. As the *C.R.* is independent of the thickness of the ALD TiO_x layer and the electrical conductivity decreases proportionally with increasing thickness, an *optimal* thickness must be determined. Such an optimal thickness has the attributes related to (i) avoidance of porosity – which is relevant at small thickness as well as with native oxide/s, while (ii) achieving higher electrical conductivity – amenable at smaller ALD TiO_x coating thickness.

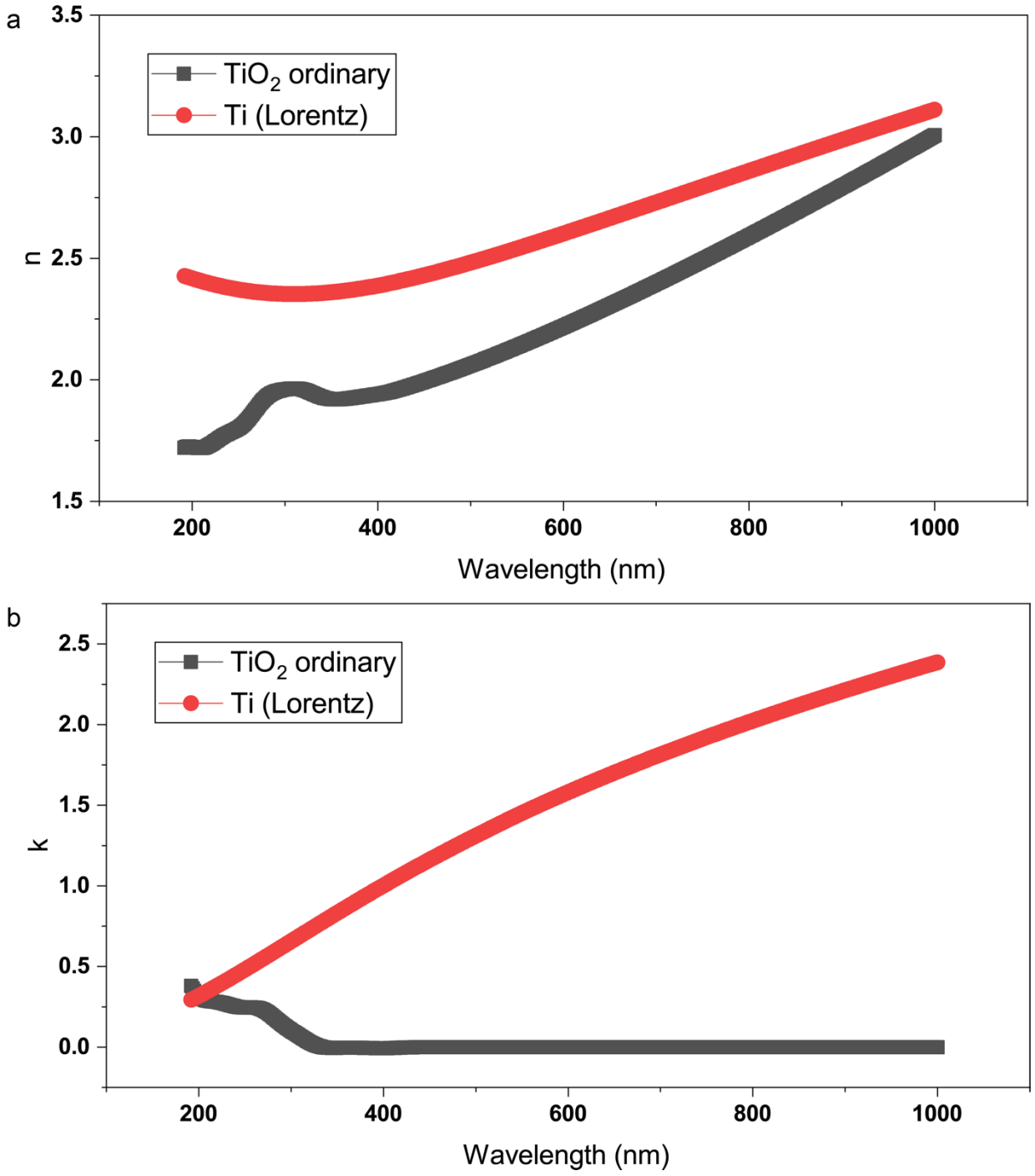
In our study, a 10 nm ALD TiO_x layer was seen to be sufficient to ensure a coating lifespan of up to two years while preserving the high electrical conductivity. The higher σ of the 10 nm TiO_x coated Ti, and the resultant higher oxygen evolution, plausibly explains the unusually low E_{corr} observed in the polarization curve (section 3.3). Similar observations, indicating the electrical stability of the ALD coating, were recorded at pH 3 80ºC as well - shown in **Figure S4.8** in *the Supporting Information*.

4.9 Conclusion

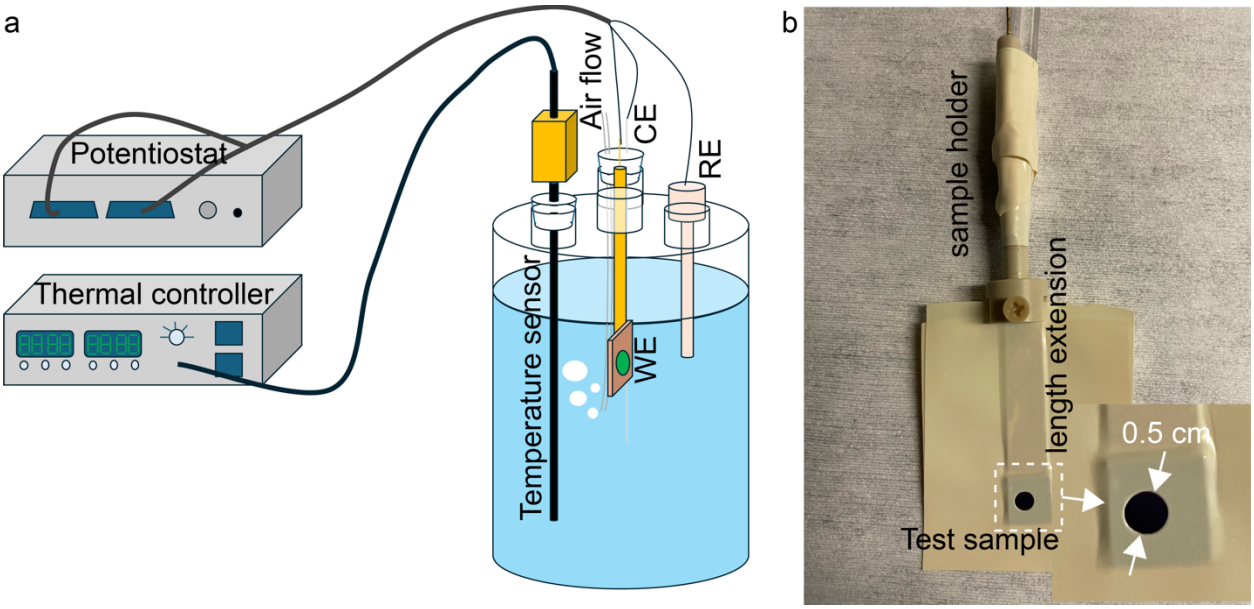
The present study documents that ALD TiO_x coatings could be deployed to reduce the extent of oxide formation on Ti in a variety of pH and applied voltage and temperature test conditions relevant to industrial electrolyzer operating conditions[13,15,16]. A significantly enhanced

corrosion resistance was observed on the ALD TiO_x coated Ti with ⩾30x lower rate of corrosion in pH5 sulfuric acid, as inferred from ICP-MS. Further, ALD coating was used to enhance the electrical conductivity, which is maintained even when the samples were subject to acidic environments at elevated temperatures up to 80ºC. It is suggested that the beneficial effect of the ALD coating arises from its role as an oxygen diffusion barrier, preventing further oxide growth on the Ti substrate.

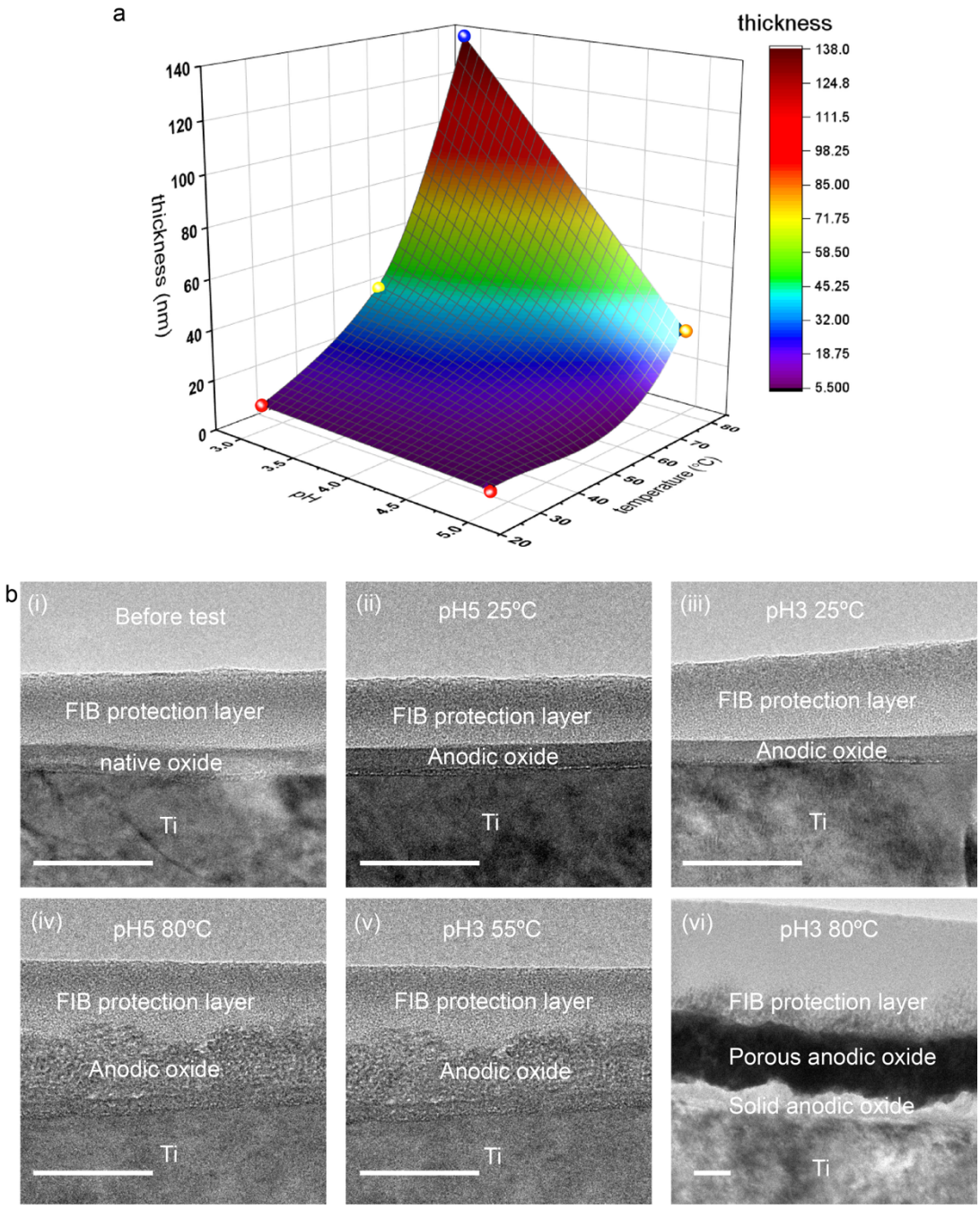
4.10 Supporting Information



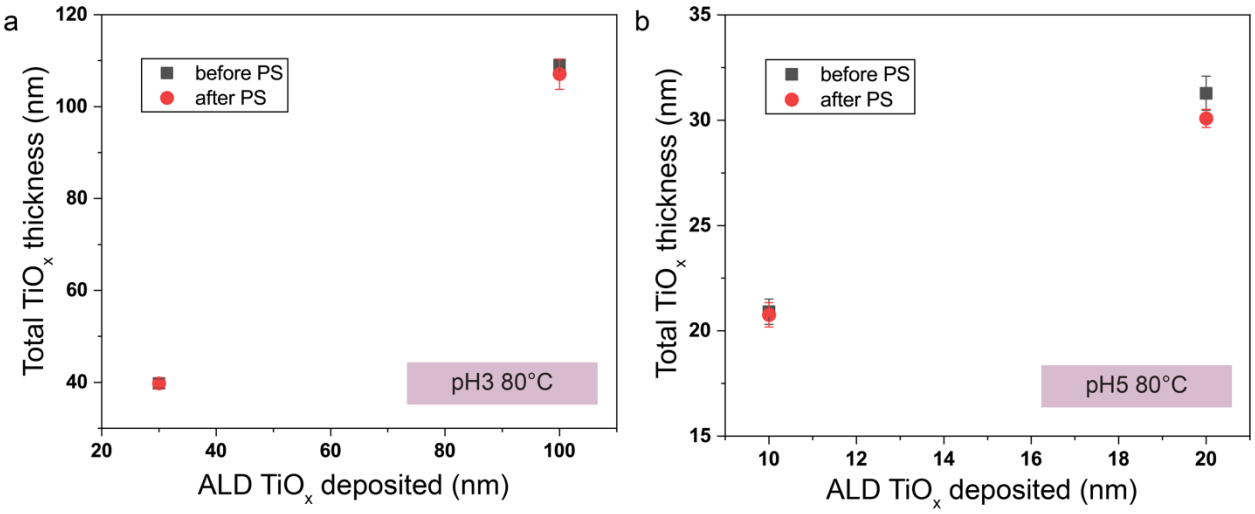
Supplemental Figure 4.1 Optical constant vs. wavelength (nm). The thickness of the anodic TiO_x and ALD TiO_x was measured on mechanical polished Grade 2 Ti assuming monolayer TiO_x on Ti substrate with the optical constant of (a) n and (b) k (the refractive index and extinction coefficient of the TiO_x thin film to fit the thickness with ellipsometry measured data)



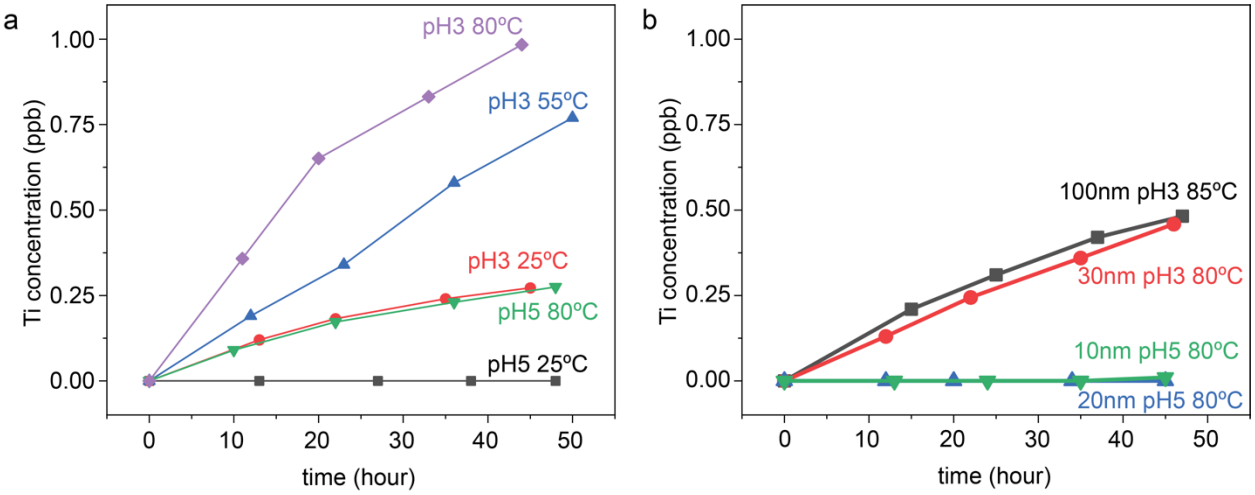
Supplemental Figure 4.2 Experimental setup for electrochemical testing (a) The schematic of the setup for electrochemical testing – for both the potentiostatic (PS) and potentiodynamic (PD) tests using three-electrode measurement with the test sample as the working electrode (WE), regular hydrogen electrode as the reference electrode (RE), and platinum wire as the counter electrode (CE). A temperature sensor is attached and air (up to 5 cc/min) was bubbled through the testing solutions during the PS tests. A positive potential of 2.4 V (vs. RHE) was applied between the WE and the CE. (b) Optical image shows how the test sample taped with a controlled exposed area of 0.785 cm^2.



Supplemental Figure 4.3 Ellipsometry and TEM characterization of anodic film on GR2 Ti after potentiostatic (PS) test in H_2SO_4 at 2.4 V vs. RHE. (a) the thickness of the anodic oxide film formed on GR2 Ti after the PS test at different pH and temperature conditions, as measured using ellipsometry. It was noticed that the thickness of the anodic oxide increases with the increase of the temperature or decrease of the pH, **(b)** TEM characterization of native oxide and anodic oxide on GR2 Ti before and after the PS test at 2.4 V (vs. RHE) at different pH and temperature conditions. A porous anodic oxide was formed on GR2 Ti at lower pH and higher temperature.

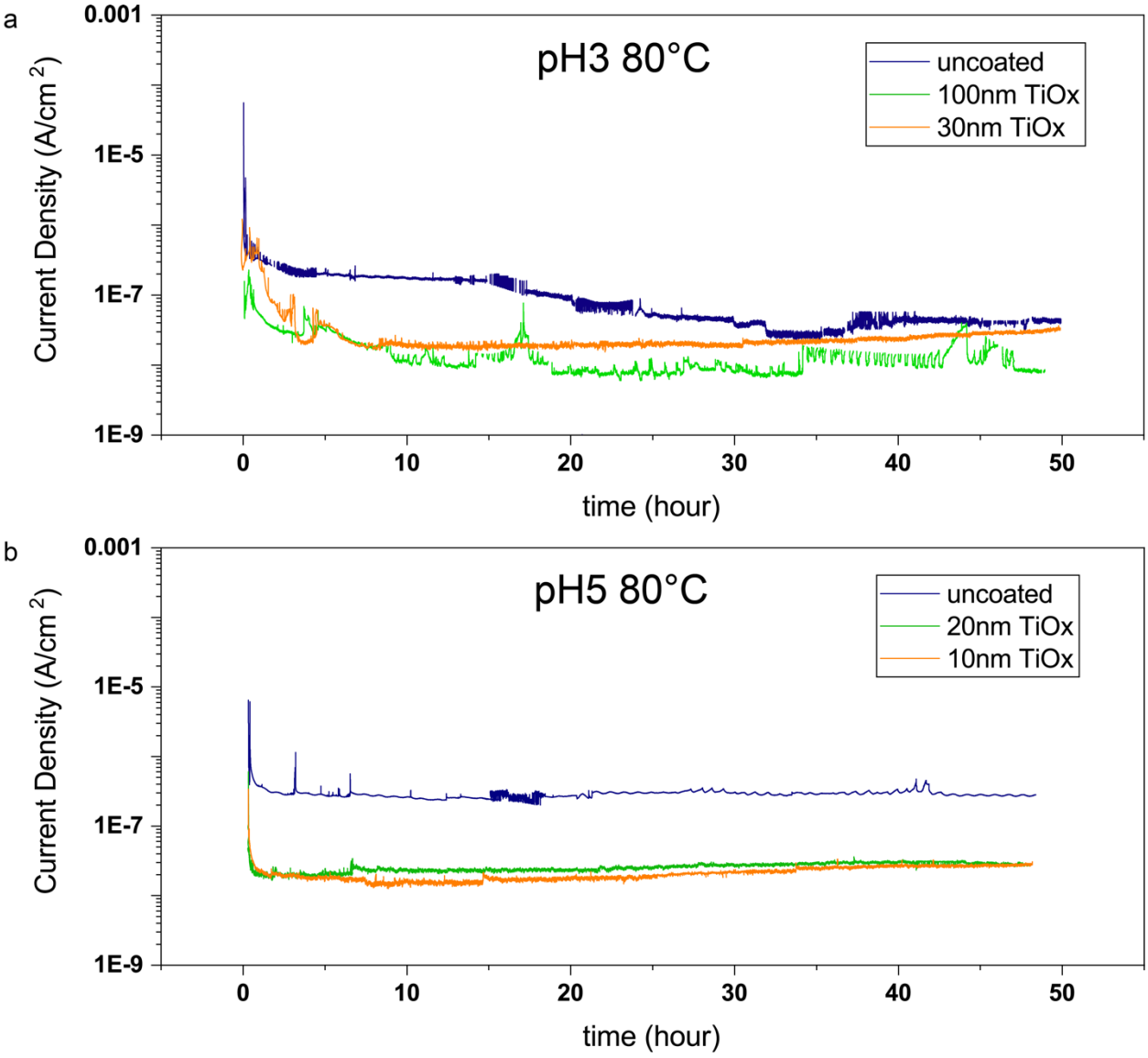


Supplemental Figure 4.4 Thickness measured through ellipsometry, for ALD TiO_x coated Ti before and after the PS test. (a) pH3 80ºC and (b) pH5 80ºC. The total thickness measured includes the native oxide on Ti before the ALD deposition. It was observed that the ALD TiO_x was able to maintain the same thickness before and after the PS test by preventing further oxidation, due to being an oxygen diffusion barrier.

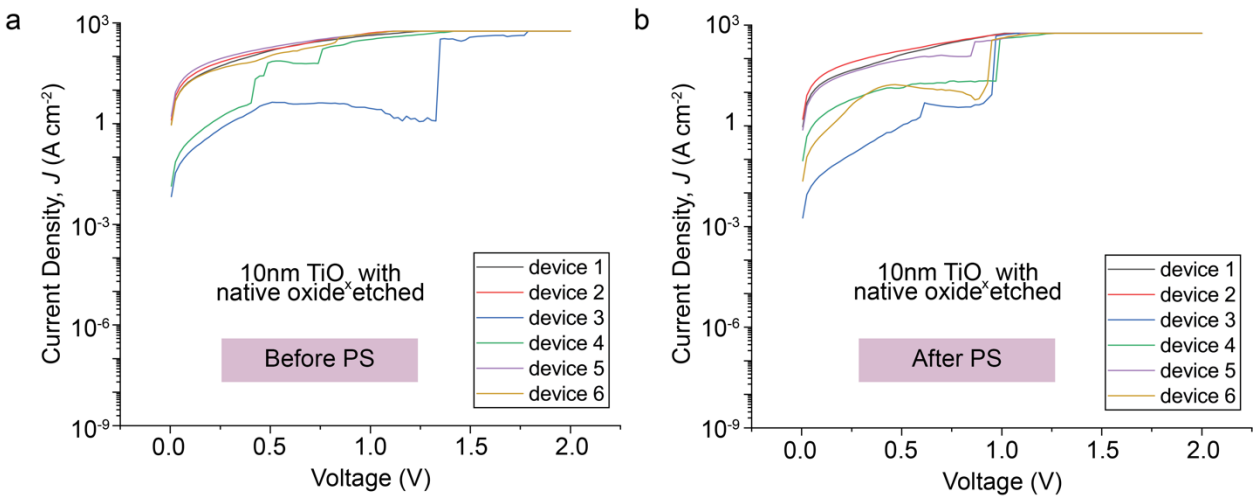


Supplemental Figure 4.5 ICP-MS results related to the elemental loss of Ti (as Ti^{4+}) as a function of time, for (a) uncoated Ti, and **(b)** ALD TiO_x coated Ti. The samples were immersed in different pH H_2SO_4 at different temperature and held at 2.4V (vs. RHE). The anodic

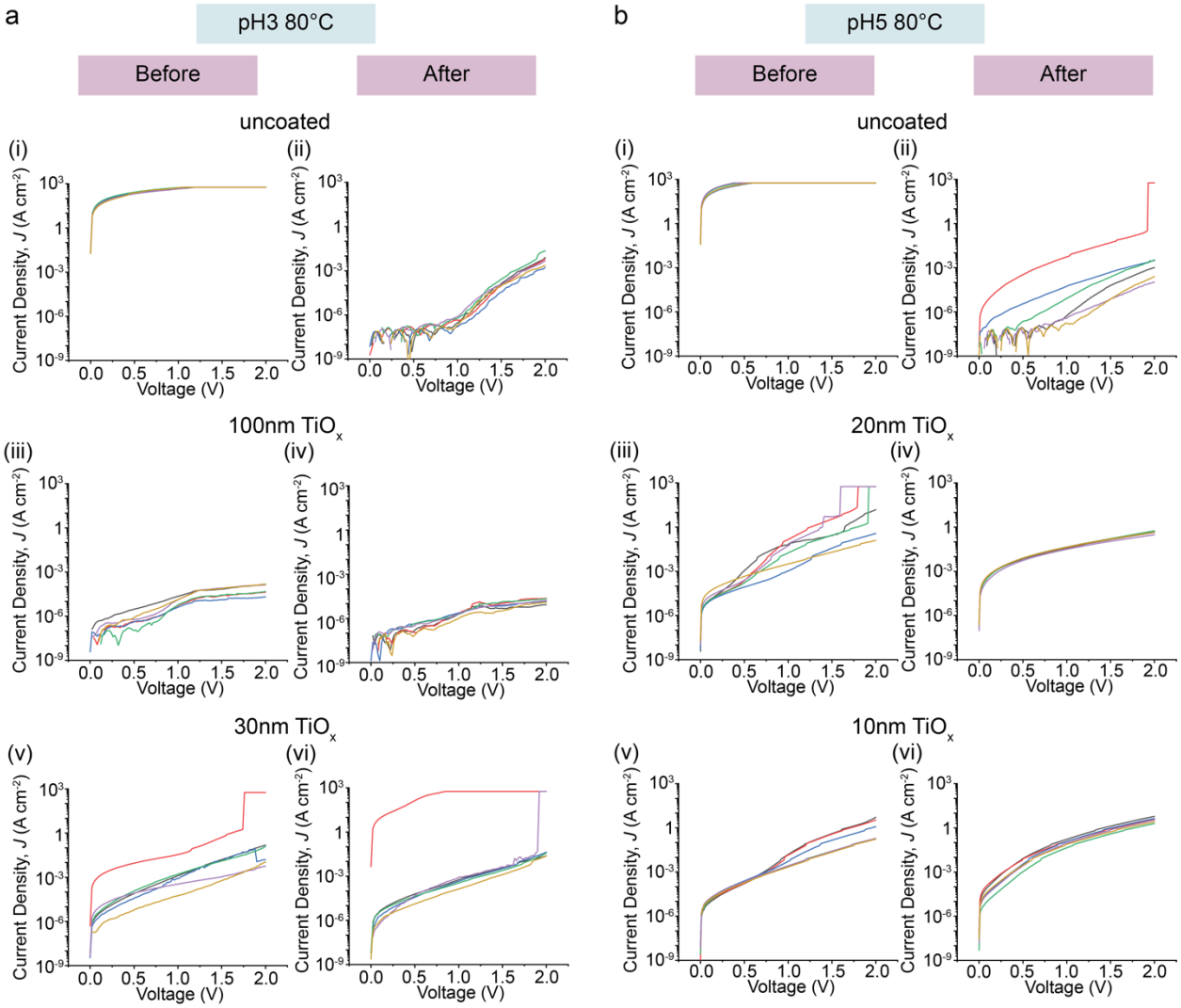
oxide (formed on uncoated Ti) was observed to have higher dissolution rate at higher temperature and lower pH, while the ALD TiO_x coated GR2 was observed to be more corrosion resistant – due to with lower Ti^{4+} detected from the ICP-MS.



Supplemental Figure 4.6 The current density as a function of time during the potentiostatic (PS) testing. (a) pH3 80ºC and (b) pH5 80ºC. The current density involving processes related to, *e.g.,* (i) oxygen evolution, (ii) anodic oxide generation on uncoated GR2 Ti, and (iii) TiO_x (anodic or ALD deposited) dissolution, tends to reach a steady state after a few hours of testing.



Supplemental Figure 4.7 The current density (J) – voltage characteristics of ALD TiO_x-coated Ti, where the native oxide was wet etched by HF prior to ALD deposition, evaluated both (a) before and (b) after PS testing at pH5 H_2SO_4 at 80°C. The current density (*J*) was increased from ~10^{-1} A cm^{-2} to ~10^{3} A cm^{-2} upon etching the native oxide on titanium, corresponding to a high electrical conductivity (σ) of 0.1 S m^{-1} and a low interfacial contact resistance (ICR) of 1 mΩ·cm^2. The relatively low device yield of 4 out of 6 is attributed to the formation of a nonuniform oxide layer during the transition between the wet etching process and ALD deposition.



Supplemental Figure 4.8 Current density (*J*) - voltage characteristics for uncoated and ALD TiO_x coated Ti samples before and after the PS testing. (a) pH3 H_2SO_4 at 80°C and (b) pH5 H_2SO_4 at 80°C. A substantially decreased *J* after the PS testing was observed for the uncoated Ti, indicating thick oxide formation due to anodization over time. However, the ALD TiO_x coated Ti has a constant *J* after the PS testing. Exponentially increased *J* were observed with thinner ALD TiO_x coating, *e.g.*, ~ 100 mA cm^{-2} *vs.* 2 mA cm^{-2} for the 10 nm *vs.* 20 nm, TiO_x coating tested at pH 5 80°C and ~ 800 µA cm^{-2} *vs.* 2 µA cm^{-2} for the 30 nm *vs.* 100 nm, TiO_x coating tested at pH 3 80°C.

4.11 Acknowledgements

This work was partially conducted at the San Diego Nanotechnology Infrastructure (SDNI) of UCSD, a member of the National Nanotechnology Coordinated Infrastructure, supported by the

National Science Foundation (Grant ECCS-2025752). The authors would like to thank Dr. Neal Arakawa of the Environmental and Complex Analysis Laboratory at UC San Diego for his assistance with the ICP-MS measurements. Additionally, the authors express their gratitude to Yaneth Hernandez for her contributions to the development and interpretation of the corrosion tests and results.

Chapter 4, in full, is a reprint of the material as it appears in "Improved corrosion resistance and electrical characteristics of titanium, with atomic layer deposited (ALD) TiO_x coating." *Applied Surface Science* 692 (2025): 162719 by Kesong Wang, Adam Paxson, Thomas I. Valdez, Ahmet G. Erlat, Ping-Che Lee, Seonguk Yun, Andrew C. Kummel, and Prabhakar R. Bandaru. The dissertation author was the primary researcher and author of this material.

4.12 Reference

(1) Boyer, R. R. An Overview on the Use of Titanium in the Aerospace Industry. *Materials Science and Engineering: A* **1996**, *213* (1–2), 103–114. https://doi.org/10.1016/0921-5093(96)10233-1.

(2) Schauerte, O. Titanium in Automotive Production. *Adv Eng Mater* **2003**, *5* (6), 411–418. https://doi.org/10.1002/adem.200310094.

(3) Rack, H. J.; Qazi, J. I. Titanium Alloys for Biomedical Applications. *Materials Science and Engineering: C* **2006**, *26* (8), 1269–1277. https://doi.org/10.1016/j.msec.2005.08.032.

(4) Ribeiro, M. V.; Moreira, M. R. V.; Ferreira, J. R. Optimization of Titanium Alloy (6Al–4V) Machining. *J Mater Process Technol* **2003**, *143–144*, 458–463. https://doi.org/10.1016/S0924-0136(03)00457-6.

(5) RAHMAN, M.; WANG, Z.-G.; WONG, Y.-S. A Review on High-Speed Machining of Titanium Alloys. *JSME International Journal Series C* **2006**, *49* (1), 11–20. https://doi.org/10.1299/jsmec.49.11.

(6) Veiga, C.; Davim, J. P.; Loureiro, A. J. R. Properties and Applications of Titanium Alloys: A Brief Review. *Rev. Adv. Mater. Sci* **2012**, *32* (2), 133–148.

(7) Sharma, A. K. Anodizing Titanium for Space Applications. *Thin Solid Films* **1992**, *208* (1), 48–54. https://doi.org/10.1016/0040-6090(92)90946-9.

(8) Karambakhsh, A.; Afshar, A.; Ghahramani, S.; Malekinejad, P. Pure Commercial Titanium Color Anodizing and Corrosion Resistance. *J Mater Eng Perform* **2011**, *20* (9), 1690–1696. https://doi.org/10.1007/s11665-011-9860-0.

(9) İzmir, M.; Ercan, B. Anodization of Titanium Alloys for Orthopedic Applications. *Front Chem Sci Eng* **2019**, *13* (1), 28–45. https://doi.org/10.1007/s11705-018-1759-y.

(10) Delplancke, J.-L.; Degrez, M.; Fontana, A.; Winand, R. Self-Colour Anodizing of Titanium. *Surface Technology* **1982**, *16* (2), 153–162. https://doi.org/10.1016/0376-4583(82)90033-4.

(11) Biestek, T.; Weber, J. *Electrolytic and Chemical Conversion Coatings : A Concise Survey of Their Production, Properties and Testing*, 1st edition.; Portcullis Press Ltd: Redhill, 1976.

(12) Singh, S.; Kumar, S.; Khanna, V.; Singh, H. Reliable Surface Modification Techniques. In *Thermal Spray Coatings: Materials, Techniques & Applications*; BENTHAM SCIENCE PUBLISHERS, 2024; pp 43–75. https://doi.org/10.2174/9789815223552124010005.

(13) Teuku, H.; Alshami, I.; Goh, J.; Masdar, M. S.; Loh, K. S. Review on Bipolar Plates for Low-temperature Polymer Electrolyte Membrane Water Electrolyzer. *Int J Energy Res* **2021**, *45* (15), 20583–20600. https://doi.org/10.1002/er.7182.

(14) Oh, H.-J.; Lee, J.-H.; Jeong, Y.; Kim, Y.-J.; Chi, C.-S. Microstructural Characterization of Biomedical Titanium Oxide Film Fabricated by Electrochemical Method. *Surf Coat Technol* **2005**, *198* (1–3), 247–252. https://doi.org/10.1016/j.surfcoat.2004.10.029.

(15) Jung, H.-Y.; Huang, S.-Y.; Ganesan, P.; Popov, B. N. Performance of Gold-Coated Titanium Bipolar Plates in Unitized Regenerative Fuel Cell Operation. *J Power Sources* **2009**, *194* (2), 972–975. https://doi.org/10.1016/j.jpowsour.2009.06.030.

(16) Wang, S.-H.; Peng, J.; Lui, W.-B. Surface Modification and Development of Titanium Bipolar Plates for PEM Fuel Cells. *J Power Sources* **2006**, *160* (1), 485–489. https://doi.org/10.1016/j.jpowsour.2006.01.020.

(17) Oviroh, P. O.; Akbarzadeh, R.; Pan, D.; Coetzee, R. A. M.; Jen, T.-C. New Development of Atomic Layer Deposition: Processes, Methods and Applications. *Sci Technol Adv Mater* **2019**, *20* (1), 465–496. https://doi.org/10.1080/14686996.2019.1599694.

(18) Zhao, Y.; Zhang, L.; Liu, J.; Adair, K.; Zhao, F.; Sun, Y.; Wu, T.; Bi, X.; Amine, K.; Lu, J.; Sun, X. Atomic/Molecular Layer Deposition for Energy Storage and Conversion. *Chem Soc Rev* **2021**, *50* (6), 3889–3956. https://doi.org/10.1039/D0CS00156B.

(19) Ponraj, J. S.; Attolini, G.; Bosi, M. Review on Atomic Layer Deposition and Applications of Oxide Thin Films. *Critical Reviews in Solid State and Materials Sciences* **2013**, *38* (3), 203–233. https://doi.org/10.1080/10408436.2012.736886.

(20) Abdulagatov, A. I.; Yan, Y.; Cooper, J. R.; Zhang, Y.; Gibbs, Z. M.; Cavanagh, A. S.; Yang, R. G.; Lee, Y. C.; George, S. M. Al $_2$ O $_3$ and TiO $_2$ Atomic Layer Deposition on Copper for Water Corrosion Resistance. *ACS Appl Mater Interfaces* **2011**, *3* (12), 4593–4601. https://doi.org/10.1021/am2009579.

(21) Fusco, M.; Oldham, C.; Parsons, G. Investigation of the Corrosion Behavior of Atomic Layer Deposited Al2O3/TiO2 Nanolaminate Thin Films on Copper in 0.1 M NaCl. *Materials* **2019**, *12* (4), 672. https://doi.org/10.3390/ma12040672.

(22) Dias, V. M.; Chiappim, W.; Fraga, M. A.; Maciel, H. S.; Marciano, F. R.; Pessoa, R. S. Atomic Layer Deposition of TiO $_2$ and Al $_2$ O $_3$ Thin Films for the Electrochemical Study of Corrosion Protection in Aluminum Alloy Cans Used in Beverage. *Mater Res Express* **2020**, *7* (7), 076408. https://doi.org/10.1088/2053-1591/aba557.

(23) Ichou, H.; Arrousse, N.; Berdimurodov, E.; Aliev, N. Exploring the Advancements in Physical Vapor Deposition Coating: A Review. *J Bio Tribocorros* **2024**, *10* (1), 3. https://doi.org/10.1007/s40735-023-00806-0.

(24) Panjan, P.; Drnovšek, A.; Mahne, N.; Čekada, M.; Panjan, M. Surface Topography of PVD Hard Coatings. *Coatings* **2021**, *11* (11), 1387. https://doi.org/10.3390/coatings11111387.

(25) Wu, L.-K.; Wu, J.-J.; Wu, W.-Y.; Cao, F.-H.; Jiang, M.-Y. Sol–Gel-Based Coatings for Oxidation Protection of TiAl Alloys. *J Mater Sci* **2020**, *55* (15), 6330–6351. https://doi.org/10.1007/s10853-020-04466-0.

(26) Figueira, R. B. Hybrid Sol–Gel Coatings for Corrosion Mitigation: A Critical Review. *Polymers (Basel)* **2020**, *12* (3), 689. https://doi.org/10.3390/polym12030689.

(27) Wen, D.; Yuan, R.; Cao, K.; Yang, F.; Chen, R. Advancements in Atomic-Scale Interface Engineering for Flexible Electronics: Enhancing Flexibility and Durability. *Nanotechnology* **2024**, *35* (41), 412501. https://doi.org/10.1088/1361-6528/ad64db.

(28) Kim, T.; Jeon, J.; Ryu, S. H.; Chung, H. K.; Jang, M.; Lee, S.; Chung, Y. J.; Kim, S. K. Atomic Layer Growth of Rutile TiO $_2$ Films with Ultrahigh Dielectric Constants via Crystal Orientation Engineering. *ACS Appl Mater Interfaces* **2024**, *16* (26), 33877–33884. https://doi.org/10.1021/acsami.4c08379.

(29) Jeon, J.; Kim, T.; Jang, M.; Chung, H. K.; Kim, S.-C.; Won, S. O.; Park, Y.; Choi, B. J.; Chung, Y. J.; Kim, S. K. High-Temperature Atomic Layer Deposition of Rutile TiO $_2$ Films on RuO $_2$ Substrates: Interfacial Reactions and Dielectric Performance. *Chemistry of Materials* **2024**, *36* (7), 3326–3333. https://doi.org/10.1021/acs.chemmater.3c03324.

(30) Chung, H. K.; Won, S. O.; Park, Y.; Kim, J.-S.; Park, T. J.; Kim, S. K. Atomic-Layer Deposition of TiO2 Thin Films with a Thermally Stable (CpMe5)Ti(OMe)3 Precursor. *Appl Surf Sci* **2021**, *550*, 149381. https://doi.org/10.1016/j.apsusc.2021.149381.

(31) Nehm, F.; Dollinger, F.; Klumbies, H.; Müller-Meskamp, L.; Leo, K.; Singh, A.; Richter, C.; Schroeder, U.; Mikolajick, T.; Hossbach, C.; Albert, M.; Bartha, J. W. Atomic Layer Deposited TiO /AlO Nanolaminates as Moisture Barriers for Organic Devices. *Org Electron* **2016**, *38*, 84–88. https://doi.org/10.1016/j.orgel.2016.07.037.

(32) Jáquez-Muñoz, J. M.; Gaona-Tiburcio, C.; Mendez-Ramirez, C. T.; Carrera-Ramirez, M. G.; Baltazar-Zamora, M. A.; Santiago-Hurtado, G.; Lara-Banda, M.; Estupiñan-Lopez, F.; Nieves-Mendoza, D.; Almeraya-Calderon, F. Corrosion of Anodized Titanium Alloys. *Coatings* **2024**, *14* (7), 809. https://doi.org/10.3390/coatings14070809.

(33) Butail, G.; Ganesan, P. G.; Raddiar, M.; Teki, R.; Ravishankar, N.; Duquette, D. J.; Ramanath, G. Kinetics of Titania Nanotube Formation by Anodization of Titanium Films. *Thin Solid Films* **2011**, *519* (6), 1821–1824. https://doi.org/10.1016/j.tsf.2010.10.004.

(34) Zhao, Z.; Wang, S.; Zhang, J.; Liu, L.; Jiang, L.; Xu, X.; Song, Y. A Phosphoric Anion Layer Inhibits Electronic Current Generation and Nanotube Growth during Anodization of Titanium. *Nanoscale Adv* **2022**, *4* (21), 4597–4605. https://doi.org/10.1039/D2NA00433J.

(35) V, S. H. S. K.; R, B.; Neelakantan, L.; K, R. Patterned Pt-TiO2 Coated Flow Field Plates in PEM Water Electrolyzers for Hydrogen Production. *Journal of Solid State Electrochemistry* **2024**, *28* (11), 4193–4205. https://doi.org/10.1007/s10008-024-06016-z.

(36) Liu, G.; Peng, S.; Hou, F.; Fang, B.; Wang, X. Au-TiO2/Ti Hybrid Coating as a Liquid and Gas Diffusion Layer with Improved Performance and Stability in Proton Exchange Membrane Water Electrolyzer. *Molecules* **2022**, *27* (19), 6644. https://doi.org/10.3390/molecules27196644.

(37) Paaka Vidyanand Sai; Samatham Madhukar; Malis Krishna Prasad Reddy; N V S Ramachandra Rao. A Review on Machinability Aspects of Titanium Grade-2. *International Journal of Scientific Research in Science, Engineering and Technology* **2017**, *3* (2), 270–275.

(38) Kim, H. S.; Yoo, S. J.; Ahn, J. W.; Kim, D. H.; Kim, W. J. Ultrafine Grained Titanium Sheets with High Strength and High Corrosion Resistance. *Materials Science and Engineering: A* **2011**, *528* (29–30), 8479–8485. https://doi.org/10.1016/j.msea.2011.07.074.

(39) Dubent, S.; Mazard, A. Characterization and Corrosion Behaviour of Grade 2 Titanium Used in Electrolyzers for Hydrogen Production. *Int J Hydrogen Energy* **2019**, *44* (29), 15622–15633. https://doi.org/10.1016/j.ijhydene.2019.04.093.

(40) Toops, T. J.; Brady, M. P.; Zhang, F.-Y.; Meyer, H. M.; Ayers, K.; Roemer, A.; Dalton, L. Evaluation of Nitrided Titanium Separator Plates for Proton Exchange Membrane Electrolyzer Cells. *J Power Sources* **2014**, *272*, 954–960. https://doi.org/10.1016/j.jpowsour.2014.09.016.

(41) Wang, K.; Paxson, A.; Valdez, T. I.; Erlat, A.; Lee, P.-C.; Yun, S.; Khajanji, P.; Zhang, Z.; Kummel, A. C.; Bandaru, P. Enhanced Corrosion Resistance in Aluminum-Based Electrolyzer Components via Stoichiometry Tuned Atomic Layer-Deposited TiO_x Films. *ACS Appl Mater Interfaces* **2024**, *16* (27), 35043–35052. https://doi.org/10.1021/acsami.4c05450.

(42) Daubert, J. S.; Hill, G. T.; Gotsch, H. N.; Gremaud, A. P.; Ovental, J. S.; Williams, P. S.; Oldham, C. J.; Parsons, G. N. Corrosion Protection of Copper Using Al_2O_3, TiO_2, ZnO, HfO_2, and ZrO_2 Atomic Layer Deposition. *ACS Appl Mater Interfaces* **2017**, *9* (4), 4192–4201. https://doi.org/10.1021/acsami.6b13571.

(43) Chiappim, W.; Watanabe, M.; Dias, V.; Testoni, G.; Rangel, R.; Fraga, M.; Maciel, H.; dos Santos Filho, S.; Pessoa, R. MOS Capacitance Measurements for PEALD TiO2 Dielectric Films Grown under Different Conditions and the Impact of Al2O3 Partial-Monolayer Insertion. *Nanomaterials* **2020**, *10* (2), 338. https://doi.org/10.3390/nano10020338.

(44) Vincent, T.; Hsu, J.; Wu, V.; Wills, J. *Routine determination of ultratrace elements in semiconductor grade nitric acid by the Thermo Scientific iCAP RQ ICP-MS*. thermofisher scientific website. https://www.thermofisher.com/order/catalog/product/BRE731416 (accessed 2024-02-23).

(45) Wang, L.; Jin, M.; Zheng, Y.-D.; Guan, Y.-P.; Lu, X.; Luo, J.-L. Nanotubular Surface Modification of Metallic Implants via Electrochemical Anodization Technique. *Int J Nanomedicine* **2014**, 4421. https://doi.org/10.2147/IJN.S65866.

(46) Gerstner, M. E. An Examination of the Corrosion Suppression Mechanism on N-Titanium Dioxide Photoanodes. *J Electrochem Soc* **1979**, *126* (6), 944–949. https://doi.org/10.1149/1.2129199.

(47) Utomo, W. B.; Donne, S. W. Electrochemical Behaviour of Titanium in H2SO4–MnSO4 Electrolytes. *Electrochim Acta* **2006**, *51* (16), 3338–3345. https://doi.org/10.1016/j.electacta.2005.09.031.

(48) de Souza, K. A.; Robin, A. Electrochemical Behavior of Titanium-tantalum Alloys in Sulfuric Acid Solutions. *Materials and Corrosion* **2004**, *55* (11), 853–860. https://doi.org/10.1002/maco.200303792.

(49) Bard, A. J.; Faulkner, L. R.; White, H. S. *Electrochemical Methods: Fundamentals and Applications*, Third.; John Wiley & Sons: Oxford, 2022.

(50) McCafferty, E. Thermodynamics of Corrosion: Pourbaix Diagrams. In *Introduction to Corrosion Science*; Springer New York: New York, NY, 2010; pp 95–117. https://doi.org/10.1007/978-1-4419-0455-3_6.

(51) Yin, Q.; Liu, S.; Fu, X.-Z.; Wang, X.-Z.; Luo, J.-L. Transition of Self-Passivation and Semiconductor Property of Titanium in the Simulated Environments of Proton Exchange Membrane Fuel Cells. *Appl Surf Sci* **2023**, *612*, 155930. https://doi.org/10.1016/j.apsusc.2022.155930.

(52) Kjeang, E. *Microfluidic Fuel Cells and Batteries*; Springer International Publishing: Cham, 2014. https://doi.org/10.1007/978-3-319-06346-1.

(53) Lorenz, W. J.; Mansfeld, F. Determination of Corrosion Rates by Electrochemical DC and AC Methods. *Corros Sci* **1981**, *21* (9–10), 647–672. https://doi.org/10.1016/0010-938X(81)90015-9.

(54) Scully, J. R. Polarization Resistance Method for Determination of Instantaneous Corrosion Rates. *CORROSION* **2000**, *56* (2), 199–218. https://doi.org/10.5006/1.3280536.

(55) Mansfeld, F.; Shih, H.; Greene, H.; Tsai, C. H. Analysis of EIS Data for Common Corrosion Processes. *Electrochemical impedance: analysis and interpretation. ASTM International.* **1993**, No. 1188, 37–53.

(56) Orazem, M. E.; Tribollet, B. *Electrochemical Impedance Spectroscopy*, 1st ed.; Kelly, R., Ed.; The Electrochemical Society (ECS): New Jersey, 2008; Vol. 906.

(57) Brug, G. J.; van den Eeden, A. L. G.; Sluyters-Rehbach, M.; Sluyters, J. H. The Analysis of Electrode Impedances Complicated by the Presence of a Constant Phase Element. *J Electroanal Chem Interfacial Electrochem* **1984**, *176* (1–2), 275–295. https://doi.org/10.1016/S0022-0728(84)80324-1.

(58) Hladky, K.; Callow, L. M.; Dawson, J. L. Corrosion Rates from Impedance Measurements: An Introduction. *British Corrosion Journal* **1980**, *15* (1), 20–25. https://doi.org/10.1179/000705980798318627.